ISSN 1927-0585 (Print)
ISSN 1927-0593 (Online)

JOURNAL OF MATERIALS SCIENCE RESEARCH

Vol. 3, No. 3 July 2014

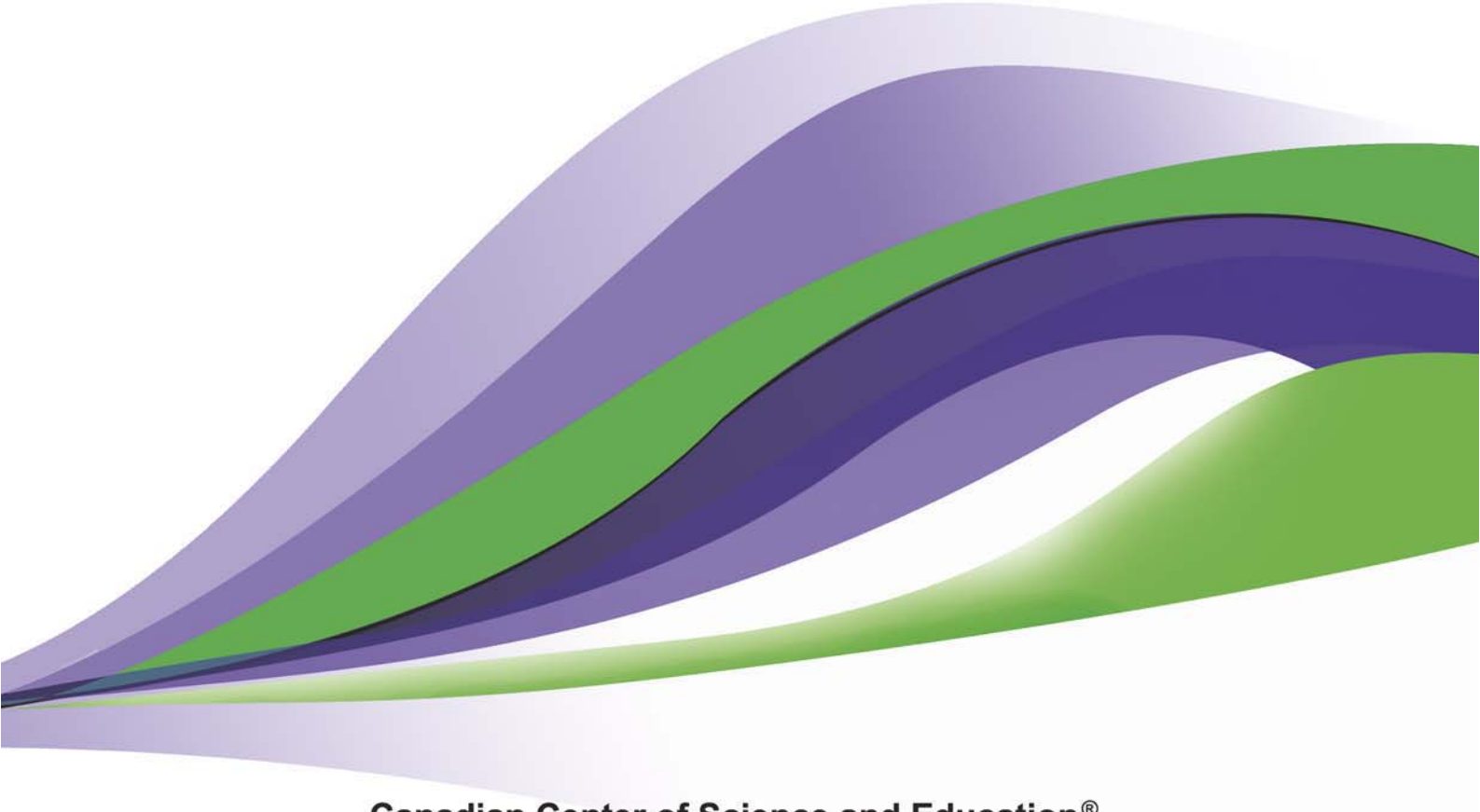

Canadian Center of Science and Education®

Editorial Board

Contents

Journal of Materials Science Research; Vol. 3, No. 3; 2014
ISSN 1927-0585 E-ISSN 1927-0593
Published by Canadian Center of Science and Education

CdO Nanoparticles by Thermal Decomposition of a Cadmium-Hexamethylenetetramine Complex

Divine Mbom Yufanyi[1], Josepha Foba Tendo[1], Agwara Moise Ondoh[2] & Joseph Ketcha Mbadcam[2]

[1] Department of Chemistry, Faculty of Science, University of Buea, Buea, Cameroon

[2] Department of Inorganic Chemistry, Faculty of Science, University of Yaounde I, Yaounde, Cameroon

Correspondence: Josepha Foba Tendo, Department of Chemistry, Faculty of Science, University of Buea, P.O. Box 63, Buea, Cameroon. Tel: 237-7322-7719. E-mail: jnfoba@yahoo.com

Received: March 10, 2014 Accepted: March 24, 2014 Online Published: April 17, 2014

doi:10.5539/jmsr.v3n3p1 URL: http://dx.doi.org/10.5539/jmsr.v3n3p1

Abstract

CdO nanoparticles have been prepared by the thermal decomposition of a precursor complex. A simple and cost effective room temperature synthetic technique allows the preparation of the precursor complex from hexamethylenetetramine and cadmium nitrate in ethanol. The precursor, characterized by elemental analysis, mass spectrometry, Fourier transform infrared spectroscopy (FTIR), and thermal gravimetric analysis, had the composition $[\{Cd(HMTA)(NO_3)_2(H_2O)_2\}n]$. It was calcined at 500 ºC for 2 h, and the cadmium oxide nanoparticles obtained was characterized by X-ray diffraction (XRD), scanning electron microscopy, high resolution transmission electron microscopy (HRTEM), Nitrogen adsorption and physisorption, and Selected Area Electron Diffraction (SAED). XRD shows that the CdO obtained is pure and crystalline. The particles obtained had a cubic morphology and are mesoporous.

Keywords: cadmium oxide, hexamethylenetetramine, nanoparticles, thermal decomposition

1. Introduction

Over the past few decades, nanomaterials, including metal oxide nanoparticles, have received enormous scientific attention because of their interesting novel and improved physico-chemical and biological properties as a result of size reduction to the nano-regime (Devan, Patil, Lin, & Ma, 2012). Their unique physical properties that are size- and shape-dependent, render them applicable in many fields such as optics, magnetism, catalysis, electricity, energy production and storage, environmental remediation, antimicrobial agents and drug delivery (Mao, Park, Zhang, Zhou, & Wong, 2007; S. Wang, Z. Wang, & Zha, 2009; Jolivet et al., 2010). Among the different metal oxide nanoparticles, CdO is an important n-type semiconductor with a cubic structure, which belongs to the II–VI group, with a direct band gap of 2.5 eV and an indirect band gap of 1.98 eV (Tadjarodi & Imani, 2011b). The difference in band gap is attributed to intrinsic cadmium and oxygen vacancies. Due to its ionic nature coupled with its wide band gap, low electrical resistivity and high transmission in the visible region, CdO nanoparticles have been found to be a suitable candidate for application in various fields such as optical, photovoltaic cells, gas sensors, solar cells and front panel displays (Ye, Zhong, Zheng, R. Li, & Y. Li, 2007; Ghoshal et al., 2009; Tadjarodi & Imani, 2011b; Giribabu, Suresh, Manigandan, Stephen, & Narayanan, 2013; Kalpanadevi, Sinduja, & Manimekalai, 2013).

Given that the physico-chemical properties of CdO do not only depend on its chemical composition but also on size, shape and surface structure, the preparation of CdO nanoparticles of well-defined morphology and size is of interest. Synthesis techniques and conditions can considerably affect the properties of CdO nanoparticles. Several synthetic methods (physical, chemical and mechanical), including; hydrothermal method (Ye et al., 2007; Yang et al., 2010; Zhang, Wang, Lin, & Huang, 2010), template assisted method (Prakash, Arunkumar, Sathya Raj, & Jayaprakash, 2013), solvothermal methods (Ghoshal, Biswas, Nambissan, Majumdar, & De, 2009; Saghatforoush, Sanati, Mehdizadeh, & Hasanzadeh, 2012; Kaviyarasu, Manikandan, Paulraj, Mohamed, & Kennedy, 2014), mechano-chemical method (Tadjarodi & Imani, 2011a, 2011b), thermal decomposition (Shi, C. Wang, H. Wang, & Zhang, 2006; Gujar et al., 2008; Askarinejad & Morsali, 2009; Kumar et al., 2012), photosynthetic method (Andeani & Mohsenzadeh, 2013) and sonochemical method (Ramazani & Morsali, 2011; Safarifard & Morsali, 2012) have been employed to prepare CdO nanostructures. These different synthetic procedures have resulted in CdO nanoparticles of varying morphology such as nanowires (Ghoshal et al., 2009;

Yang et al., 2010), nanoplatelets (Giribabu et al., 2013), nanodisks (Shi et al., 2006), nanofibers (Ye et al., 2007), and nanorods (Barakat, Al-Deyab, & Kim, 2012; Kaviyarasu et al., 2014). Most of the synthetic techniques require expensive equipment, extra purification steps and long reaction times. For practical applications, the synthesis should be based on readily available, non-toxic and cheap precursors, as well as simple synthetic procedures without the necessity for additional purification steps.

The synthesis of CdO nanoparticles by thermal decomposition of organo-cadmium compounds or cadmium complexes has also been reported (Ramazani & Morsali, 2011; Ranjbar & Morsali, 2011; Safarifard & Morsali, 2012; Kalpanadevi, Sinduja, & Manimekalai, 2013; Payehghadr & Moasali, 2013). By proper choice of the precursor and the calcination conditions, this could be a simple and cost-effective technique for the preparation of oxide particles with controlled morphologies. However, the robustness and the reproducibility of the method is still a matter of concern.

Hexamethylenetetramine (HMTA) is a cheap and readily available heterocyclic organic compound with a cage-like structure. It is highly soluble in water and polar organic solvents. HMTA is a versatile ligand that can serve as a terminal monodentate or as bi-, tri-, and tetradentate bridging ligand (Kirillov, 2011). Apart from coordinative bonds, HMTA can also (depending on the synthesis conditions and the solvent used) be involved in the formation of hydrogen bonds (Ndifon et al., 2009). The kinetics of the thermal decomposition of some HMTA-transition metal complexes, leading to the formation of metal oxides (Mn, Ni, Zn, Cd) or metal nanoparticles in a carbon matrix (Ni, Co; Ni-Mo and Co-Mo carbides), have already been reported (Chouzier, Afanasiev, Vrinat, Cseri, & Roy-Auberger, 2006; Singh et al., 2007; Afanasiev et al., 2008; Chouzier et al., 2011; Kumar et al., 2012).

In this paper we report the synthesis and characterization (morphology and surface area) of CdO nanoparticles obtained by thermal decomposition of a Cd-HMTA precursor. The precursor was synthesized from simple, cheap, and relatively safer reagents. The synthetic process for both the precursor and the oxide nanoparticles is ecofriendly.

2. Method

2.1 Chemicals

$Cd(NO_3)_2 \cdot 6H_2O$, hexamethylenetetramine and ethanol were obtained from Sigma Aldrich. The chemicals were of analytical grade and were used without further purification.

2.2 Synthesis of the Cd-HMTA Precursor

The precursor was synthesized by modifying a procedure previously reported for a cadmium-HMTA polymeric complex (Kumar et al., 2012).

HMTA (4 mmol, 0.5608 g) was dissolved in 15 mL of ethanol (sonication for 20 min at room temperature). Cadmium nitrate (2 mmol) in 10 mL of ethanol was added drop wise under magnetic stirring. The mixture was stirred for a further 2 h. The white precipitate formed was filtered, washed several times with ethanol and dried in a desiccator over silica gel.

2.3 Synthesis of CdO Nanoparticle

A sample of the dry precursor (0.5 g) was ground, placed in a ceramic crucible and calcined at 500 °C (CdO-500). The crucible was placed in the furnace, heated to the desired calcination temperature, and calcination in air continued for 2 h. The sample was allowed to cool down to room temperature in the furnace. The reddish-brown powder obtained could easily be re-dispersed in water and ethanol.

2.4 Characterization Techniques

Elemental analysis (C, H, N) of the precursor was carried out on a Flash 2000 Thermo Scientific analyzer. Mass spectrometry of the precursor complex was performed on a Micro-Mass LCT Premier mass spectrometer (Waters Corporation, USA). FT-IR spectra were recorded from 4000 to 400 cm^{-1} on a PerkinElmer Spectrum Two universal attenuated total reflectance Fourier transform infrared (UATR-FT-IR) spectrometer. Thermogravimetric analysis (TGA) was obtained using a Pyris 6 PerkinElmer TGA 4000 thermal analyzer. The TGA analysis was conducted between 30 and 900 °C under nitrogen atmosphere at a flow rate of 20 mL/min and a temperature ramp of 10 °C/min. The XRD diffractogram of CdO was recorded on a Bruker D8 Advance X-ray diffractometer using a Cu Kα radiation source (λ = 0.15406 nm, 40 kV and 40 mA). Scans were taken over the 2θ range from 10^o to 100^o in steps of 0.01^o at room temperature in open quartz sample holders. The phase was identified with the help of the BrukerDIFFRACplus evaluation software in combination with the ICDD powder diffraction data base (International Centre for Diffraction Data). SEM images and EDX spectra were obtained on a JEOL

JSM-7600F field-emission scanning electron microscope. Transmission electron microscopy (TEM) was performed on a JEOL JEM-2100F microscope using a maximum acceleration voltage of 200 kV from the field emission gun. The particle size distribution was determined from the TEM image using the ImageJ software. N_2-physisorption experiment for the determination of the total surface area and the average pore diameter was conducted on a Micromeritics ASAP 2020 instrument. Prior to the measurement, the sample was degassed at 200 ˚C for 6 h.

3. Results and Discussion

The white and crystalline Cd-HMTA precursor was obtained from $Cd(NO_3)_2{\cdot}6H_2O$ and HMTA in ethanol at ambient conditions in one step. Light-brown CdO nanoparticles were obtained by calcination of the precursor at 500 ºC.

The elemental composition of the precursor (Table 1) corresponds closely to the empirical formula $CdC_6H_{16}N_6O_8$, which matches the structural formula $Cd(HMTA)(NO_3)_2(H_2O)_2$.

Table 1. Elemental analysis of the Cd-HMTA precursor compared to the values calculated for the empirical formula $CdC_6H_{16}N_6O_8$

Complex	Colour	% Yield	Elemental Analyses: % Found (% Calculated)			
			% Cd	% C	% H	% N
$Cd(HMTA)(NO_3)_2(H_2O)_2$	white	94	(27.24)	18.04 (17.46)	4.07 (3.91)	20.02 (20.37)

The high resolution mass spectrum (MS) of the complex shows a molecular ion (M^+-H) peak at m/z = 411.9 which corresponds to the structural formula derived from elemental analysis. Small peaks above m/z = 411.9 (473, 485, and 489) which correspond to the addition of water or nitrate fragments to the precursor, were also observed on the spectrum.

Table 2. Relevant FTIR bands of HMTA and the Cd-HMTA precursor

HMTA	$[\{Cd(HMTA)(NO_3)_2(H_2O)_2\}_n]$	Band Assignments
-	3480	ν(OH) (coordinated water)
2955	2950	ν(CH_2) stretch
-	1785	Cd-NO_3
1457	1432	ν(CH_2) scissor (HMTA)
1370	1380	ν(CH_2) wag (HMTA)
	1298	ν(CH_2) twist (HMTA)
	1241	ν(CH_2) rock (HMTA)
1235	1228	ν(CH_2) twist (HMTA)
1000	998	ν(CN) stretch (HMTA)
811	819	ν(CN) stretch (HMTA)
670	682	N-C-N bend (HMTA)
-	505	Cd-O stretch

Relevant infrared bands of HMTA and the precursor complex are listed in Table 2. The broad band at 3480 cm^{-1} in the FTIR spectrum of Cd-HMTA (Figure 1) is attributed to ν(OH) of coordinated water (Hee Ng, Guan Teoh, Moris, & Yang Yap, 2004; Ndifon et al., 2009). The band at 1235 cm^{-1}, assigned to the C-N stretching vibration of the free HMTA ligand is split into 1241 and 1228 cm^{-1} in the Cd-HMTA precursor suggesting that HMTA is coordinated to the cadmium ion (Ndifon et al., 2009). Strong prominent peaks at 811 and 1000 cm^{-1} due to the C-N stretching vibration of HMTA (Jensen, 2002) are shifted to 819 and 998 cm^{-1}, respectively in the Cd-HMTA

precursor complex. The weak band observed at 1785 cm^{-1} shows the coordination of a monodentate nitrate ion, Cd-NO_3 (Ndifon et al., 2009). The coordination of water molecules is also indicated by the IR bands in the region 400–600 cm^{-1}, assigned to Cd-H_2O (Ndifon et al., 2009). The elemental, mass spectrum and FTIR analytical results indicate that the complex is probably polymeric with formula $[\{Cd(HMTA)(NO_3)_2(H_2O)_2\}_n]$.

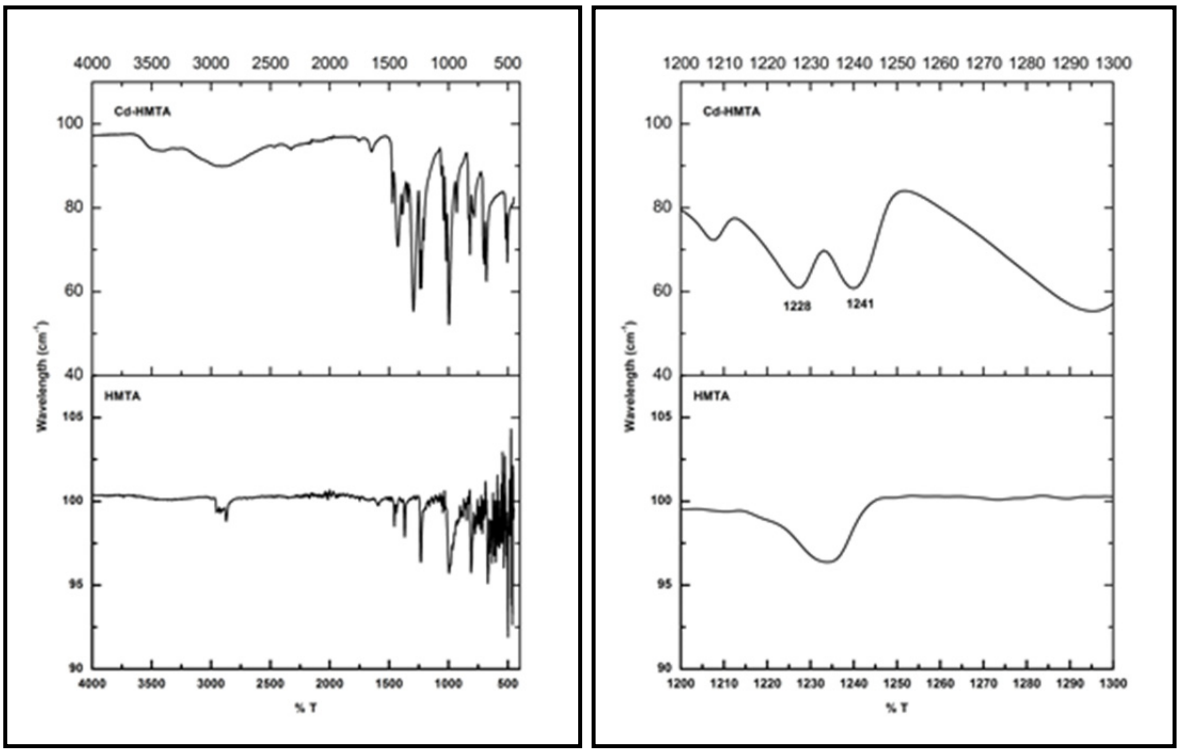

Figure 1. a) FTIR spectra of HMTA and Cd-HMTA precursor complex; b) Expansion of FTIR spectrum in region 1200–1300 cm^{-1} to show split of band

The thermal decomposition curve of the Cd-HMTA precursor is shown in Figure 2 while the relevant decomposition data are summarized in Table 3.

Table 3. Thermal decomposition data for Cd-HMTA precursor

Step	Temperature Range (ºC)	% Mass Loss
1	150–190	6.8
2	200–400	41.4
3	400–630	18.7

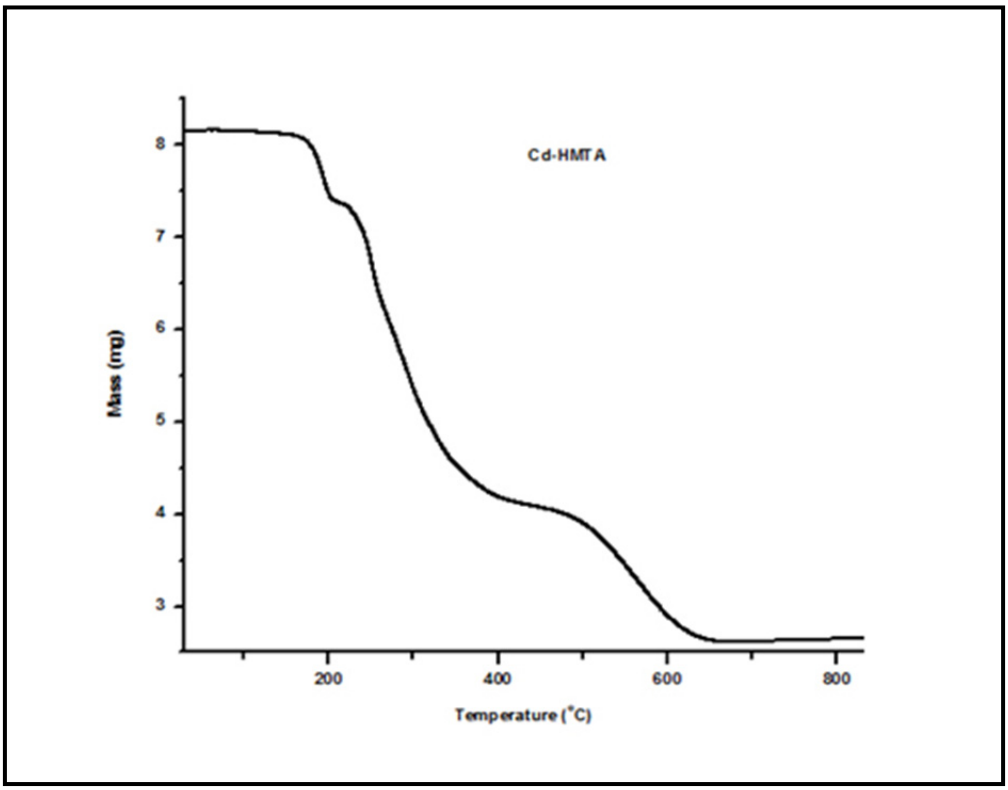

Figure 2. Thermogravimetric analysis of Cd-HMTA precursor complex

The precursor $Cd(HMTA)(NO_3)_2(H_2O)_2$ is composed of 27.25% Cd, 8.72% H_2O, 33.95% HMTA and 30.07% NO_3^-. The TG curve (Figure 2) shows that the precursor decomposes in three major steps within the temperature range 30–830 °C. However, the derivative TG indicates that the pattern is complex; in the range 200–400 °C there are two overlapping decomposition steps and not one (indicated by a strong narrow peak and a weak shallow peak).

The first decomposition step between 150–190 °C which is distinctive (mass loss of 6.8%), can be attributed predominantly to the loss of water (calc. 8.7%). This discrepancy suggests that water may not be lost as molecular water. The major mass loss of 41.4% takes place in the range 200–400 °C. This could be assigned to the decomposition of HMTA and part of the nitrate in the form of various gases (Afanasiev et al., 2008). This assignment is supported by the observation that in this range, the derivative TG indicates that there are two overlapping decomposition steps and not one. The coordination of HMTA to Cd tends to weaken the Cd-NO_3^- bond, suggesting that the bonding environment of the nitrates is not identical and thus will decompose at different temperatures. We propose that the extensively H-bonded nitrates decompose at slightly lower temperatures than the covalently bonded ones. Over the range 400–630 ºC we have another distinctive decomposition step with a mass loss of 18.7% which can be assigned to the decomposition of the remaining nitrate. A stable mass is obtained at 630 °C with 32.1% residue (calc. 31.3%), which is predominantly CdO due to the oxidative nature of the environment (presence of water vapour).

The calcination temperature was chosen as 500 °C from the derivative TG plot which indicates that 550 °C is the optimum temperature. This temperature is lower than that indicated by the TG (630 °C). This is probably due to the use of a fast heating rate (10 °C per minute) which permits a base-line drift further away from equilibrium conditions because a short time is required for each determination.

The XRD pattern of CdO obtained is shown in Figure 3. The sharp and well defined peaks indicate the crystalline nature of CdO. The strong diffraction peaks in the XRD spectrum of CdO occurring at 2θ values of 33.00, 38.29, 55.27, 65.87, 69.24, and 81.95 are indexed as the (111), (200), (220), (311), (222), and (400) crystal planes and correspond to the cubic structure of CdO (JCPDS card No. 65-2908). No other impurity peaks were detected indicating that the obtained CdO was phase pure. The average particle size of CdO was calculated using Debye-Scherrer equation (Equation 1) (Klug & Alexander, 1974):

$$D = k\lambda/\beta \mathrm{Sin}\theta \quad (1)$$

Where D is the average particle size, λ is the X-ray wavelength, β is the corrected width of the XRD peak at half height, k is the shape factor which is approximated as 0.89, and θ is the Bragg diffraction angle. The calculated average particle size of cadmium oxide nanoparticles was found to be 30.9 nm.

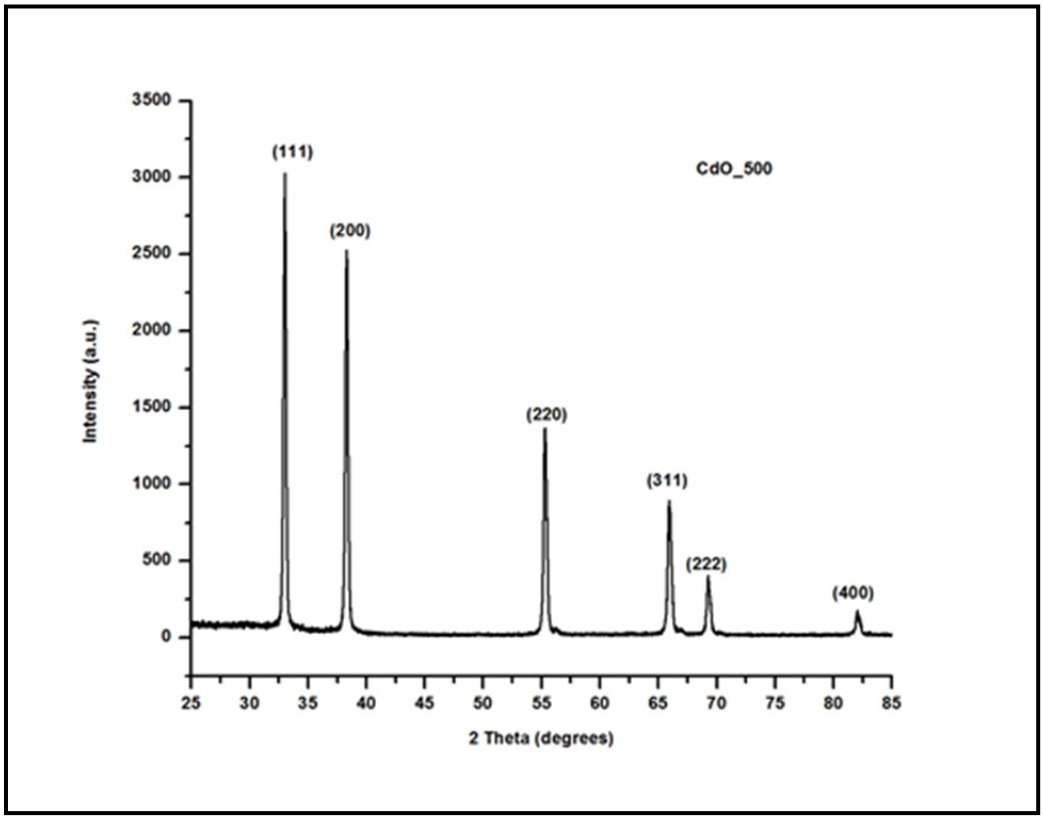

Figure 3. XRD pattern of CdO nanoparticles

The morphology and structural features of CdO nanoparticles were determined by SEM, TEM and SAED. The SEM image (Figure 4a) indicates that the Cd-HMTA precursor has a spike-shaped morphology, while the CdO nanoparticles have rod-like morphology. The EDX spectrum of the precursor (Figure 4c) indicates that it contains only Cd, C, H, N, and O, while that of CdO (Figure 4d) indicates pure CdO is obtained. The Cu impurity found in the EDX of CdO is due to the sample holder.

The HRTEM image (Figure 5a) of CdO shows particles with a cubic shape. The larger particles present are due to aggregation or the overlapping of small particles. The average particle diameter of 22.7 nm for CdO was determined after a log normal fitting of the data obtained from the TEM image. The resulting histogram and average particle size are shown in Figure 6a. The average particle size from HRTEM is consistent with values obtained by XRD. The SAED image of CdO (Figure 5b) shows bright spots which indicate that the CdO nanoparticles are polycrystalline in nature.

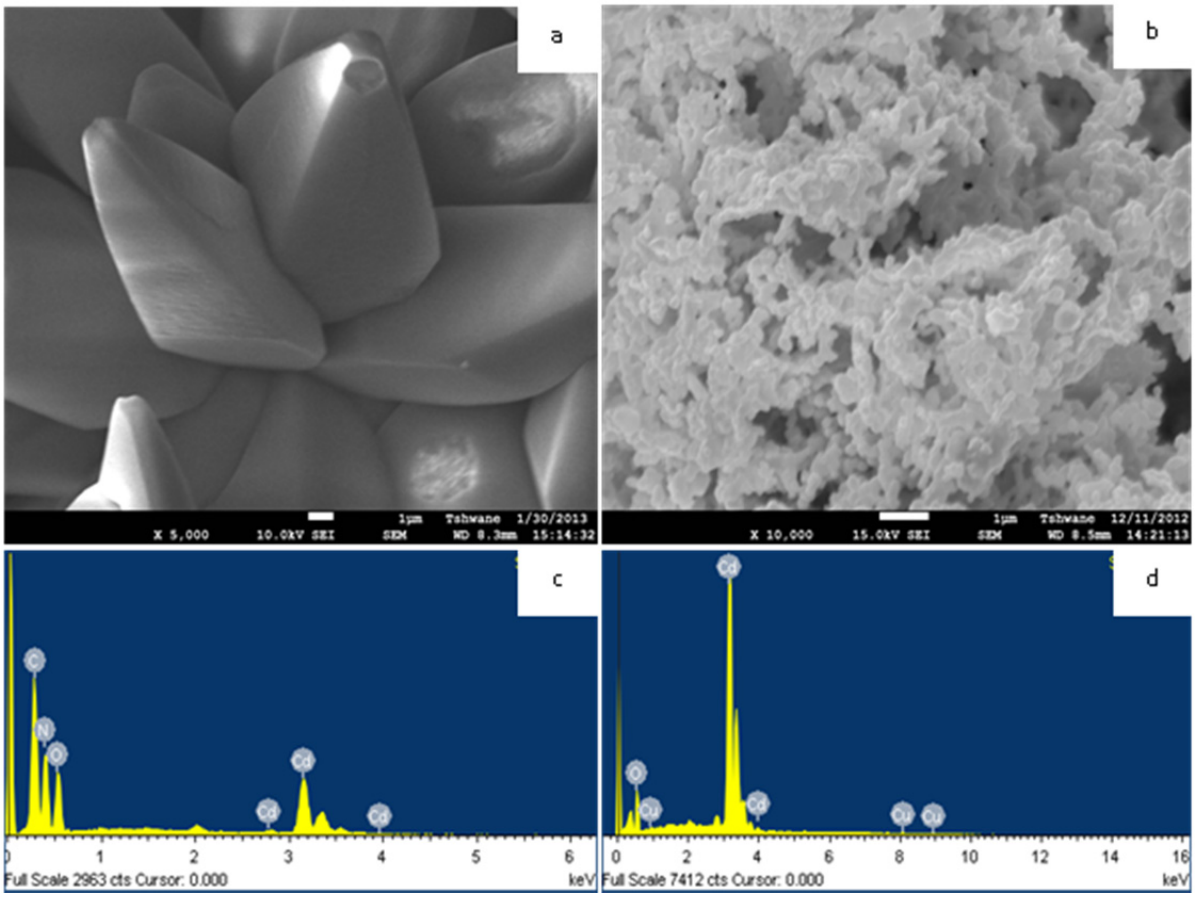

Figure 4. SEM images of (a) Cd-HMTA precursor and (b) CdO; EDX images of (c) Cd-HMTA precursor and (d) CdO

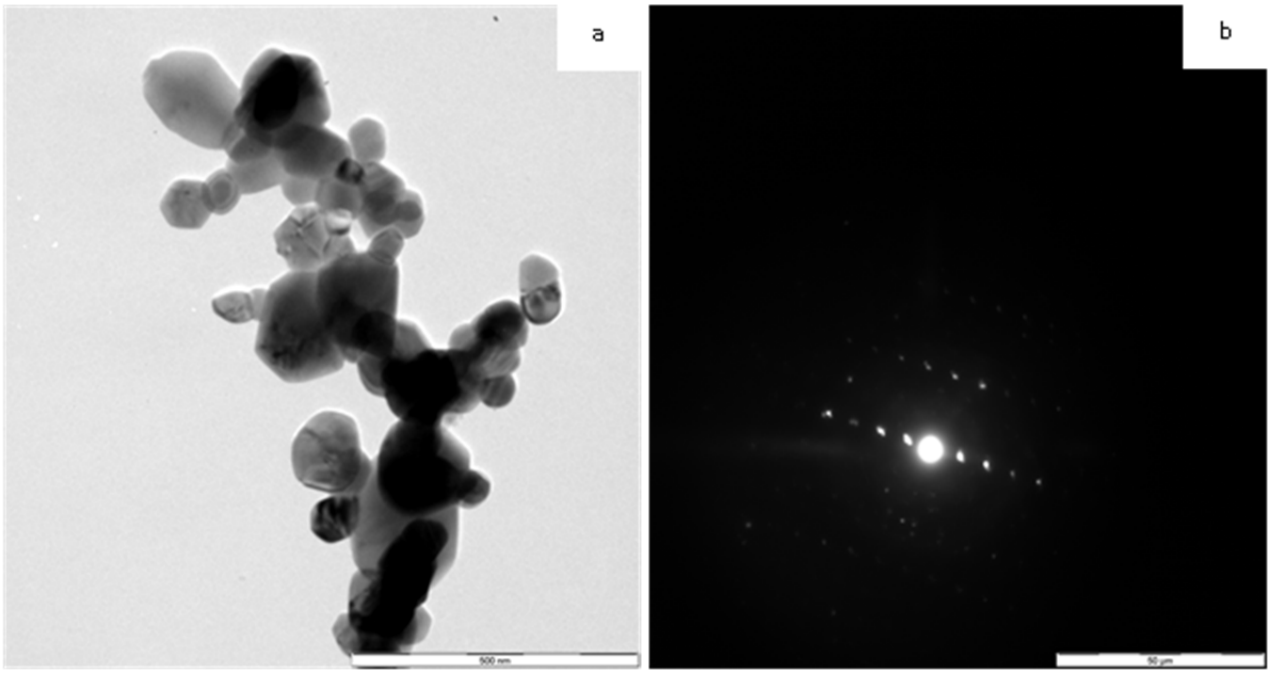

Figure 5. (a) TEM image and (b) SAED image of CdO nanoparticle

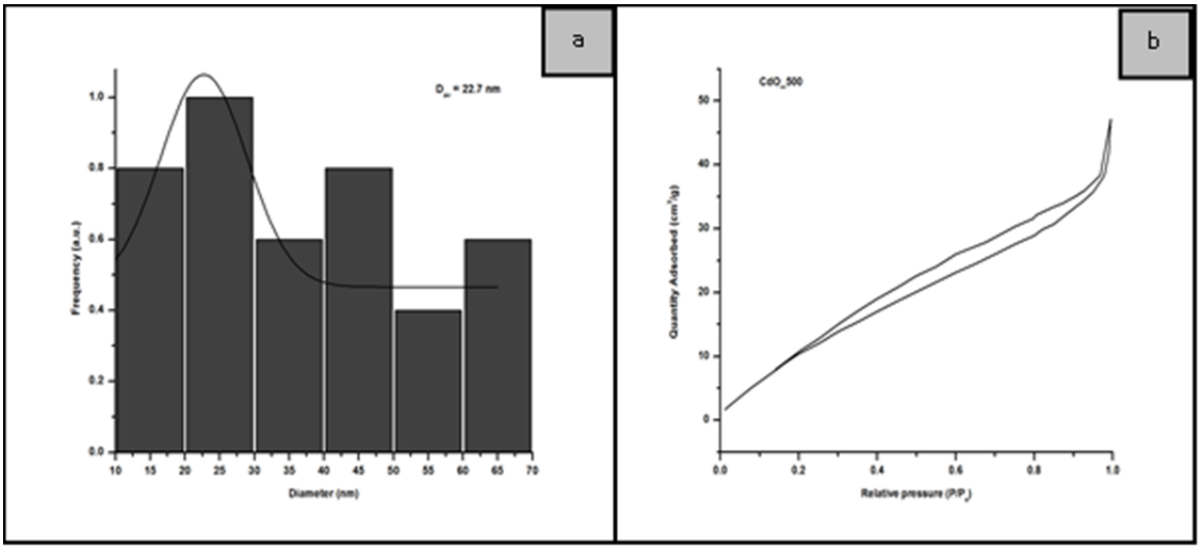

Figure 6. (a) Particle size distribution and (b) N_2 adsorption/desorption isotherm for CdO nanoparticles

For comparison, some CdO particle morphologies and sizes found in the literature that are obtained by the thermal decomposition of different precursors are listed in Table 4. The results indicate that cubic nanoparticles with sizes in the range 10–70 nm obtained from the Cd-HMTA precursor of this study compares favorably with those obtained from other starting materials. It can also be observed from Table 4 that our starting materials are the simplest, most readily available, and very cost-effective.

Table 4. Particle sizes (HRTEM) of CdO prepared by the thermal decomposition of various precursors at different calcination temperatures

Precursor	Calcination		Particle Size (HRTEM) (nm)	Morphology	Ref.
	Time (h)	Temperature (ºC)			
$Cd(CH_3COO)_2{\cdot}2H_2O$ + $CO(NH_2)_2$	2	500	46	Spherical	(Tadjarodi et al., 2013)
$Cd(Cin)_2{\cdot}(N_2H_4)_2$	0.45	500	31	Cubic	(Kalpanadevi et al., 2013)
$Cd(CH_3COO)_2{\cdot}2H_2O$ + PEG-400 + NaOH	1	400	15–36	/	(Liu et al., 2011)
$[Cd(L)_2(H_2O)_2]$	4	650	/	Agglomerated particles	(Safarifard & Morsali, 2012)
Cis-[dmphen-CdI_2]	2	400	50	Spherical	(Aldwayyan et al., 2013)
$[\{Cd(HMTA)(NO_3)_2(H_2O)_2\}_n]$	2	500	10–70	Cubic	This work

Cin = Cinnamic acid; PEG = polyethylene glycol; L = 1H-1,2,4-triazole-3-carboxylate; dmphen = 2,9-dimethyl-1,10-phenanthroline

The surface area and average pore size distribution (PSD) of CdO nanoparticles were determined by N_2 physisorption. The nitrogen adsorption–desorption isotherms (Figure 6b) of CdO can be classified as type IV with H3 hysteresis loop (according to the IUPAC classification) (Greg & Sing, 1982). The isotherm type and hysteresis loop observed here indicates that CdO nanoparticles possess slit mesoporous structure (Greg & Sing, 1982). The BET surface area (according to Brunauer, Emmett and Teller) of CdO was found to be 58.4 m^2/g and the pore volume 0.059 cm^3/g. The Barrett-Joyner-Halenda (BJH) desorption pore size distribution of 4.7 nm indicates a mesoporous structure for the CdO nanoparticles with high surface contact sites.

4. Conclusion

Pure, crystalline and cubic CdO nanoparticles have been synthesized by the thermal decomposition of a Cd-HTMA precursor. The TG curve indicates the precursor decomposes in three steps but the derivative TG suggests the second decomposition step is composed of two overlapping steps instead of one. This renders the decomposition pattern more complex. The metal oxide nanoparticles were confirmed by XRD and calculated to have average size 30.9 nm. The morphology of the oxide nanoparticles (cubic) is different from that of the precursor (spikelike) and they have sizes in the range 10–70 nm. The average size of 22.7 nm for the nanoparticles is lower or compares favorably with those obtained by the decomposition of more expensive or less readily available starting materials. The CdO nanoparticles obtained is mesoporous, has a surface area of 58.4 m^2/g and an average pore diameter of 4.7 nm. The low-temperature synthetic technique is simple and cost effective and it can be extended to the synthesis of other metal oxide nanoparticles.

Acknowledgments

The authors thank Dr. Khamlich Saleh (University of Pretoria) for assistance with the SEM and TEM images.

References

Afanasiev, P., Chouzier, S., Czeri, T., Pilet, G., Pichon, C., Roy, M., & Vrinat, M. (2008). Nickel and Cobalt Hexamethylentetramine Complexes $(NO_3)_2Me(H_2O)_6(HMTA)_2{\cdot}4H_2O$ (Me = Co^{2+}, Ni^{2+}): New Molecular Precursors for the Preparation of Metal Dispersions. *Inorganic Chemistry, 47*(7), 2303-2311. http://dx.doi.org/10.1021/ic7013013

Aldwayyan, A. S., Al-Jekhedab, F. M., Al-Noaimi, M., Hammouti, B., Hadda, T. B., Suleiman, M., & Warad, I. (2013). Synthesis and Characterization of CdO Nanoparticles Starting from Organometalic Dmphen-CdI_2 complex. *International Journal of Electrochemical Science, 8*, 10506-10514. Retrieved from http://www.electrochemsci.org/papers/vol8/80810506.pdf

Andeani, J. K., & Mohsenzadeh, S. (2013). Phytosynthesis of Cadmium Oxide Nanoparticles from Achillea wilhelmsii Flowers. *Journal of Chemistry, 2013*, 1-4. http://dx.doi.org/10.1155/2013/147613

Askarinejad, A., & Morsali, A. (2009). Synthesis of cadmium(II) hydroxide, cadmium(II) carbonate and cadmium(II) oxide nanoparticles; investigation of intermediate products. *Chemical Engineering Journal, 150*(2), 569-571. http://dx.doi.org/10.1016/j.cej.2009.03.005

Barakat, N. A. M., Al-Deyab, S., & Kim, H. Y. (2012). Synthesis and study of the photoluminescence and optical characteristics of Cd/CdO nanorods prepared by the electrospinning process. *Materials Letters, 66*(1), 225-228. http://dx.doi.org/10.1016/j.matlet.2011.08.074

Chouzier, S., Afanasiev, P., Vrinat, M., Cseri, T., & Roy-Auberger, M. (2006). One-step synthesis of dispersed bimetallic carbides and nitrides from transition metals hexamethylenetetramine complexes. *Journal of Solid State Chemistry, 179*(11), 3314-3323. http://dx.doi.org/10.1016/j.jssc.2006.06.026

Chouzier, S., Czeri, T., Roy-Auberger, M., Pichon, C., Geantet, C., Vrinat, M., & Afanasiev, P. (2011). Decomposition of molybdate–hexamethylenetetramine complex: One single source route for different catalytic materials. *Journal of Solid State Chemistry, 184*(10), 2668-2677. http://dx.doi.org/10.1016/j.jssc.2011.08.005

Devan, R. S., Patil, R. A., Lin, J. -H., & Ma, Y. -R. (2012). One-Dimensional Metal-Oxide Nanostructures: Recent Developments in Synthesis, Characterization, and Applications. *Advanced Functional Materials, 22*(16), 3326-3370. http://dx.doi.org/10.1002/adfm.201201008

Ghoshal, T., Biswas, S., Nambissan, P. M. G., Majumdar, G., & De, S. K. (2009). Cadmium Oxide Octahedrons and Nanowires on the Micro-Octahedrons: A Simple Solvothermal Synthesis. *Crystal Growth & Design, 9*(3), 1287-1292. http://dx.doi.org/10.1021/cg800203y

Giribabu, K., Suresh, R., Manigandan, R., Stephen, A., & Narayanan, V. (2013). Cadmium oxide nanoplatelets: synthesis, characterization and their electrochemical sensing property of catechol. *Journal of Iranian Chemical Society, 10*, 771-776. http://dx.doi.org/10.1007/s13738-012-0211-3

Greg, S. J., & Sing, K. S. W. (1982). *Adsorption, Surface Area and Porosity* (2nd ed.). Academic Press.

Gujar, T. P., Shinde, V. R., Kim, W. -Y., Jung, K. -D., Lokhande, C. D., & Joo, O. -S. (2008). Formation of CdO films from chemically deposited $Cd(OH)_2$ films as a precursor. *Applied Surface Science, 254*(13), 3813-3818. http://dx.doi.org/10.1016/j.apsusc.2007.12.015

Hee Ng, C., Guan Teoh, S., Moris, N., & Yang Yap, S. (2004). Structural, infrared spectral and

thermogravimetric analysis of a hydrogen-bonded assembly of cobalt(II) and nickel(II) mixed complex cations with hexamethylenetetraamine and aqua ligands: $\{[M(hmt)_2(H_2O)_4][M(H_2O)_6]\}(SO_4)_2 \cdot 6H_2O$. *Journal of Coordination Chemistry, 57*(12), 1037-1046. http://dx.doi.org/10.1080/00958970412331281791

Jensen, J. O. (2002). Vibrational frequencies and structural determinations of hexamethylenetetraamine. *Spectrochimica Acta Part A: Molecular and Biomolecular Spectroscopy, 58*(7), 1347-1364. http://dx.doi.org/10.1016/S1386-1425(01)00585-6

Jolivet, J. -P., Cassaignon, S., Chaneac, C., Chiche, D., Durupthy, O., & Portehault, D. (2010). Design of metal oxide nanoparticles: Control of size, shape, crystalline structure and functionalisation by aqueous chemistry. *C.R. Chimie, 13*, 40-51. http://dx.doi.org/10.1016/j.crci.2009.09.012

Kalpanadevi, K., Sinduja, C. R., & Manimekalai, R. (2013). Characterisation of Zinc Oxide and Cadmium Oxide Nanostructures Obtained from the Low Temperature Thermal Decomposition of Inorganic Precursors. *ISRN Inorganic Chemistry, 2013*, 1-5. http://dx.doi.org/10.1155/2013/823040

Kaviyarasu, K., Manikandan, E., Paulraj, P., Mohamed, S. B., & Kennedy, J. (2014). One dimensional well-aligned CdO nanocrystal by solvothermal method. *Journal of Alloys and Compounds, 593*, 67-70. http://dx.doi.org/10.1016/j.jallcom.2014.01.071

Kirillov, A. M. (2011). Hexamethylenetetramine: An old new building block for design of coordination polymers. *Coordination Chemistry Reviews, 255*(15–16), 1603-1622. http://dx.doi.org/10.1016/j.ccr.2011.01.023

Klug, H. P., & Alexander, L. E. (1974). *X-ray Diffraction Procedures for Polycrystalline and Amorphous Materials*. New York: Wiley.

Kumar, D., Kapoor, I. P. S., Singh, G., Goel, N., & Singh, U. P. (2012). Preparation, characterization and thermal behaviour of polymeric complex of cadmium hexamethylenetetramine nitrate. *Solid State Sciences, 14*, 495-500. http://dx.doi.org/10.1016/j.solidstatesciences.2012.01.021

Liu, J., Zhao, C., Li, Z., Yu, L., Li, Y., Gu, S., … Yang, C. (2011). Solid State Synthesis and Optical properties-Controlling Studies of CdO Nanoparticles. *Advanced Materials Research, 228-229*, 580-585. http://dx.doi.org/10.4028/www.scientific.net/AMR.228-229.580

Mao, Y., Park, T. -J., Zhang, F., Zhou, H., & Wong, S. S. (2007). Environmentally Friendly Methodologies of Nanostructure Synthesis. *Small, 3*(7), 1122-1139. http://dx.doi.org/10.1002/smll.200700048

Ndifon, P. T., Agwara, M. O., Paboudam, A. G., Yufanyi, D. M., Ngoune, J., Galindo, A., … Mohamadou, A. (2009). Synthesis, characterisation and crystal structure of a cobalt(II)-hexamethylenetetramine coordination polymer. *Transition Metal Chemistry, 34*(7), 745-750. http://dx.doi.org/10.1007/s11243-009-9257-1

Payehghadr, M., & Moasali, A. (2013). Thermolysis preparation of cadmium(II) oxide nanoparticles from a new three-dimensional cadmium(II) supramolecular compound. *Journal of Structural Chemistry, 54*(4), 787-791. http://dx.doi.org/10.1134/s0022476613040197

Prakash, T., Arunkumar, T., Sathya Raj, D., & Jayaprakash, R. (2013). Surfactant-liaised Variation in CdO Nanocomposites Morphology. *Physics Procedia, 49*, 36-43. http://dx.doi.org/10.1016/j.phpro.2013.10.008

Ramazani, M., & Morsali, A. (2011). Sonochemical syntheses of a new nano-plate cadmium(II) coordination polymer as a precursor for the synthesis of cadmium(II) oxide nanoparticles. *Ultrasonics Sonochemistry, 18*(5), 1160-1164. http://dx.doi.org/10.1016/j.ultsonch.2010.12.011

Ranjbar, Z. R., & Morsali, A. (2011). Ultrasound assisted syntheses of a nano-structured two-dimensional mixed-ligand cadmium(II) coordination polymer and direct thermolyses for the preparation of cadmium(II) oxide nanoparticles. *Polyhedron, 30*(6), 929-934. http://dx.doi.org/10.1016/j.poly.2010.12.033

Safarifard, V., & Morsali, A. (2012). Sonochemical syntheses of a nanoparticles cadmium(II) supramolecule as a precursor for the synthesis of cadmium(II) oxide nanoparticles. *Ultrasonics Sonochemistry, 19*(6), 1227-1233. http://dx.doi.org/10.1016/j.ultsonch.2012.02.013

Saghatforoush, L. A., Sanati, S., Mehdizadeh, R., & Hasanzadeh, M. (2012). Solvothermal synthesis of $Cd(OH)_2$ and CdO nanocrystals and application as a new electrochemical sensor for simultaneous determination of norfloxacin and lomefloxacin. *Superlattices and Microstructures, 52*(4), 885-893. http://dx.doi.org/10.1016/j.spmi.2012.07.019

Shi, W., Wang, C., Wang, H., & Zhang, H. (2006). Hexagonal Nanodisks of Cadmium Hydroxide and Oxide

with Nanoporous Structure. *Crystal Growth & Design, 6*(4), 915-918. http://dx.doi.org/10.1021/cg050431z

Singh, G., Baranwal, B. P., Kapoor, I. P. S., Kumar, D., & Fröhlich, R. (2007). Preparation, X-ray Crystallography, and Thermal Decomposition of Some Transition Metal Perchlorate Complexes of Hexamethylenetetramine. *The Journal of Physical Chemistry A, 111*(50), 12972-12976. http://dx.doi.org/10.1021/jp077278z

Tadjarodi, A., & Imani, M. (2011a). A novel nanostructure of cadmium oxide synthesized by mechanochemical method. *Materials Research Bulletin, 46*(11), 1949-1954. http://dx.doi.org/10.1016/j.materresbull.2011.07.016

Tadjarodi, A., & Imani, M. (2011b). Synthesis and characterization of CdO nanocrystalline structure by mechanochemical method. *Materials Letters, 65*(6), 1025-1027. http://dx.doi.org/10.1016/j.matlet.2010.12.054

Tadjarodi, A., Imani, M., & Kerdari, H. (2013). Application of a facile solid-state process to synthesize the CdO spherical nanoparticles. *International Nano Letters, 3*(43), 1-6. http://dx.doi.org/10.1186/2228-5326-3-43

Wang, S., Wang, Z., & Zha, Z. (2009). Metal nanoparticles or metal oxide nanoparticles, an efficient and promising family of novel hetrogeneous catalysts in organic synthesis. *Dalton Transactions*, 9363-9373. http://dx.doi.org/10.1039/b913539a

Yang, Z. -X., Zhong, W., Yin, Y. -X., Du, X., Deng, Y., Au, C., & Du, Y. -W. (2010). Controllable Synthesis of Single-Crystalline CdO and $Cd(OH)_2$ Nanowires by a Simple Hydrothermal Approach. *Nanoscale Research Letters, 5*, 961-965. http://dx.doi.org/10.1007/s11671-010-9589-y

Ye, M., Zhong, H., Zheng, W., Li, R., & Li, Y. (2007). Ultralong Cadmium Hydroxide Nanowires: Synthesis, Characterization, and Transformation into CdO Nanostrands. *Langmuir, 23*(17), 9064-9068. http://dx.doi.org/10.1021/la070111c

Zhang, J., Wang, Y., Lin, Z., & Huang, F. (2010). Formation and Self-Assembly of Cadmium Hydroxide Nanoplates in Molten Composite-Hydroxide Solution. *Crystal Growth & Design, 10*(10), 4285-4291. http://dx.doi.org/10.1021/cg901559y

Journal of Materials Science Research; Vol. 3, No. 3; 2014
ISSN 1927-0585 E-ISSN 1927-0593
Published by Canadian Center of Science and Education

Effect of Hemp'S Soluble Components on the Physical Properties of Hemp Concrete

Rosanne Walker[1] & Sara Pavía[1]

[1] Dept of Civil Engineering, Trinity College, Dublin 2, Ireland

Correspondence: Sara Pavía, Dept of Civil Engineering, Trinity College, Dublin 2, Ireland. Tel: 353-1896-2516. E-mail: pavias@tcd.ie

Received: November 21, 2013 Accepted: February 28, 2014 Online Published: June 13, 2014

doi:10.5539/jmsr.v3n3p12 URL: http://dx.doi.org/10.5539/jmsr.v3n3p12

Abstract

Lime hemp concrete is a sustainable building material made with hemp shiv and lime. In this research, pozzolans are added to the lime binder. Hemp shiv contains water soluble constituents including pectic polysaccharides which can dissolve in the mixing water. Sugars and pectins are known to retard clinker hydration in portland cement. This research studies whether the hemp soluble components impact lime-pozzolan paste reactions thus affecting the properties of hemp concrete with lime-pozzolan binder. Physical tests and microstructural analyses were undertaken to determine how the water soluble hemp constituents influence the hydration reactions responsible for setting and hardening of lime-pozzolan pastes. The effect of hemp particles on a lime-pozzolan binder was also investigated using microstructural analysis.

Physical testing evidenced that the hemp's soluble constituents do not alter ultimate strength however, they delay pozzolanic reaction retarding setting and early strength development. The microstructural analysis of lime-pozzolan pastes agreed with the above, evidencing that the hemp delays the formation of hydrates, in particular calcium silica hydrates. The halt of the pozzolanic reaction by the hemp particles was clear at the hemp interface, where few hydrates were evident. This suggests that the properties of the hemp particles including their high suction (which removes water at the interface) and their high porosity (which assists CO_2 diffusion) contribute to the halt of the pozzolanic reaction.

Keywords: lime-hemp concrete, pectin, pozzolanic reaction, hydration, setting, strength

1. Introduction

Lime hemp concrete is a sustainable, carbon negative building material that can replace high embodied energy materials in certain applications thus making construction more sustainable. Lime hemp composites have been used in France since the 1990s and are gaining popularity in Europe. They are made with hemp shiv, which is the woody interior of the hemp stalk, and a lime-based binder. Commercial binders currently available and binders designed on site by building practitioners typically include hydraulic lime, portland cement (PC) and additions. The purpose of the hydraulic lime and PC is to improve early age properties such as setting and strength development. This paper is part of a research programme which aims at formulating a binder using calcium lime and pozzolans. It is intended that the pozzolans will eliminate the need for hydraulic lime and PC so that the material can have a lower environmental impact.

Pozzolans are materials with an amorphous siliceous or siliceous and aluminous content that react with portlandite ($CH=Ca(OH)_2$) in the presence of water to form hydrates (similar to cement hydration) thereby accelerating the slow hardening (carbonation) of calcium limes by imparting a hydraulic set. They have been used to enhance the properties of composites since antiquity. Previous research by the authors indicated two suitable pozzolans for use in lime hemp composites: Ground Granulated Blastfurnace Slag (GGBS) and metakaolin; on account of their fast setting and high reactivity (Walker & Pavía, 2010; Walker & Pavía, 2011). In this paper, Rice Husk Ash (RHA) was also included in several tests to study the effect of the pectins on a fully siliceous pozzolan.

1.1 Effect of Organic Compounds on Material Properties

The amount and type of hydrates produced upon binder hydration, and the time at which they appear, impact the physical properties of cement and lime composites, including setting and early strength development. Sugars and

pectins are known to retard hydration in cement (Young, 1972; Ramachandran, Feldman, & Beaudoin, 1981). Hemp comprises of cellulose, hemicelluloses, lignin and pectin, and the percentage of each component is dependent on a number of variables such as growing conditions, maturity and decortification. Some of these are water soluble (including pectin). They can dissolve in the mixing water and have been reported to delay the set of gypsum binders by trapping calcium ions, thus resulting in a lack of calcium available to form calcium silicate hydrates (Dalmay et al., 2010). The hemp pectins are partly present as methyl esters (Figure 1). In an alkaline environment, their ester groups saponify and react with the calcium ions of lime (CH-portlandite) (Zsivanovits, MacDougall, Smith, & Ring, 2004; Renard & Thibault, 1996; Fang et al., 2008; Sedan et al., 2007; Kavasa, Olgunb, Erdoganb, & Oncec, 2007).

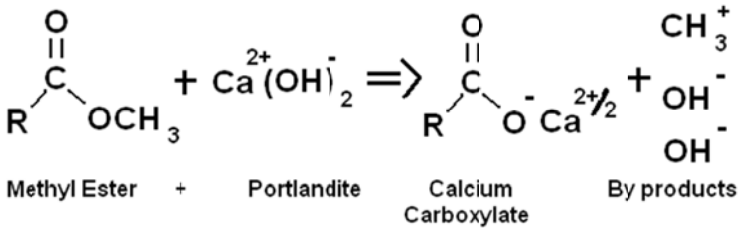

Figure 1. Summary of behaviour of water soluble pectin present as a methyl ester in a lime-rich media

Research to date has focused on the influence of hemp fibre in PC and gypsum binders, however, this paper investigates the influence of hemp shiv on the lime and lime- pozzolan reactions that govern the early properties of lime hemp concrete.

1.2 Relationships Between Hydration, Setting and Hardening

As aforementioned, the amount and type of hydrates formed in binder reactions and the time at which they appear impact the physical properties of cement and lime composites, including setting and strength development. For example in PC, silicate hydrates are stronger than aluminates (Bogue & Lerch, 1934; Beaudoin & Ramachandran, 1992) thus they are the main contributors to strength since early age (1 -10 days). At 28 days, C_2S has a compressive strength of c.5MPa while C_3A strength is close to zero (Beaudoin & Ramachandran 1992). Aluminates, despite contributing little to strength, are responsible for the early set of the paste.

The hydration of the lime- pozzolan mixes in this research differs from PC hydration but produces similar compounds since the overall chemical composition of the two systems is similar. Differences are minor and generally affect the amount rather than the nature of the hydrate phases formed (Massazza, 2007) which include calcium silicate hydrates (CSH) and calcium silica aluminate hydrates (CSAH).

In general, the acceleration of hydration contributes to strength development. The acceleration of the pozzolanic reaction positively affects strength development, and the rate of strength increase depends on the type of pozzolan (amount of lime that it combines) and the type and microstructure of the hydration products formed (Massazza, 2007). Due to the slightly different chemical composition of the pozzolans investigated (clinker-bearing GGBS; alumina-rich metakaolin and silica-rich RHA), hydration will generate similar hydrates, however in different quantities and at different times, during setting and early strength development.

In the GGBS paste, clinker hydration occurs first, and this is followed by pozzolanic reaction between the pozzolan's active silica/alumina and lime (CH). Therefore, setting is mainly attributed to the formation of CSH upon clinker hydration. The GGBS investigated contains no C_3A clinkers however, its alumina content is 13.85% therefore, aluminates formed in pozzolanic reactions might contribute to setting.

In the RHA paste, a pozzolanic reaction occurs between the RHA's amorphous silica and lime to form CSH. RHA contains very little alumina (1.93 % vs 45.26 in metakaolin) therefore, no significant aluminates will be found upon hydration and setting and strength development will be due to the formation of CSH.

At ambient temperature, the products of hydration of lime- metakaolin pastes are mainly CSH and CSAH (gehlenite -C_2ASH_8- and C_4AH_{13}) (Murat, 1983; de Silva & Glasser, 1993; He, Makovicky, & Osbæck, 1994; Donchev, Nivov, Doykov, Petrova, & Dimova, 2010). There is no definite sequence of formation of pozzolanic hydration products due to numerous variables. However, Rojas and Cabrera (2002) report that CSH forms first followed by C_2ASH_8 and later C_4AH_{13} which progressively increases over time. According to this, the initial set

of the paste should be due to the formation of CSH. A previous study which compared reactivity of a number of pozzolans found that pozzolans with the highest Al_2O_3 content set the fastest (Walker & Pavía, 2010; Walker & Pavía, 2011), therefore, it is likely that aluminates also contribute to setting.

2. Materials and Methods

2.1 Materials

A hydrated commercial lime (CL90s) complying with EN 459-1 was used. As aforementioned, two pozzolans, metakaolin and GGBS, were identified as having potential for use in the lime hemp composite on account of their fast setting times and high reactivity (Walker & Pavía, 2010; Walker & Pavía, 2011). The programme of research concentrates on these two pozzolans however RHA was included in several tests to study the effect of the pectins on a fully siliceous pozzolan. The pozzolan composition, rate of amorphousness and surface area are included in Table 1.

The chemical composition was determined by XRF using a Quant'X EDX Spectrometer and UniQuant analysis package. The mineralogy and rate of amorphousness were analysed by X-Ray diffraction (XRD), using a Phillips PW1720 XRD with a PW1050/80 goniometer and a PW3313/20 Cu k-alpha anode tube at 40 kV and 20 mA. The specific surface area was measured using a Quantachrome Nova 4200e and the BET method, a model isotherm based on adsorption of gas on a surface. Industrial hemp shiv was supplied by La Chanvrière De L'aube in central France.

Table 1. Properties of the pozzolan

Pozzolan	SiO_2	Al_2O_3	CaO	Fe_2O_3	SO_3	K_2O	MgO	Rate of Amorph-ousness	Surface area m^2/g	Mineral composition
GGBS	34.1	13.9	39.3	0.4	2.4	0.3	8.6	Totally	2.65	no crystalline fraction
Metakaolin	51.4	45.3	-	0.5	-	2.1	0.6	Mostly	18.30	quartz, tohdite, aluminum oxide, wollastonite and paragonite.
RHA	93.8	1.9	0.7	0.3	-	1.4	0.5	Mostly	13.70	quartz and crystobalite

As shown in Table 1, the chemical and mineral composition, rate of amorphouseness and surface area of pozzolans (Walker & Pavía, 2010; Walker & Pavía, 2011).

2.2 Setting Time

It is not possible to determine the setting time of composites such as hemp concrete using the Vicat test as the organic aggregate impedes needle penetration and absorbs water; hastening the drying of the paste and giving inaccurate results. Therefore, the hemp aggregate was replaced by hemp water; and the effect of hemp on setting determined by comparing the Vicat test results of pastes made with water and hemp water. Mixing was in accordance with EN 459-2 except for the addition of the pozzolan (added after 1 minute and the mixing stopped for 30 seconds).

The hemp water was prepared by soaking the shiv for 45 minutes so that it releases its water soluble constituents including pectins. The concentration of soluble hemp compounds in the mixing water present in the lime hemp concrete during curing was not established. Longer soaking times would yield a higher concentration of soluble compounds, however it was felt that long soaking times in a water excess were not representative of the actual conditions in hemp concrete, thus soaking the shiv for 45 minutes was deemed an adequate solution. The influence of varying amounts of soluble hemp compounds on setting was measured by varying the hemp water content (0, 25, 50 and 100%).

2.3 Water Content for Setting

Consistency in the water content is of paramount importance as it affects the kinetics of the binder reactions and the final properties of the material: a small water increase significantly delays setting of lime-pozzolan pastes (Walker & Pavía, 2010). A standard consistency for the lime-pozzolan pastes was achieved by adding the amount of water necessary to produce a paste with a 165 mm initial flow diameter. The water required in order to produce such paste was measured according to EN 459-2. The quantity of water required by different

pozzolans to produce a paste of the same standard consistency (necessary for the Vicat test) varies: GGBS has a much lower water demand than lime while, in contrast, lime and metakaolin have a similar water demand (Walker & Pavía, 2011). For the lime- GGBS pastes, the binder: water ratio of 1:0.69 and 1:0.64 for the 30% and 37.5 % (Figure 2) GGBS content respectively. As hydrated lime and metakaolin have a similar water demand, the water content of the lime- metakaolin pastes was determined at 37.5% pozzolan content and fixed at a lime+pozzolan:water ratio of 1:0.93 (by weight) for both pozzolan contents.

2.4 Compressive and Flexural Strength

Strength was measured at 30% pozzolan content with the water content adjusted to produce a 165 mm initial flow diameter. The prisms were demoulded after 1 day and stored in a curing room at 20°C±3°C and RH 60%±10%. The unconfined compressive strength was measured according to EN196-1 and EN 459-2 at 28 days.

Flexural strength tests were conducted according to EN196-1 and EN 459-2 using the center-point loading method. Here, the prisms were placed on fixed supports with the longitudinal axis normal to the applied load. After breaking the prism, the following equation was used to determine the flexural strength:

$$R_f = (1.5 \times F_f \times l)/b^3 \quad (1)$$

R_f flexural strength (N/mm^2)

F_f load applied to the middle of the prism at fracture (N)

b side of the square section of the prism (mm)

l distance between the supports (mm)

The values reported are the mean of 6 compressive and 3 flexural strength tests.

2.5 Analysis of Hydration Products With Scanning Electron Microscopy (SEM)

SEM and XRD were used to determine whether water soluble constituents of hemp were responsible for a difference in the nature and/or amount of hydrates. The microstructure of the binder and the formation of hydrates were investigated using a Tescan MIRA Field Emission SEM. The samples were fractured and covered with a gold coating in an 'Emscope SC500' plasma coating unit. Lime- pozzolan pastes (30% pozzolan by weight) were investigated at 1, 3, 7 and 28 days. Pastes with 2% hemp content (untreated and washed hemp in which the hemp was immersed in water for 24 hours and then dried prior to mixing) were investigated at 28 days. 15 random areas were analyzed in each sample.

XRD was undertaken on the lime- pozzolan pastes, at different ages up to 6 months, using a Phillips PW1720 XRD with a PW1050/80 goniometer and a PW3313/20 Cu k-alpha anode tube at 40 kV and 20 mA.

2.6 Testing Regime

The testing regime of the different pastes is as set out in Table 2.

Table 2. Matrix of testing

Property	Test	Pozzolan	Pozzolan Content	Additions	Figure
Setting	Vicat Test	Lime, GGBS, metakaolin, RHA	37%	Hemp water	Section 3.1, Figure 2
Setting	Vicat Test	GGBS, metakaolin	30%	Hemp water (0-100%)	Section 3.1, Figure 3
Compressive strength	EN196-1 EN459-2	Lime, GGBS, metakaolin	30%	Hemp water	Section 3.2, Figure 4, 5
Flexural strength	EN196-1 EN459-2	Lime, GGBS, metakaolin	30%	Hemp water	Section 3.3, Figure 6
Microstructural analysis	SEM	GGBS, metakaolin, RHA	30%	Hemp water	Section 3.4, Figure 7, 8
Microstructural analysis	SEM	GGBS, metakaolin, RHA	30%	Hemp particles	Section 3.4, Figure 9, 10

As shown in Table 2, the testing undertaken in this research.

3. Results and Discussion

3.1 Effect of Water-Soluble Hemp Components on Setting Time

The pozzolanic reaction is significantly controlled by the pozzolan's active silica and alumina content (Massazza, 2007). The pozzolans have a different composition ranging from the clinker-bearing GGBS to the alumina-rich metakaolin and the silica-rich RHA. As aforementioned, RHA was introduced in order to ascertain the effect of the hemp on an almost fully siliceous pozzolan. A 100% calcium lime paste was included as a control sample.

The results show that hemp's soluble constituents do not alter the setting time of lime: both the lime and the lime/hemp-water pastes display a similar set, with the final set at 110 hours and a maximum deviation of 9 hours (Figure 2). This indicates that the hemp does not alter mechanical processes such as flocculation, drying and early carbonation responsible for the initial hardening of lime. In contrast, the hemp water retards the setting of lime- pozzolan pastes. RHA is retarded the most followed by GGBS and metakaolin: 39, 23 and 10 hours respectively for a setting equivalent to a depth of penetration of the Vicat needle of 25 mm (Figure 2). Therefore, the hemp delays pozzolanic reaction and the amount of retardation is partially determined by the chemical composition of the pozzolan.

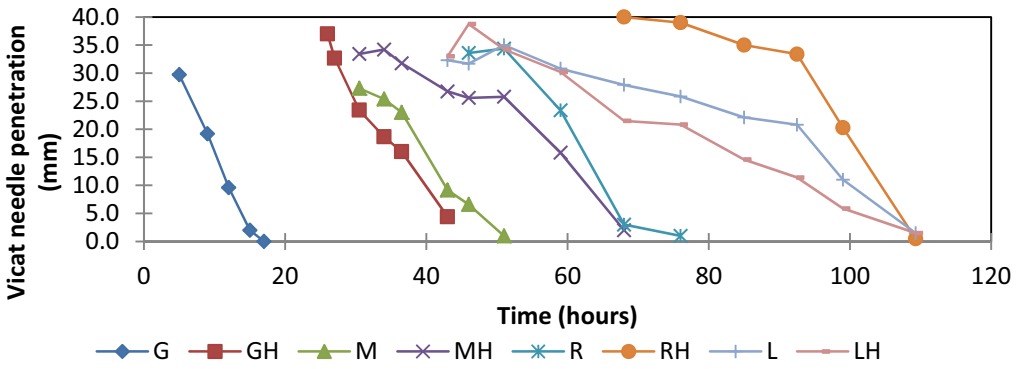

Figure 2. Setting time of lime (L) and lime- pozzolan pastes, with and without hemp water. G-GGBS; M-metakaolin; R-RHA; H-hemp water. All 37.5% pozzolan content by weight

It could be argued that the retardation of the set is due to the water soluble hemp constituents retaining water in the binder rather than delaying pozzolanic reaction. However, the samples were continuously weighed during drying, and the similar drying rates of all samples (with and without hemp water) indicate that there is no water retention triggered by the water soluble hemp constituents. Therefore the set retardation is due to the soluble hemp constituents interfering with the lime-pozzolan reactions responsible for setting.

The setting of the most siliceous pozzolan (RHA) is retarded the most; the initial set starts late (at approximately 80 hours). In contrast, the setting of the alumina-rich pozzolan paste (metakaolin) is delayed the least, despite the fact that it contains more soluble hemp compounds due to its greater water demand (section 2.3). This suggests that the hydration of silica is retarded to a greater extent than that of alumina and agrees with previous authors stating that retardation by pectins is greater for low C_3A cement (Peschard, Govin, Grosseau, Guilhot & Guyonnet, 2004).

In order to assess the influence of increasing amounts of soluble hemp compounds on setting, the Vicat test was repeated with varying hemp water concentrations (ranging from 0% to 100%) for the GGBS and metakaolin pozzolans. It is evident from the results (Figure 3) that increasing hemp water content increases the delay in setting. This was true in all cases except for the metakaolin paste with hemp water content over 50% and this may be due to the presence of a surplus of soluble hemp constituents on account of the higher water content in the lime- metakaolin pastes. It was also evidenced that a small amount of hemp water (25%) significantly delays setting.

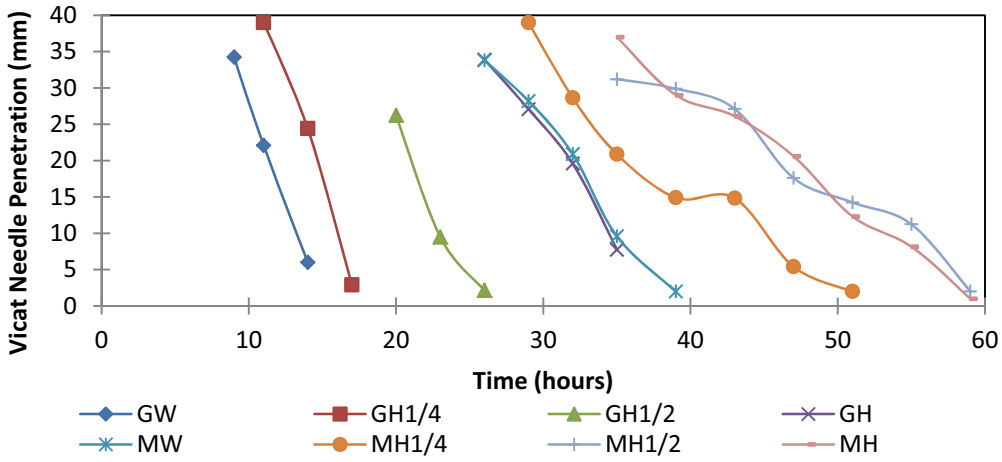

Figure 3. Influence of increasing soluble hemp compounds on the setting of lime- pozzolan pastes. G-GGBS; M-metakaolin; W=100% water; H1/4=25% hemp water and 75% water; H1/2=50% hemp water; H=100% hemp water. All 30% pozzolan by weight

3.2 Effect of Water-Soluble Hemp Components on Compressive Strength

The impact of the soluble constituents of hemp on compressive strength was investigated in samples of 30% pozzolan content (by weight) made with water and hemp water, at 5, 7, 14 and 28 days (Figure 4). The lime samples at 5 days were still soft and compressive strength was therefore only investigated at 7, 14 and 28 days. The low coefficients of variation (Table 3) indicate that the results are reliable.

The results indicate that the hemp does not affect the strength development of lime pastes however, it delays the strength development of lime-pozzolan pastes (Figure 4); in particular that of the metakaolin. The pozzolanic reaction contributes to strength development and it is evident that the hemp water delays this reaction. This agrees with the setting results indicating that hemp delays pozzolanic reaction. It differs from the setting results in that metakaolin is delayed further than GGBS. However, as strength development is largely attributed to the formation of silica hydrates, it is clear that the hemp water is delaying their formation.

The magnitude of strength reduction gradually decreases over time and, at 28 days, the pozzolan pastes made with water and hemp water show similar strength. Therefore, the soluble hemp constituents undermine early strength but do not significantly affect ultimate strength.

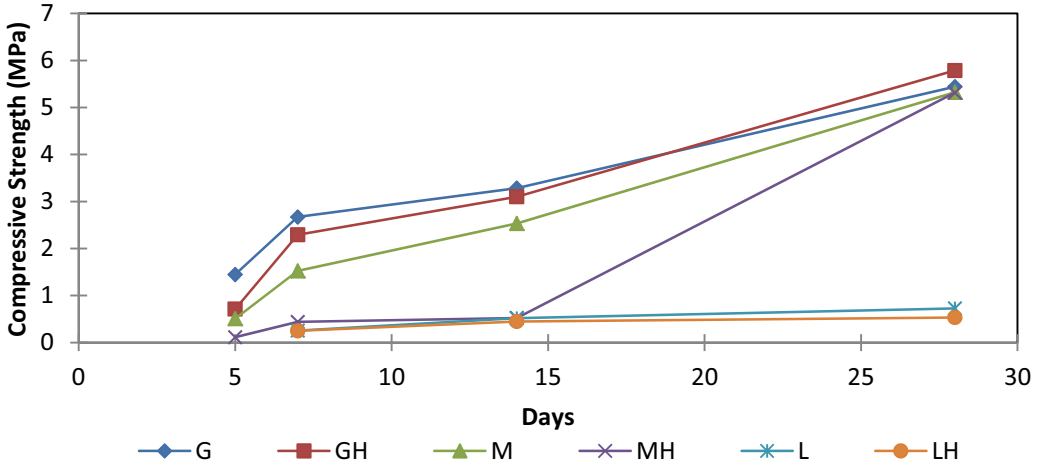

Figure 4. Influence of hemp soluble components on the compressive strength development of lime and lime-pozzolan pastes. G-GGBS; M-metakaolin; L-lime; H-hemp water. All 30% pozzolan content

Table 3. Coefficient of variation of the compressive strength results in Figure 4

specimen→	G	GH	M	MH	L	LH
5 days	5.04	11.69	16.71	6.58		
7 days	8.2	9.2	5.44	10.93	5.68	17.3
14 days	9.68	6.45	7.44	2.38	6.35	12.04

In order to confirm that the soluble hemp components produce a delay in compressive strength development, the compresive strength test was repeated using aluminium sulphate as an additive. Aluminium sulphate precipitates pectins and should therefore reduce the effect of pectin on the lime-pozzolan reaction. The results (Figure 5) show that aluminium sulphate has no impact on the strength development of pastes made with water but improves the strength of pastes made with hemp water (in particular that of the metakaolin paste whose strength was lowered the most). This further confirms that the soluble hemp components (in particular pectin) cause a delay in compressive strength development.

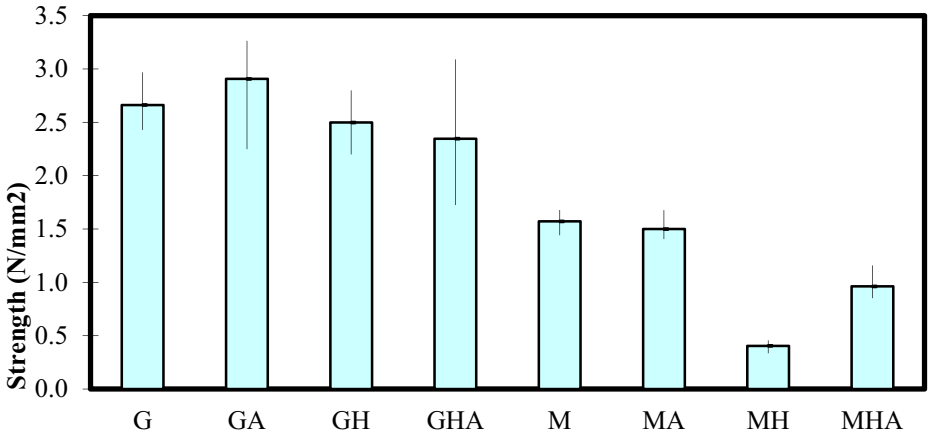

Figure 5. Influence of soluble hemp components on the early compressive strength of lime- pozzolan pastes with and without aluminium sulphate additive at 7 days. G-GGBS; M-metakaolin; L-lime; H-hemp water; A-aluminium sulphate

3.3 Effect of Water-Soluble Hemp Components on Flexural Strength

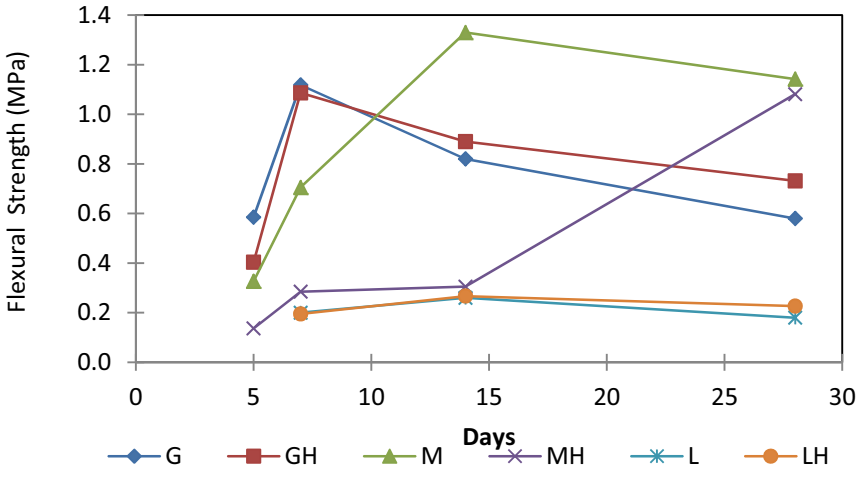

Figure 6. Flexural strength development of pastes over time. G-GGBS; M-metakaolin; L-lime; H-hemp water. All 30% pozzolan content

The early strength reduction caused by the hemp water is also clear in the flexural strength results. The hemp does not affect the flexural strength development of lime pastes but it delays that of the lime-pozzolan pastes (Figure 6). In addition, the early flexural strength gain of the GGBS is hardly affected whereas that of the metakaolin is lowered significantly by the presence of hemp water. These agree with compressive strength results. The low coefficients of variation (Table 4) indicate that the results are reliable.

A reduction in flexural strength of the lime-metakaolin paste made with water (M) is observed between 14 days and 28 days. This aggrees with previous authors (Donchev et al., 2010) and it is probably due to the transformation of hydration phases. The metakaolin sample made with hemp water will likely undergo a similar strength reduction over time which is not shown in the graph as a result of its delayed strength development. The lime-GGBS pastes also exhibited strength reduction and became brittle upon hardening.

Table 4. Coefficient of variation of the flexural strength results in Figure 6

specimen→	G	GH	M	MH	L	LH
5 days	2.56	11.68	13.76	9.13		
7 days	1.90	8.40	7.80	6.00	4.08	2.56
14 days	18.29	22.47	14.28	11.47	7.69	6.37

3.4 Effect of Water-Soluble Hemp Components on Hydration (XRD and SEM Results)

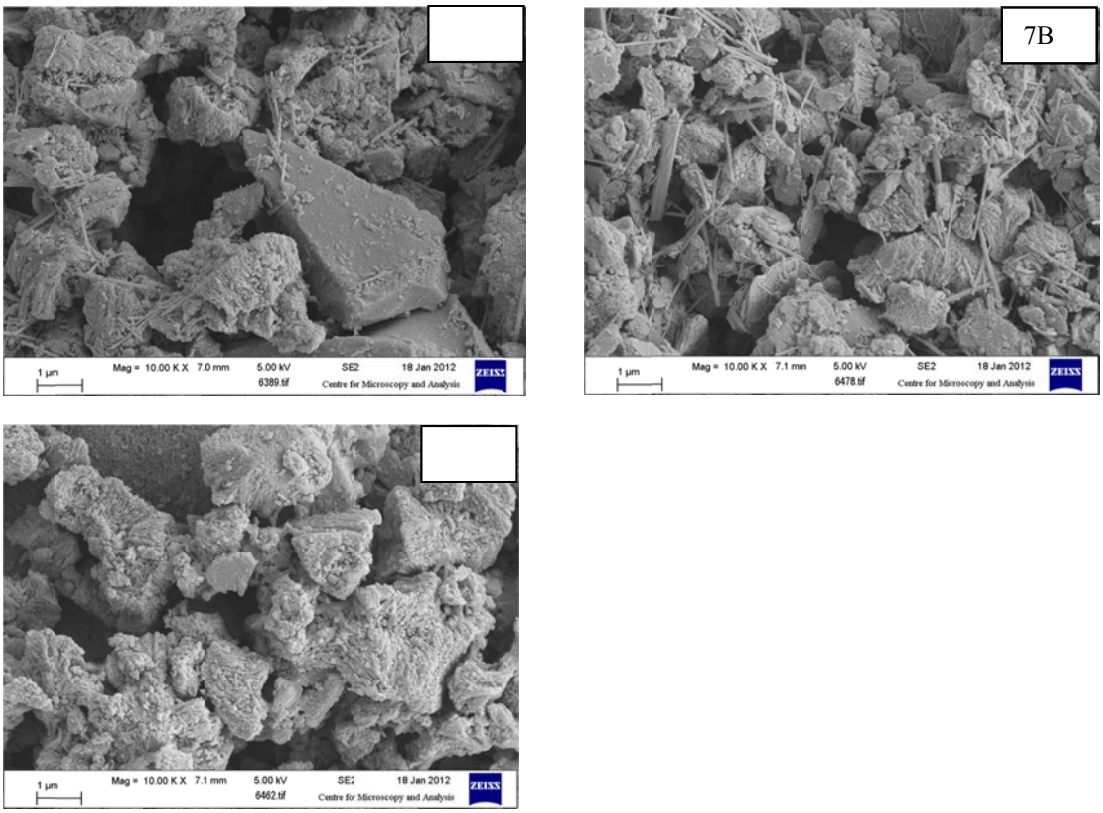

Figure 7. SEM micrographs of lime-pozzolan pastes made with hemp-water at 24 hours of curing

7A (GGBS) and 7B (metakaolin) pastes showing hydrates with needle morphology formed as a result of the pozzolanic reaction.

7C (RHA paste) showing carbonation and no pozzolanic reaction products.

It was attempted to use XRD to determine whether the water soluble hemp constituents were responsible for a difference in the nature/ amount of hydrates formed upon pozzolanic reaction. Pastes were analysed at different ages up to 6 months however, no hydration products were detected using XRD. This was attributed to their amorphous character, low amount (XRD limit of detection is approximately 5%) and/or concealment by other mineral peaks.

In contrast, a substantial amount of hydrates were observed in the lime-pozzolan pastes under SEM. A significant amount of hydrates were found early (at 24 hours of curing), in all lime- pozzolan pastes except in the RHA paste made with hemp-water (Figure 7). In all pastes, the morphology of the hydrates changes over time, from predominantly needle-shape at early ages to sponge and gel types at later ages. The composition of these hydrates could not be analysed due to technical limitations however, based on their morphology, the sponge and gel types as well as some of the low-crystallinity fibrous phases are likely CSH.

In the RHA pastes, there was a clear difference in the quantity of hydration products in the samples made with water and hemp water: at 1 and 3 days, there were few needle-shaped hydrates in the water pastes and none in the hemp-water pastes while at 7 days, needles and sponge type hydrates were present in the water pastes and needles begin to appear in the hemp-water pastes (Figure 8). This agrees with the setting and strength results indicating that hemp water delays hydration of silicates to form CSH.

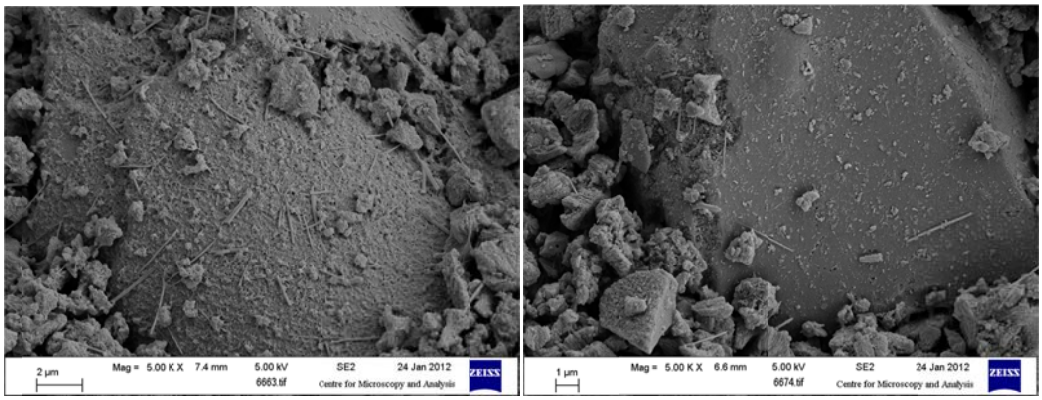

Figure 8. SEM micrographs of RHA pastes at seven days of curing showing a clear difference in the amount of hydration products. Left image: RHA particle coated with hydrates in a paste made with water. Right: RHA particle in the paste made with hemp water showing few hydrates

In the GGBS and metakaolin pastes, it was not possible to determine whether the hemp water had influenced pozzolanic reaction as there was no discernable difference in neither the type nor the amount of hydrates between the water and hemp water pastes at any stage (1, 7, 14, and 28 days).

SEM was also undertaken at the interface between the lime-pozzolan paste and the hemp particles. Very few hydrates were present on the hemp particles despite abundant hydrates being visible in the paste (Figure 9 and 10). Furthermore, when the hemp particles were washed to remove the water soluble constituents prior to mixing, a small amount of hydrates appeared on the particles (Figure 11) –a much smaller amount than that in the paste. This suggests that, not only the soluble hemp compounds but also the hemp particle itself contributes to the lack of hydration. An analogy can be drawn with mortar-brick interfaces, where the presence of limited hydrates has been attributed to the dewatering of the mortar as a result of high suction by the brick, reducing the water available for hydration (Reda & Shrive, 2001 referring to Goodwin & West, 1982). This is particularly important in lime-pozzolan binders because pozzolanic reaction starts early but is slow and therefore the presence of water is required for a long time period.

The hemp particle is a carbon dioxide reservoir as it holds air in its porous structure. It is likely that the carbonated zone on the hemp particle interface (Figures 9 and 10 – left image) is assisted by the diffusion of CO_2 supplied by the particle. This would agree with Brocken and Larbi (1999) who attributed the carbonated zone at the mortar brick interface to CO_2 supplied by the brick by diffusion. The prevalence of calcium carbonate may also be influenced by high mobility of calcium ions in a water environment caused by the high absorption of the shiv (as observed by Savastano and Agopyan (1999) for other vegetable fibres in a cement paste). In addition,

the alkaline degradation of the shiv may also provide CO_2 for carbonation of the portlandite, as observed by Govin, Peschard, & Guyonnet (2006) in a cement paste with wood.

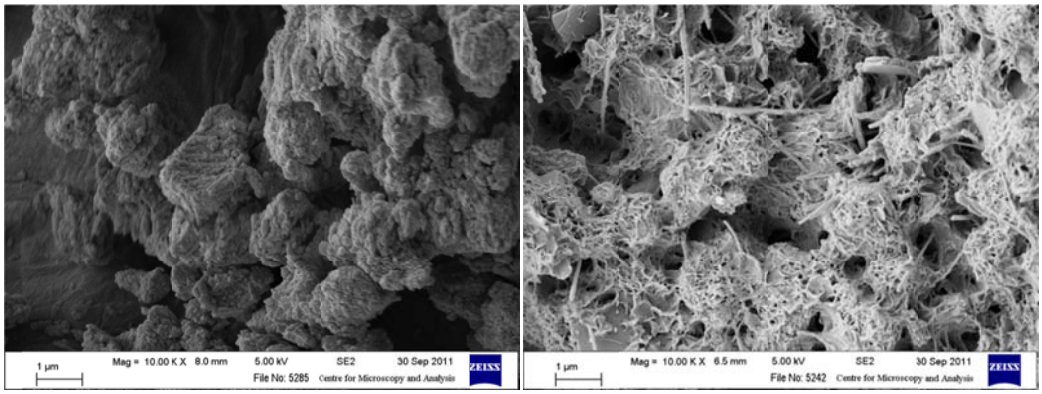

Figure 9. SEM micrographs of the lime-GGBS specimens at 28 days.

Left image: hemp interface showing carbonated lime and very few hydrates.

Right image: paste including hydrates with needle and sponge morphologies.

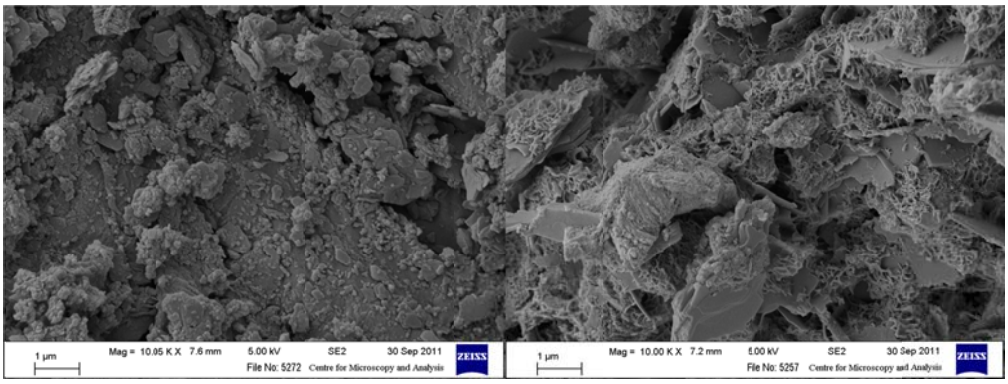

Figure 10. SEM micrographs of the lime-metakaolin specimens at 28 days

Left image: hemp interface showing carbonated lime and no hydrates.

Right image: paste including hydrates with needle and sponge morphologies.

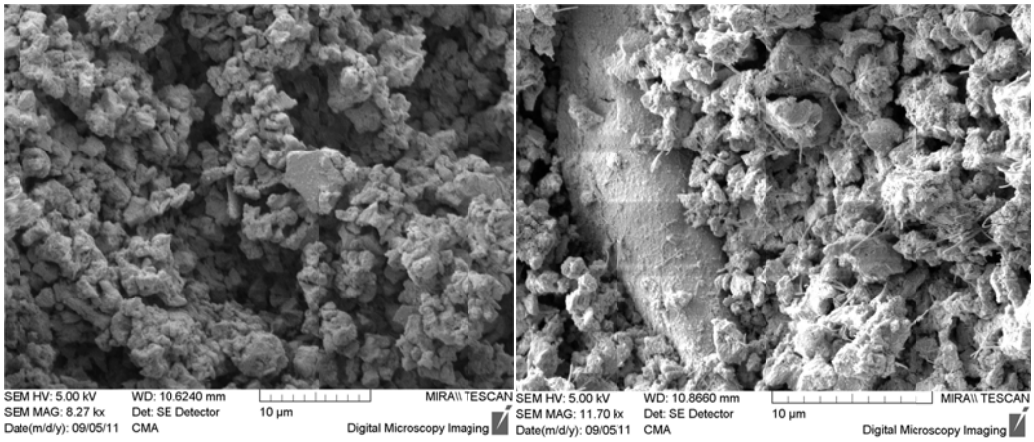

Figure 11. Morphology of the lime-GGBS specimens at the hemp particle interface at 7 days. Left image: unwashed hemp particle showing carbonated lime and no hydration. Right image: surface of a washed hemp particle with some hydrates

4. Conclusion

The water-soluble hemp components delay hydration. As a result, they retard the setting and early strength development of lime-pozzolan pastes however, they do not affect their ultimate strength. In contrast, the soluble hemp compounds do not impact the setting, hardening and initial strength development of calcium lime pastes. The results also revealed that the water-soluble hemp components delay the formation of silica hydrates further than alumina hydrates.

It was noted that a small amount of hemp water significantly halts hydration. The effect of hemp water does not increase linearly with concentration; at high hemp water contents, increasing concentration has a smaller effect. This is likely on account of a surplus of active hemp components in solution.

The SEM analysis agreed with the setting and strength results indicating that hemp water delays the formation of hydrates. This was clearly evident in the lime-RHA pastes in where a delay in the formation of CSH was readily observed.

The halt of the pozzolanic reaction by the hemp particles was clear at the hemp interface, where few hydration products appeared and their quantity slightly increased when the hemp particles were washed to remove their water soluble constituents. This paper concludes that the properties of the hemp particles, including their high suction removing water at the interface and their high porosity assisting CO_2 diffusion, contribute to the halt of the pozzolanic reaction.

This research also evidenced that pozzolanic reaction takes place early in lime-pozzolan pastes (significant hydrates were observed at 24 hours). An evolution in the morphology of the pozzolanic hydrates over time, from predominantly needle-shaped at very early ages (24 hours); into fibrous, sponge and gel-like hydrates at later stages, was determined.

Acknowlegements

The authors wish to thank the Environmental Protection Agency for funding this research. The authors also thank the Traditional Lime Company, Clogrennane Lime and Ecocem for the provision of materials and also Dr Heath Bagshaw, Mr. Neal Leddy and Mr. Colin Reid (Centre for Microscopy and Analysis) and Dr. Robbie Goodhue (Geology Department) for their help with the SEM and XRD respectively.

References

Beaudoin, J. J., & Ramachandran, V. S. (1992). A new perspective on the hydration characteristics of cement phases. *Cement and Concrete Research, 22*, 689-694. http://dx.doi.org/10.1016/0008-8846(92)90021-M

Bogue, R. H., & Lerch, W. (1934). Hydration of Portland Cement Compounds. *Industrial & Engineering Chemistry Research, 26*, 837-847.

Brocken, H. J. P., & Larbi, J. A. (1999). Composition of mortar as a function of distance to the brick-mortar interface: a study on the formation of cured mortar structure in masonry using NMR, PFM and XRD. *Heron, 44*, 257-270.

Dalmay, P., Smith, A., Chotard, T., Sahay-Turner, P., Gloaguen, V., & Krausz, P. (2010). Properties of cellulosic fibre reinforced plaster: influence of hemp or flax fibres on the properties of set gypsum. *Journal of Material Science, 45*, 793-803. http://dx.doi.org/10.1007/s10853-009-4002-x

de Silva, P. S., & Glasser, F.P. (1993). Phase relations in the system CaO-Al2O3-SiO2-H2O relevant to metakaolin - calcium hydroxide hydration. *Cement and Concrete Research, 23*, 627-639. http://dx.doi.org/10.1016/0008-8846(93)90014-Z

Donchev, I., Nivov, J., Doykov, I., Petrova, N., & Dimova, L. (2010). On the formation of cement phases in the course of the interaction of kaolinite with CH. *Journal of the University of Chemical Technology and Metallurgy, 45*, 391-396.

EN 196-1 Methods of testing cement. Determination of strength. (2010). European Committee for Standardisation CEN, Brussels.

EN 459-2 Building lime, part 2: Test Methods. (2010). European Committee for Standardisation CEN, Brussels.

EN 459-Building lime. Part 1: Definitions, specifications and conforming criteria. (2010). European Committee for Standardisation CEN, Brussels.

Fang, Y., Al-Assaf, S., Phillips, G., Nishinari, K., Funami, T., & Williams, P. (2008). Binding behavior of calcium to polyuronates: Comparison of pectin with alginate. *Carbohydrate Polymers, 72*, 334-341. http://dx.doi.org/10.1016/j.carbpol.2007.08.021

Goodwin, J. F., & West, W. H. (1982). A Review of the Literature on Brick/Mortar Bond. *Proceedings of the British Ceramic Society, 30*, 23-37.

Govin, A., Peschard, A., & Guyonnet, R. (2006). Modification of cement hydration at early ages by natural and heated wood. *Cement and Concrete Composites, 28*, 12-20. http://dx.doi.org/10.1016/j.cemconcomp. 2005.09.002

He, C., Makovicky, E., & Osbæck, B. (1994). Thermal stability and pozzolanic activity of calcined kaolin. *Applied Clay Science, 9*, 165-187. http://dx.doi.org/10.1016/0169-1317(94)90018-3

Kavasa, T., Olgunb, A., Erdoganb, Y., & Oncec G. (2007). The effect of pectin on the physicochemical and mechanical properties of cement containing boron. *Building and Environment, 42*, *1803*-1809. http://dx.doi.org/10.1016/j.buildenv.2006.01.018

Massazza, F. (2007). Pozzolana and pozzolanic cements. In P. C. Hewlett (Ed.), *Lea's chemistry of cement and concrete* (pp. 471-602). UK: Elsevier.

Murat, M. (1983). Hydration reaction and hardening of calcined clays and related minerals. I. Preliminary investigation on metakaolinite. *Cement and Concrete Research, 13*, 259-266. http://dx.doi.org/10.1016/0008-8846(83)90109-6

Peschard, A., Govin, A., Grosseau, P., Guilhot, B., & Guyonnet, R. (2004). Effect of polysaccharides on the hydration of cement paste at early ages. *Cement and Concrete Research, 34*, 2153-2158. http://dx.doi.org/10.1016/j.cemconres.2004.04.001

Ramachandran, V. S., Feldman, R. F, & Beaudoin, J. J. (1981). *Concrete Science*. London: Heyden & Son Ltd.

Reda Taha, M. M., & Shrive, N. G. (2001). The use of pozzolans to improve bond and bond strength. *Proceedings of the 9th Canadian Masonry Symposium*. University of New Brunswick. Canada.

Renard, C., & Thibault, J. F. (1996). Degradation of pectins in alkaline conditions: kinetics of demethylation. *Carbohydrate Research, 286*, 139-150. http://dx.doi.org/10.1016/0008-6215(96)00056-0

Rojas, M. F., & Cabrera, J. (2002). The effect of temperature on the hydration rate an d stability of the hydration phases of metakaolin-lime-water systems. *Cement and Concrete Research, 32*, 133-138. http://dx.doi.org/ 10.1016/S0008-8846(01)00642-1

Savastano, Jr H., & Agopyan, V. (1999). Transition zone studies of vegetable fibre-cement paste composites. *Cement and Concrete Composites, 21*, 49-57. http://dx.doi.org/10.1016/S0958-9465(98)00038-9

Sedan, D., Pagnoux, C., Chotard, T., Smith, A., Lejolly, D., Gloaguen, V., & Krausz, P. (2007). Effect of calcium rich and alkaline solutions on the chemical behaviour of hemp fibres. *Journal of Material Science, 42*, 9336-9342. http://dx.doi.org/10.1007/s10853-007-1903-4

Walker, R., & Pavía, S. (2010). Behaviour and properties of lime- pozzolan pastes. In W. Jäger, B. Haseltine, & A. Fried (Eds.), *8th International Masonry Conference* (pp. 353-362). Dresden.

Walker, R., & Pavía, S. (2011). Physical properties and reactivity of pozzolans, and their influence on the properties of lime-pozzolan pastes. *Materials and Structures, 44*, 1139-1150. http://dx.doi.org/10.1617/s11527-010-9689-2

Young, J. (1972). A review of the mechanisms of set-retardation in portland cement pastes containing organic admixtures. *Cement and Concrete Research, 2*, 415-433. http://dx.doi.org/10.1016/0008-8846(72)90057-9

Zsivanovits, G., MacDougall, A., Smith, A., & Ring, S. (2004). Material properties of concentrated pectin networks. *Carbohydrate Research, 339*, 1317-1322. http://dx.doi.org/10.1016/j.carres.2004.02.027

Journal of Materials Science Research; Vol. 3, No. 3; 2014
ISSN 1927-0585 E-ISSN 1927-0593
Published by Canadian Center of Science and Education

100 MeV Si^{7+} Ion Irradiation Induced Modifications in Electrical Characteristics of Si Photo Detector: An In-Situ Reliability Study

M Vinay Kumar[1], Shammi Verma[2], V Shobha[3], B Jayashree[4], D Kanjilal[2], Ramani[5] & S Krishnaveni[1]

[1] Department of Studies in Physics, University of Mysore, Mysore, India

[2] Inter University Accelerator Centre (IUAC), New Delhi, India

[3] Laboratory for Electro-Optics Systems (LEOS), Bangalore, India

[4] Department of Physics, Maharanis Science College for Women, Bangalore, India

[5] Department of Physics, Bangalore University, Jnanabharathi, Bangalore, India

Correspondence: S Krishnaveni, Department of Studies in Physics, University of Mysore, Mysore-570006, India. Tel: 91-984-402-3568. E-mail: sk@physics.uni-mysore.ac.in

Received: May 20, 2014 Accepted: June 13, 2014 Online Published: June 18, 2014

doi:10.5539/jmsr.v3n3p24 URL: http://dx.doi.org/10.5539/jmsr.v3n3p24

Abstract

The influence of 100 MeV Silicon (Si) ion irradiation on electrical characteristics of Si photo detectors has been analyzed using in-situ current-voltage characterization (I-V) in dark condition. The irradiation was performed over a wide range of fluences from 1×10^{11} ions/cm^2 to 1×10^{13} ions/cm^2. Key electrical parameters such as ideality factor (n), series resistance (R_s) and reverse bias leakage current (I_R) for each irradiation fluence have been extracted from the I-V characteristics. The ideality factor of the unirradiated detector is found to be 1.48 and it gradually increased up to the fluence of 5×10^{11} ions/cm^2, then it saturates around 3.4-3.5 for higher fluences. The I-V characteristics showed significant increase in forward bias and drastic increase in reverse leakage current. The value of I_R is 7.23 nA for unirradiated detector and it increases about four orders of magnitude up to 5×10^{11} ions/cm^2. Further there is no observable change in the value of I_R. However the value of R_s increases initially and slightly decrease at higher fluences. The observed results are interpreted in terms of energy loss mechanisms of swift heavy ion as it passes through the different layers of the detector. The radiation induced defects in the bulk region and activation of multiple current transport mechanisms have attributed to the observed deviations in the electrical behaviour of the device. SRIM (Stopping power and Range of Ion in Matter) and TRIM (Transport and Range of Ion in Matter) simulation results of damage induced in the device have been reported in the present study. Linear energy transfer (LET), non ionizing energy loss (NIEL) damage contributions, total ionization dose (TID) and displacement damage dose (D_d) has been correlated with the observed degradation. Quantitative estimation of radiation hardness of the Si photo detector is done by comparing with the equivalent damage created by the proton at similar penetration depth in the present device structure.

Keywords: Si photo detectors, swift heavy ion irradiation, space application, radiation hardness, current transport, NIEL, LET

1. Introduction

The Si Photo detectors are major part of several electro-optical instruments used in space and military applications. Also, these are being used extensively for energy and position measurements in particle and nuclear physics experiments (Kurokawa et al., 1995). In such experiments the detectors are exposed to typically 100 Mrad in their operational lifetime (Gill, Hall, & MacEvoy, 1997). Hence these devices need to be radiation hardened to function reliably. The effect of protons, electrons, neutrons and gamma rays on Si photo detectors of various configurations such as p-n junction/n-p junction devices and p-i-n structures are reported (Krishnan, Sanjeev, & Pattabi, 2007; Pillai et al., 2012; Moloi & McPherson, 2009). However the effect of swift heavy ion (SHI) on photo detectors, particularly high energy heavy ion has not been reported extensively. It is well documented in the literature that SHI irradiation in semiconductors can create latent tracks, induce modifications such as vacancies, di-vacancies, point defects etc (Bolse & Beate, 2002; Levalois & Marie, 1999; Kanjilal, 2001). The damage created depends largely on the type of incident particles and values of LET and NIEL. LET is the sum of electronic and nuclear energy losses and plays an important role in case of heavy ions (Leroy & Rancoita,

2009). NIEL is the rate at which energy is lost to non ionizing events. Most of the earlier work focused on NIEL induced displacement damage by lighter particles and there are limited reports on the contribution of LET and NIEL by SHI (Bourqui et al., 2008; Zelijko, Milko, Gabor, Mihlay, & Aliz, 2009; Prabhakara Rao, Praveen, Rejeena Rani, Tripathi, & Gnana Prakash, 2013). Hence the present study is of significant interest both fundamentally and technically to understand the mechanism of ion solid interaction and to improve the device fabrication technology leading to more radiation hard electronic circuitry.

The objective of this work is to study the effect of 100 MeV Si ion irradiation on the electrical characteristics of Si photo detector through in-situ I-V measurements in dark condition. The in-situ measurements are done on the same sample to avoid discrepancy in the measured parameters due to variation of initial conditions of the device. The current transport mechanism has been analyzed by extracting the key electrical parameters such as ideality factor, series resistance and revere leakage current. The interaction of ion beam with the device is analyzed by energy loss mechanisms and interpreted with the aid of SRIM code (J. Ziegler, M. Ziegler, & Biersack, 2010). The ionization and displacement damage simulation has been performed using TRIM and results are presented. The observed degradation is explained in terms of LET, NIEL, TID and D_d. Finally with the aid of SRIM, we present quantitative estimation of radiation hardness of the present device by comparing with the equivalent damage created by proton at similar penetration depth.

2. Experiment

The Silicon photo detector used in the present study having $n^+/p/p^+$ structure and the cross section of the device is as shown in Figure 1. The top n^+ layer is achieved by the implantation of phosphorous ion into mono crystalline p-Si <100> wafer of thickness 300 µm with resistivity of 10 Ω.cm. A p^+ layer of aluminum (approximately 1 µm thick) was created at the rear surface by sputtering and subsequent annealing. This will serve as both Back Surface Field (BSF) and Back Surface Reflector (BSR). On the front surface tri-layer metal coating of Ti/Pd/Ag of suitable thickness was applied for contact purpose. Similar metallic coating was done at rear surface. Silicon oxy nitride was deposited as antireflection coating on the active area of the device using ion beam sputtering process. The device is having total thickness of 305 µm approximately and area of 5 mm^2.

The Si photo detector was irradiated at room temperature with 100 MeV Si^{7+}ion from 15 UD Pelletron at Inter University Accelerator Center (IUAC), New Delhi, India. A low beam current of about 1 pnA (particle nano ampere) was maintained throughout the experiment to avoid sample heating. The vacuum of the irradiation chamber was 1×10^{-6} mbar. The irradiation was performed over wide range of ion fluences from 1×10^{10} to 1×10^{13} ions/cm^2 to study in detail the modifications induced by Si ion beam on the electrical characteristics of the detector. Schematic representation of irradiation of Si photo detector inside the vacuum chamber is depicted in Figure 2.

In-situ I-V characterization (in dark condition) was performed using Keithley 2400 source meter and LabVIEW program. The dark condition was achieved by covering all the windows of irradiation chamber and switching off the camera light inside. The I-V characteristics were recorded within 15 minutes of each irradiation fluence by stopping the ion beam momentarily using Faraday cup in the beam line. The terminals of the photo detector were floating during irradiation.

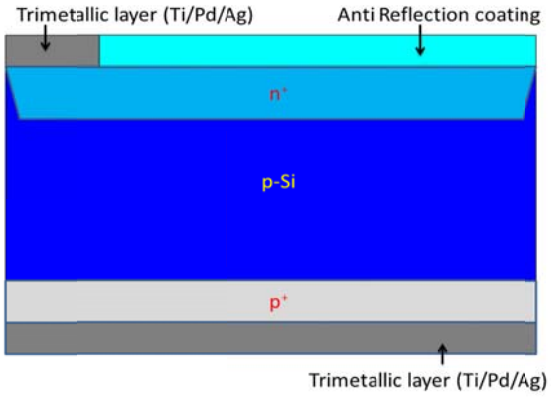

Figure 1. Structure of Si photo detector

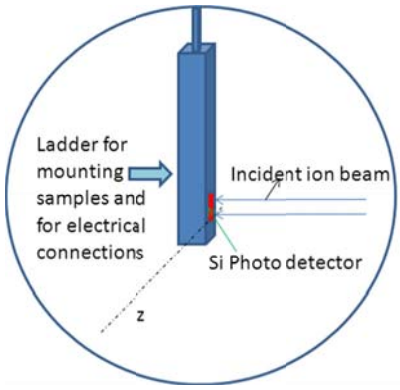

Figure 2. Schematic representation of 100 MeV Si ion irradiation on Si Photo detector inside the vacuum chamber

3. Results and Discussion

3.1 SRIM/TRIM Simulation Results

SRIM/TRIM simulation software is widely used to estimate the values of stopping power and range of ions in matter. In the present study we have used SRIM 2013 program to study the passage of 100 MeV Si ion beam through the Si photo detector. It is well known that as the swift heavy ion (SHI) traverses through the target material, the ion loses its energy via two processes:

1) Nuclear energy loss (S_n)

2) Electronic energy loss (S_e)

S_n is due to elastic scattering by target nuclei whereas S_e is due to inelastic interaction with target electrons. Also S_e is known to dominate at higher energy regime (>1 MeV/amu) compared to S_n which dominates at lower energy regime (<1 keV/amu). The observed modification in electrical properties can be understood by analyzing the possible implications of passage of ion through the device structure.

The passage of 100 MeV Si ion through different regions of the Si photo detector (only active region is considered) is analyzed through SRIM code and a plot of S_e and S_n versus depth of the material is depicted in Figure 3. It is clear from the Figure that the device suffers non uniform irradiation and the ion stops deep in the substrate away from the n^+/p junction. The value of S_e and S_n at this junction is 2.48 keV/nm and 1.96×10^{-3} keV/nm respectively. It is noteworthy that the value of S_e is almost 1000 times greater than the values of S_n. It may be recalled that nuclear energy loss is known to create defects like vacancies interstitials etc. whereas high electronic energy loss produces electron hole-pairs and trapping centers (Kanjilal, 2001; Levalois, Bogdanski, & Toulemonde, 1992; Clayes & Simoen, 2002).

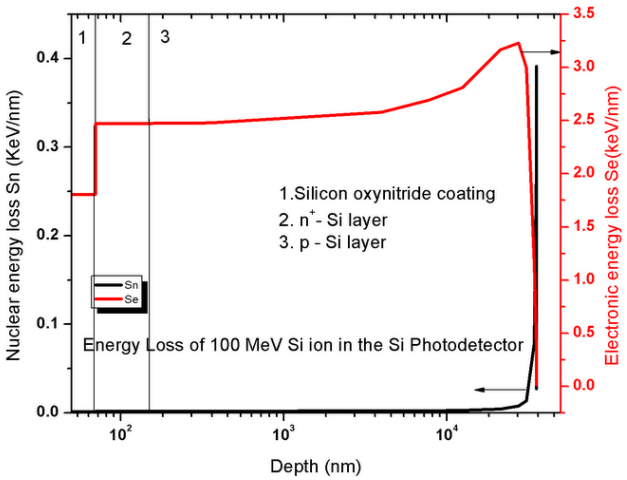

Figure 3. Passage of 100 MeV Si ion along different layers of the Si photo detector

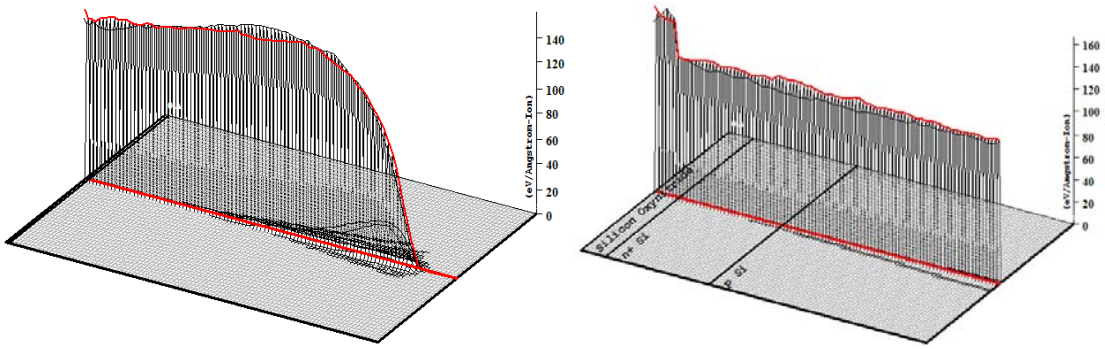

a b

Figure 4. (a) Ionization damage (eV/Angstrom-ion) in 100 MeV Si ion irradiated Si photo detector (upto range of ion: 35.4 μm from the top surface) and (b) Ionization damage (eV/Angstrom-ion) in 100 MeV Si ion irradiated Si photo detector (upto 1 μm depth from the top surface)

The ionization and displacement damage induced by 100 MeV Si ion beam in the present device structure is shown in Figure 4a, 4b and Figure 5a, 5b respectively. It is clear from Figure 4a and 4b that the ionization damage is maximum at the beginning of the ion range and it gradually decreases along with the depth. Whereas Figure 5a and 5b shows that the displacement damage is minimum in the beginning and it is maximum at the end of the range. Therefore more number of displacements/vacancies are created due to large nuclear energy loss in the bulk Si and electron-hole pairs are created due to ionization damage mostly in AR coating region, n^+ layer and in the bulk of Si. The same has been validated by further calculations of NIEL and TID.

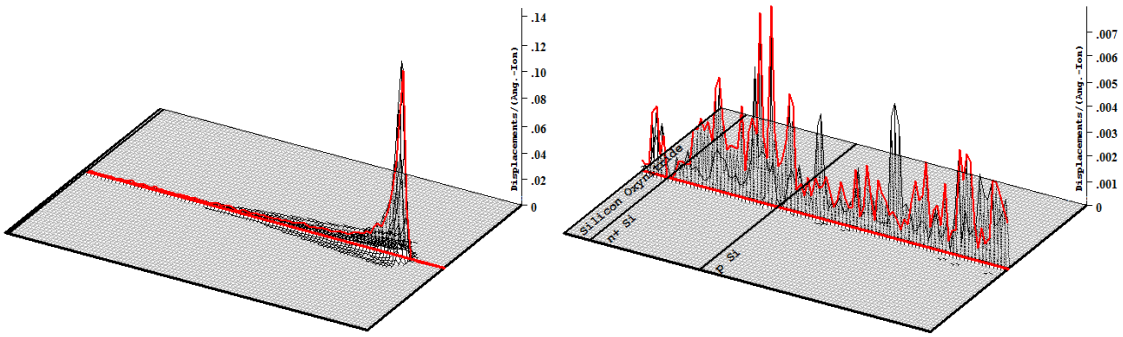

a b

Figure 5. (a) Displacement damage (Displacements/Angstrom-ion) in 100 MeV Si ion irradiated Si photo detector (up to range of ion: 35.4 µm from the top surface) and (b) Displacement damage (Displacements/Angstrom-ion) in 100 MeV Si ion irradiated Si photo detector (up to 1 µm depth from the top surface)

3.2 Contributions From NIEL and LET

TRIM is a comprehensive program of SRIM which provides the detailed treatment of ion damage cascades and the ion distribution within the target material. Only primary displacements due to ion cascade are considered and the quantitative estimation of the damage on the layered structure of the device is provided. The amount of charge in the ionization track per unit length is called the linear energy transfer (LET) and is measured in MeV-cm^2/g. LET is a function of particle type and incident energy (Pease, Johnston, & Azarewicz, 1988). The expression for NIEL (Messenger, Burke, Summers, & Xapsos, 1999) is given by,

$$NIEL = \frac{N}{A}\int_{\theta_{min}}^{\pi}\left[\frac{d\sigma(\theta,E)}{d\Omega}\right]T(\theta,E).L(\theta,E).d\Omega \quad (1)$$

Where N is the Avogadro's number, A is the atomic number and θ_{min} is the minimum scattering angle for which the recoil energy equals the threshold energy for the atomic displacements, T is the average recoil energy for the target atoms and L is the Linhard partition function which separates the energy into ionizing and non-ionizing events. NIEL is a direct analog of LET and it is usually expressed in MeV-cm^2/g. The value of NIEL is estimated from SRIM and was found to be 64.415 MeV-cm^2/g.

The TID and D_d is calculated using the relation,

$$\text{TID} = 1.6 \times 10^{-8} \times \Phi \times \text{LET} \quad (2)$$

$$D_d = 1.6 \times 10^{-8} \times \Phi \times \text{NIEL} \quad (3)$$

Where 1.6×10^{-8} is the unit conversion parameter and the unit is rad g/MeV, Φ is the ion fluence (ions/cm^2).

The damage caused due to LET and NIEL is estimated from SRIM/TRIM and tabulated in Table 1. The fluence dependent TID and D_d are tabulated in Table 2. TID is mainly dependent on the value of LET and hence in case of MeV ion, the contribution from electronic excitations is much more compared to nuclear displacements by 3 orders of magnitude.

Table 1. TRIM Calculations for 100 MeV Si in Si target

Name	Value
Range, R (μm)	35.4
Average Displacements/ion	9707
Average Vacancies/ion	8951
Average Replacements/ion	756
NIEL up to R (MeV cm^2/g)	64.415
LET ((MeV cm^2/g)	10.072 x 10^3

Table 2.Fluence dependent TID and D_d for Si target

Fluence (ions/cm^2)	$1x10^{11}$	$5x10^{10}$	$1x10^{11}$	$5x10^{11}$	$1x10^{12}$	$5x10^{12}$	$1x10^{13}$
TID(rad)	1.611 $x10^6$	8.057 $x10^6$	1.611 $x10^7$	8.057$x10^7$	1.611$x10^8$	8.057 $x10^8$	1.611 $x10^9$
D_d (rad)	1.026$x10^4$	5.132 $x10^4$	10.26 $x10^4$	51.32 $x10^4$	10.26 $x10^5$	51.32 $x10^5$	10.26 $x10^6$

3.3 I-V Measurements / Current Transport Mechanism

The I-V characteristics (in dark condition) of 100 MeV Si^{7+} ion irradiated Silicon photo detector in the fluence range of 1×10^{10} to 1×10^{13} ions/cm^2 is shown in comparison with pristine results in Figure 6a and 6b. The reverse I-V characteristics exhibits a drastic change compared to forward bias.

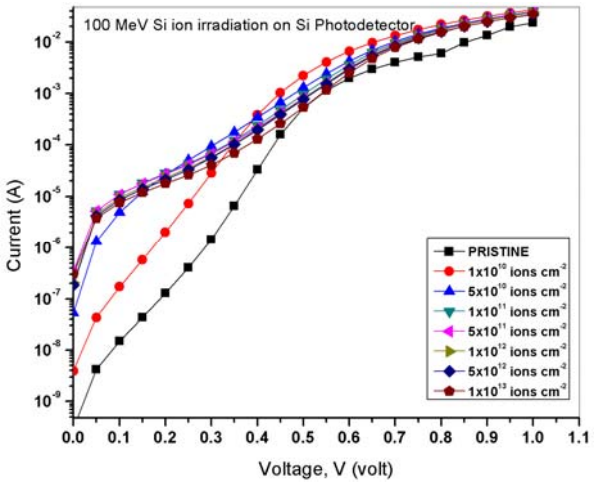

Figure 6a. Forward bias I-V characteristics of 100 MeV Si ion irradiated Si Photo detector

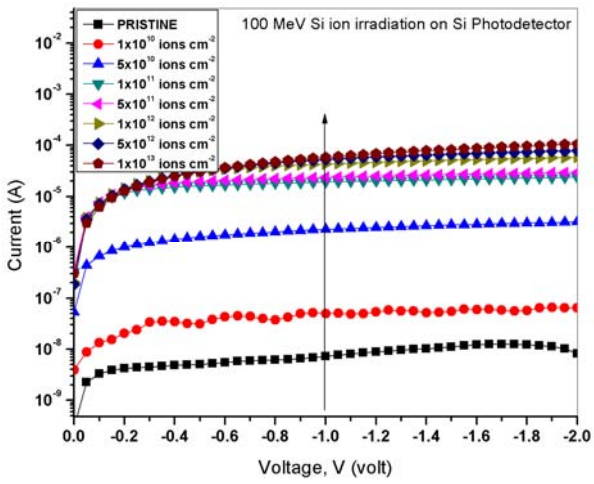

Figure 6b. Reverse bias I-V characteristics of 100 MeV Si ion irradiated Si Photo detector

To study the modification in current transport properties of the device due to Si ion irradiation, the I-V characteristics has been analyzed according to thermionic emission theory and the experimental data is fitted with thermionic emission given by (Jayavel, Udayashankar, Kumar, Asokan, & Kanjilal, 1999),

$$I = I_s\left[\exp\left(\frac{qV}{nk_BT}\right) - 1\right] \quad (4)$$

Where,

$$I_s = A^{**}T^2\exp\left(\frac{-q\phi_B}{k_BT}\right) \quad (5)$$

Where A^{**} is the effective Richardson constant (A cm^{-2} K^{-2}); T is the absolute temperature (K), I_s is the saturation current and n is the ideality factor and other symbols have their usual significance. From the gradient of ln(I) versus V curve, the value of ideality factor is estimated using the relation,

$$n = \frac{q}{k_B T}\left[\frac{dV}{d(\ln I)}\right] \quad (6)$$

One of the important parameters of the device is series resistance and it was been calculated by using the method developed by Cheung and Cheung (Cheung & Cheung, 1986). The forward bias I-V characteristics due to thermionic emission of hetero-structures with series resistance can be expressed as Cheung functions,

$$\frac{dV}{d(\ln I)} = IR_s + n\left[\frac{kT}{q}\right] \quad (7)$$

The term IR_S is the voltage drop across the junction. The gradient of dV/d(lnI) yields the series resistance (R_S). Also reverse leakage current (I_R) at -1V has been determined from Figure 6b. All the evaluated parameters are tabulated in Table 3.

Table 3. The calculated device parameters for different ion fluences

Sl. No	Ion Fluence (ions cm^{-2})	Ideality factor (n)	Series Resistance (R_s) (ohm)	Reverse Leakage current I_R (A) (at -1 V)
1	Pristine	1.48	8.205	7.23×10^{-9}
2	1×10^{10}	1.62	8.615	4.97×10^{-8}
3	5×10^{10}	2.71	8.880	2.28×10^{-6}
4	1×10^{11}	3.40	9.022	1.19×10^{-5}
5	5×10^{11}	3.51	8.720	2.37×10^{-5}
6	1×10^{12}	3.41	8.680	4.35×10^{-5}
7	5×10^{12}	3.37	8.330	5.31×10^{-5}
8	1×10^{13}	3.34	7.960	5.38×10^{-5}

The value of ideality factor for pristine sample and at different fluences are tabulated in Table 3. The 100 MeV Si^{7+} ion irradiation increases the value of ideality factor moderately up to 3.51 for the fluence of 5×10^{11} ions/cm^2. It can be observed from the values of ideality factor that the ideality factor increases up to a fluence of 5×10^{11} ions/cm^2. Further the ideality factor decreases slightly with increasing ion fluence. Since the value of ideality factor lies between 1 and 2 at the initial stages the conduction mechanism is due to thermionic emission and gradually there is a contribution from generation recombination process.The generation-recombination process lead the diode to deviate from its ideal behaviour (Sharma, Shahnawaz, Kumar, Katharria, & Kanjilal, 2007). Therefore the increase in ideality factor clearly indicates that the Si ion beam induced modification in current transport mechanisms. At higher fluences magnitude of ideality factor increases by 2-3 orders and saturates around 3.4 indicating probable contribution from defect assisted tunnelling current. The activation of multiple current transport mechanisms may be attributed to the observed increase in the value of ideality factor. It is evident from the fluence dependent NIEL and TID calculations that the number of defects created by ion beam also increases along with the fluence. After the fluence of 5×10^{11} ions/cm^2 the accumulation of these defects get saturated and is reflected in the saturation value of ideality factor. The enhanced recombination probability of trap centers introduced by Si ion beam in the intrinsic region of the device may also have significant contribution for the increase in the value of ideality factor (Pillai et al., 2012).

Since the reverse leakage current of advanced silicon photo diodes used in nuclear radiation detection is very low, measurement of changes in the leakage current can be a very sensitive tool for monitoring ion irradiation (Hazdra, Haslar, & Vobecky, 1995). In the present study, the value of I_R has increased significantly. It is to be noted that pristine sample has the reverse leakage current of 7.23 nA at -1V and it has drastically increased up to 11.9 μA for the fluence of 1×10^{11} ions/cm^2, thereafter begins to saturate around 10^{-5} A. It is to be noted that I_R has increased up to four orders of magnitude when compared to pristine value. The Si ion beam induced increment in dark leakage current occurs due to the creation of trap centers which act as recombination centers in the band gap of semiconductor. These trap centers are created due to atomic displacement which leads to increase in thermal generation rate in the depletion region of the device. The increase of reverse leakage current

with the fluence confirms the increase of generation-recombination (G-R) centers (Khamari et al., 2011). The value of series resistance of the device in the present investigation increases initially up to 1×10^{11} ions/cm^2 and slightly decreases at higher fluences. Series resistance is inversely proportional to the product of both mobility and carrier concentration. In general ion irradiation is known to decrease the carrier mobility and carrier concentration and thereby increase the series resistance. The 100 MeV Si beam has introduced significant number of displacements, vacancies as listed in Table 2. These defects contribute to the decrease in minority carrier lifetime and responsible for increase in the value of series resistance. As the low temperature mobility is affected by the presence of shallow levels, the mobility might not change at lower fluence, however at higher fluence the less stable shallow level may become stable and form complex defects contributing to increase in mobility (Khamari et al., 2011). At the lower fluences the series resistance increases because of the increase in number of vacancies created by the ion beam. But at higher fluences these defects get saturated and starts overlapping. The decrease in series resistance implies that the product of mobility and free career concentration has been increased. It is reported that the increase in mobility decreases the value of series resistance (Kumar, Katharria, Batra, & Kanjilal, 2007). After a certain fluence there is a dynamic equilibrium between creation and annealing of defects. The defect creation is mainly due to atomic displacements during elastic (S_n) collisions of ion with Si atoms, where as annealing of defects is due to inelastic (S_e) collisions causing excitation and ionization of atoms and their subsequent relaxation (Verma, Praveen, Kumar, & Kanjilal, 2013). The high value of electronic energy loss is known to produce partial annealing (Srour et al., 2003; Singh, Arora, & Kanjilal, 2001). At higher fluences, the device parameter starts saturating, as there will not be any effective increase in defects.

It is necessary to estimate the radiation hardness of the Si photo detector when the devices are considered for space application. Here we have followed the approach of Sciuto et al. (Sciuto, Roccaforte, & Raineri, 2008). The estimation of proton irradiation induced damage on the present device was deduced from the 100 MeV Si ion beam irradiation effects by taking into account of the nuclear stopping power (Ziegler et al., 2010; Sze, 1988). Considering the typical proton fluxes in the range of 10^2 to 10^4 ions/cm^2/s, from SRIM simulation it can be estimated that irradiation with 100 MeV Si ion beam with the fluence of 10^{11} ions/cm^2 would be equivalent to irradiation with 1.6 MeV protons for a time longer than 35 years (NASA (www.nasa.gov), Messenger & Ash, 1986). Thus in Low earth orbit, usually where the spacecrafts and satellites are operated, the detector will require very long time to achieve fluence of 10^{11} ions/cm^2 and hence it can function reliably during its operational lifetime.

4. Conclusion

Si $n^+/p/p^+$ junction photo detector has been subjected to 100 MeV Si ion irradiation at various fluences and its sensitivity for ionization and displacement damage has been systematically studied. In-situ darkI-V measurements has been performed and the present device shows increase in the value of ideality factor and reverse leakage current upto the fluence of 5×10^{11} ions/cm^2, thereafter it is almost constant indicating good radiation immunity. Si ion beam induced G-R centers in the bulk Si may be the main reason for the increase in leakage current. The higher values of ideality factor are attributed to activation of multiple transport mechanisms including multistep tunnelling. However the NIEL induced displacement damage appears to be the major effect to the observed degradation primarily in the bulk region of the device. At higher fluences these parameters improve indicating the annealing effect due to high electronic energy loss. SRIM results also validate that the displacement damage is created in the bulk Si compared to top layers of the device. The values of LET and NIEL and fluence dependent TID and D_d has been calculated and an attempt has been made to correlate with the observed degradation in electrical parameters. Radiation hardness is estimated by comparing the present study with the equivalent damage created by proton and the present device was found to function reliably for several tens of years in low earth orbit.

Acknowledgments

One of the Authors (MVK) thanks IUAC for providing financial assistance through fellowship Grant no. UFR-50310. The technical assistance provided by Pelletron group at IUAC during the beam time experiment is acknowledged. Also, the authors thank Dr. C. L. Nagendra (LEOS-ISRO, Bangalore), Dr. C. M. Dinesh (Govt. first grade college, Kolar, India) and Dr. Prabha Sana (MANIT, Bhopal) for their useful discussions.

References

Bolse, W., & Schattat, B. (2002). Atomic mixing in thin film systems by swift heavy ions. *Nucl. Instr. and Meth. B, 190*(1-4), 173-176. http://dx.doi.org/10.1016/S0168-583X(01)01225-3

Bourqui, M. L., Bechou, L., Gilard, O., Deshayes Y., Del Vecchio P., How L. S., … Touboul, A. (2008). Reliability investigations of 850 nm silicon photodiodes under proton irradiation for space applications. *Microelectron. Reliab, 48*, 1202-1207. http://dx.doi.org/10.1016/j.microrel.2008.07.012

Cheung, S. K., & Cheung, N. W. (1986). Extraction of Schottky diode parameters from forward current - voltage characteristics. *Appl. Phys. Lett., 49*, 85 -87. http://dx.doi.org/10.1063/1.97359

Clayes, C., & Simoen, E. (2002). *Radiation Effects in Advanced Semiconductor Materials and Devices*. Heidelberg, Germany: Springer-Verlag, ch. 2.

Gill, K., Hall G., & MacEvoy, B. (1997). Bulk damage effects in irradiated silicon detectors due to clustered divacancies. *J. Appl. Phys., 82*, 126-136. http://dx.doi.org/10.1063/1.365790

Hazdra, P., Haslar, V., & Vobecky, J. (1995). Application of defect related generation current for low-dose ion implantation monitoring. *Nucl. Inst. Meth. B,* 96, 104-108. http://dx.doi.org/10.1016/0168-583X(94)00462-5

Jayavel, P., Udhayasankar, M., Kumar, J., Asokan, K., & Kanjilal, D. (1999). Electrical characterisation of high energy ^{12}C irradiated Au/n-GaAsSchottky Barrier Diodes. *Nucl. Inst. Meth. B, 156*(1-4), 110-115. http://dx.doi.org/10.1016/S0168-583X(99)00282-7

Kanjilal, D. (2001). Swift heavy ion induced modification and track formation in materials. *Curr. Sci. India, 80*(12), 1560-1566. http://www.iisc.ernet.in/~currsci/jun252001/1560.pdf

Khamari, S. K., Dixit, V. K., Ganguli, T., Porwal, S., Singh, S. D., Kher, S., … Oak, S. M. (2011). Effect of ^{60}Co γ-ray irradiation on electrical properties of GaAsepilayer and GaAs p–i–n diode. *Nucl. Inst. B., 269*(3), 272-276. http://dx.doi.org/10.1016/j.nimb.2010.11.067

Krishnan, S., Sanjeev, G., & Pattabi, M. (2007). 8 MeV electron irradiation effects in silicon photo-detectors. 8 MeV electron irradiation effects in silicon photo-detectors.*Nucl.Inst. Meth. B, 264*, 79-82 http://dx.doi.org/10.1016/j.nimb.2007.08.004

Kumar, S., Katharria, Y. S., Batra, Y., & Kanjilal, D. (2007). Influence of swift heavy ion irradiation on electrical characteristics of Au/ n -Si (1 0 0) Schottky barrier structure. *J. Phys. D. Appl. Phys., 40*(22), 6892-6897. http://dx.doi.org/10.1088/0022-3727/40/22/006

Kurokawa, M., Motobayashi, T., Ieki, K., Shimoura, S., Murakini, H., Ikeda, Y., Moriya, S., Yanagisawa, Y., & Nomura, T. (1995). Radiation damage factor for ion-implanted silicon detectors irradiated with heavy ions. *IEEE Trans. Nucl. Sci., 42*(3), 163-166. http://dx.doi.org/10.1109/23.387356

Leroy, C., & Rancoita, P. G. (2009). Principles of radiation interaction in matter and detection. *World Scientific Publishing Company Incorporated.*

Levalois, M., & Marie, P. (1999). Damage induced in semiconductors by swift heavy ion irradiation. *Nucl. Instr. and Meth. B, 156*(1-4), 64-71. http://dx.doi.org/10.1016/S0168-583X(99)00243-8

Levalois, M., Bogdanski, P., & Toulemonde, M. (1992).Induced damage by high energy heavy ion irradiation at the GANIL accelerator in semiconductor materials. *Nucl. Inst. Meth. B, 63*(1-2), 14-20. http://dx.doi.org/ 10.1016/0168-583X(92)95160-S

Messenger, G., & Ash, M. (1986). The Effects of Radiation on Electronic Systems. *Van Nostrand Reinhold,* 245.

Messenger, S. R., Burke, E. A., Summers, G. P., Xapsos, M. A., Walters, R. J., Jackson, E. M., & Weaver, B. D. (1999). Nonionizing energy loss (NIEL) for heavy ions. *IEEE Trans. Nucl. Sci., 46*(6), 1595-1602. http://dx.doi.org/10.1109/23.819126

Moloi S. J., & McPherson, M. (2009). The current and capacitance response of radiation-damaged silicon PIN diodes.*Physica B, 404*(21), 3922-3929. http://dx.doi.org/10.1016/j.physb.2009.07.123

NASA website. (ND). http://ww.nasa.gov

Pastuovic, Z., Jaksic, M., Kalinka, G., Novak, M., & Simon, A. (2009). Deterioration of electrical and spectroscopic properties of a detector grade silicon photodiode exposed to short range proton, lithium and oxygen ion irradiation. *Nuclear Science, IEEE Transactions on, 56*(4), 2457-2464. http://dx.doi.org/10.1109 /TNS.2009.2023123

Pease, R. L., Johnston A. H., & Azarewicz, J. L. (1988).Azarewicz.Radiation testing of semiconductor devices for space electronics *IEEE proceedings, 76*(11), 1510-1526. http://dx.doi.org/10.1109/5.90110

Pillai, V. R. V, Khamari, S. K., Dixit, V. K., Ganguli, T., Kher, S., & Oak, S. M. (2012). Effect of γ-ray irradiation on breakdown voltage, ideality factor, dark current and series resistance of GaAs*p–i–n* diode. *Nucl. Inst. Meth. A, 685*, 41-45. http://dx.doi.org/10.1016/j.nima.2012.05.062

Prabhakara Rao, Y. P., Praveen, K. C., Rejeena Rani, Y., Tripathi, A., & Gnana Prakash, A. P. (2013). 75 MeV boron ion irradiation studies on Si PIN photodiodes. *Nucl. Instr. Meth. B, 316*, 205-209. http://dx.doi.org/10.1016/j.nimb.2013.09.011

Sciuto, A., Roccaforte, F., & Raineri, V. (2008). Electro-optical response of ion-irradiated 4H-SiC Schottky ultraviolet photo detectors. *Appl. Phys. Lett., 92*(093505), 1-3. http://dx.doi.org/10.1063/1.2891048

Sharma, A. T., Shahnawaz, K. S., Katharria, Y. S., & Kanjilal, D. (2007). Effect of swift heavy ion irradiation on electrical characteristics of Au/n-GaAsschottky diodes. *Appl. Surf. Sci., 254*(2), 459-463. http://dx.doi.org/10.1016/j.apsusc.2007.06.027

Singh, R., Arora, S. K., & Kanjilal, D. (2001). Swift heavy ion irradiation induced modification of electrical characteristics of Au/n-Si Schottky barrier diode. *Mat. Sci. Semicon. Proc., 4*, 425-432. http://dx.doi.org/10.1016/S1369-8001(01)00009-9

Srour, J. R., Marshall, C. J., & Marshall, P. W. (2003). Review of displacement damage effects in silicon devices. *IEEE Trans. Nucl. Sci., 50*, 653-670. http://dx.doi.org/10.1109/TNS.2003.813197

Sze, S. M. (1988). *VLSI Technology* (McGraw-Hill International Editions). NewYork, 1988.

Verma, S., Praveen, K. C., Kumar, T., & Kanjilal, D. (2013). In Situ Investigation of Current Transport Across Pt/n-Si (100) Schottky Junction During 100 Ni^{7+} Ion Irradiation. *IEEE Trans. Device Mater. Rel., 13*(1), 98-102. http://dx.doi.org/10.1109/TDMR.2012.2217396

Ziegler, J. F., Ziegler, M. D., &Biersack, J. P. (2010). SRIM–The stopping and range of ions in matter (2010). *Nuclear Instruments and Methods in Physics Research Section B: Beam Interactions with Materials and Atoms, 268*(11), 1818-1823. http://dx.doi.org/10.1016/j.nimb.2010.02.091

Journal of Materials Science Research; Vol. 3, No. 3; 2014
ISSN 1927-0585 E-ISSN 1927-0593
Published by Canadian Center of Science and Education

A Fiber-Reinforced Architectural Concrete for the Newly Designed Façade of the Poseidon Building in Frankfurt am Main

Henrik L. Funke[1], Sandra Gelbrich[1], Andreas Ehrlich[1] & Lothar Kroll[1]

[1] Institute of Lightweight Structures, Technische Universität Chemnitz, Chemnitz, Germany

Correspondence: Henrik L. Funke, Institute of Lightweight Structures, Chemnitz University of Technology, Chemnitz, Germany. Tel: 49-371-5313-8995. E-mail: henrik.funke@mb.tu-chemnitz.de

Received: March 12, 2014 Accepted: April 10, 2014 Online Published: June 27, 2014

doi:10.5539/jmsr.v3n3p33 URL: http://dx.doi.org/10.5539/jmsr.v3n3p33

Abstract

In the course of revitalizing the Poseidon Building in Frankfurt, an energetically optimized façade, made of architectural concrete was developed. The development of a fiber-reinforced architectural concrete had to consider the necessary mechanical strength, design technology and surface quality. The fiber-reinforced architectural concrete has a compressive strength of 104.1 MPa and a 3-point bending tensile strength of 19.5 MPa. Beyond that, it was ensured that the fiber-reinforced high-performance concrete had a high durability, which has been shown by the capillary suction of de-icing solution and freeze thaw test with a weathering of abrasion of 113 g/m² after 28 freeze-thaw cycles and a mean water penetration depth of 11 mm.

Keywords: fiber-reinforced concrete, durability, CDF-Test, high-performance concrete

1. Introduction

Apart from designing claddings, the focus in civil engineering increasingly moves to sustainability and resource efficiency, because future-oriented living and building is hardly viable without a significant increase of resource efficiency. With respect to resource efficiency, optimized building with low input (material, energy, area) during the complete lifecycle of a building means to meet the requirements of the residents regarding indoor environment quality and home comforts.

A truly sustainable building has to meet individual design requirements. It is to be built in the desired location within a very short time and with little effort. It also has to be possible to rebuild and remove the building easily at a future date (Lemken, 2008). Using the material and technologies that are currently available, the practical implementation of these innovative ideas is rather expensive and therefore reaches its limits easily. The application of new high-performance materials which are inorganic-non-metallic offers more freedom for construction. Fiber-reinforced concrete facilitates the production of thin-walled, single- and double-curved free-form elements which are highly suitable for lightweight construction and comply with design requirements regarding surface quality (Brameshuber, 2006; Funke et al., 2013a, Mumenya, 2012; Rafi et al., 2006; Funke et al., 2013b; Schneider et al., 2004).

The Poseidon Building, a multistory building in Frankfurt which was built in the 1970s and 1980s, is an example for construction in existing contexts. In 2008, the Poseidon Building was planned to be replaced by a newly built skyscraper (Wirtschaft & Architektur, 2013), but a revitalization was preferred instead by reason of resource efficiency and sustainability. In the course of revitalization, an energetically optimized façade was going to be implemented to get the Green Building “Gold” certification after LEED (Leadership in Energy and Environmental Design).

The 13800 m² three-dimensional façade consists of more than 11500 elements. Of special importance in the course of redesigning the façade was the replacement of the aluminum elements with high-strength architectural concrete. That architectural concrete was to be pure white, with perfect surface quality. This means, it had to have a homogeneous coloring and be absolutely non-porous.

This paper reports the devolpment of the architectural concrete and an appropriate process technology for the production of prefabricated façade elements. An important part of this work is the testing of long-term behaviour and durability aspects of the fiber-reinforced architectural concrete.

2. Method

2.1 Components of Architectural Concrete

The composition of the used concrete was dependent on the requirements it had to meet respecting statics, color, surface quality and element design. Based on these requirements, the fine concrete in Table 1 was developed. Except from white Portland cement CEM I 52.5 N (according to EN 197) it contained amorphous aluminosilicate as pozzolan. Dolomite sand with a grain size of 0 to 1 mm and dolomite powder with an average grain size of 70 µm were used as aggregate and filler. The short alkali-resistant (AR) glass-fibers (16 mass percent of ZrO_2) was 12 mm long and had a length weight of 45 g/km. A super plasticizer based on polycarboxylate ether (PCE) was used with a solid content of 30 mass percent. The water binder ratio was 0.35.

Table 1. Qualitative composition of the architectural concrete

component	explanation
white cement CEM I 52.5 N	• white cement with high early strength
amorphous aluminosilicate	• pozzolan to increase mechanical strength and durability, and as optical brightener
dolomite sand 0/1	• white aggregate
dolomite powder (x_{50} = 70 µm)	• filler to improve processability of fresh concrete and as white pigment
integral AR-glass fibers (12 mm)	• armoring for the fine-aggregate concrete matrix
water	• for mixing the concrete
high-performance plasticizer (30 M.-% PCE)	• electrosteric stabilizer

The fine grained concrete was mixed with the intensive mixer Eirich R05T. The mixing parameters are shown in Table 2. The mixing time was 5 min in total. The fresh concrete was tested according to DIN EN 12350. Air content and bulk density of the fresh concrete were determined by means of an air content testing device, following DIN 18555-2.

Table 2. Mixing parameters for the production of fine concrete

	component	mixing principle	mixing power in %	mixing time in s
1.	binders + aggregates	counter rotation	15	60
2.	75 % of water	co-rotation	50	90
3.	super plasticizer	co-rotation	50	60
4.	residual water	co-rotation	50	30
5.	ar-glass fibres	co-rotation	60	60

2.2 Rheological Optimization by Superplasticizer Content

The optimization of the superplasticizer content was carried out by rheological measurements of the fresh concrete of Table 2. For this, flow curves of the fresh concrete were measured with various superplasticizers content using the rheometer Thermo Scientific HAAKE MARS III (Figure 1). The measurements were carried out with the so-called material box. As a comparing measurement variable, the torque was used at a shear rate of 10 s^{-1} in response to the superplasticizer content.

Figure 1. Rheometer HAAKE MARS for rheological measurements (Origin: Thermo Scientific)

2.3 Determination of the Hardened Concrete Characteristics

The samples for the tests to be performed on the hardened concrete were stored dry, according to DIN EN 12390-2. The compressive strength was determined by means of the Toni Technik ToniNorm (load frame 3000 kN) following DIN EN 12390-3, with cubes having an edge length of 150 mm (Figure 2a). The pre-load was 18 kN. The span width set was 200 mm and the load speed 100 N/s constant.

The 3-point bending tensile strength (Figure 2b) was determined with samples which measured 225 x 50 x 15 mm^3 (length x width x height), based on DIN EN 12390-5 and ToniNorm (test frame 20 kN).

Figure 2. Determination of compressive strength and 3-point bending tensile strength

To validate the durability of the architectural concrete, the capillary suction of de-icing solution and freeze thaw test (CDF-test) was measured by the Schleibinger Freeze-Thaw-Tester (Figure 3) with standard agent solution according to the recommendations of RILEM TC 117-FDC. Beyond this, the water penetration depth was determined.

Figure 3. Determination of the capillary suction of de-icing solution and freeze thaw test

3. Results

3.1 Optimization of Superplasticizer Content

Figure 4 shows the torque as a function of the superplasticizer content at a shear rate of $10s^{-1}$. The torque decreases up to a superplasticizer content of 3.5 mass percent due to the increasing electrosteric stabilization of finely dispersed particles, such as cement particles and silica fume. The point of saturation S_P, i.e. the complete stabilization of the finely dispersed particles, is about 3.5 mass percent of the superplasticizer content. Over the saturation point (> 3.5 mass percent) added superplasticizer contents results in an increasing torque. The increasing of the torque, and thus indirectly increases the dynamic viscosity, is due to the viscosity of the plasticizer itself. Beyond this, the increased entanglement of the steric PCE main and side chains results in an increasing of the torque.

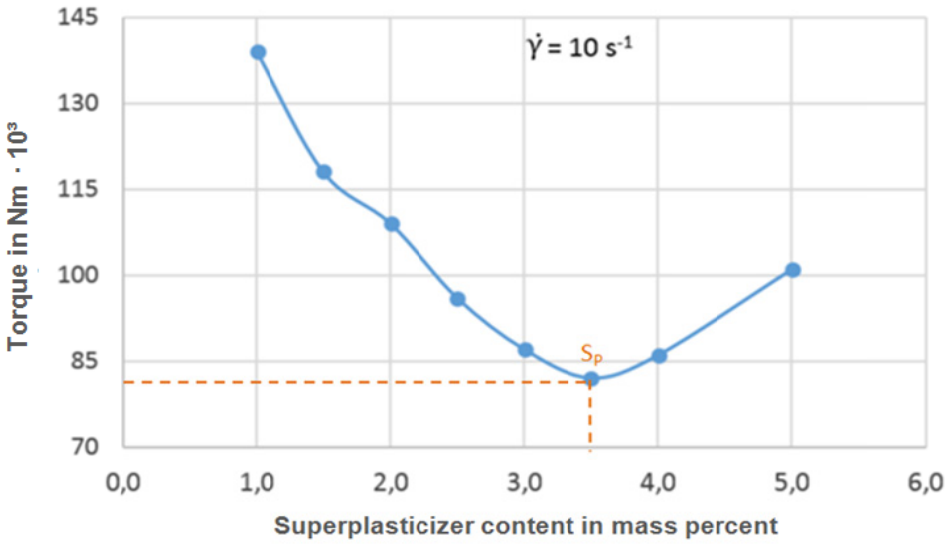

Figure 4. Torque as a function of superplasticizer content

3.2 Fresh and Hardened Concrete Characteristics

Table 3 shows the fresh and hardened concrete characteristics after 28 days. With a high flow capacity (diameter of the resulting flow table test: 650 mm) the fresh concrete complies with the flow class F6. The air content tester showed an air volume content of 2.0% and a geometric bulk density of 2.28 g/cm³ in the fresh concrete. The total shrinkage deformation, determined with a shrinkage channel, was 0.91 mm/m. The reasons for this were first the high binder content, and the high chemical shrinkage resulting from that. Second, autogenously shrinkage increased due to the low water-binder ratio. Drying shrinkage could be practically eliminated due to a two days aftertreatment including humidifying and protection against draft. The high total shrinkage deformation did not lead to shrinkage cracking and was therefore not harmful.

The compressive strength was 104.1 MPa after 28 days and already 38 MPa after 24 hours. Thus, the façade elements were ready to be demolded after one day. The small variation coefficient of 1.1% implied a homogenous microstructure of the hardened concrete. The 3-point bending tensile strength was 19.5 MPa, so the static requirements were met.

Table 3. Fresh and hardened concrete characteristics of fiberglass-modified fine concrete after 28 days

characteristic	fresh concrete	hardened concrete
geometric bulk density	2.28 g/cm³	2.21 g/cm³
flow spread	650 mm	-
air content	2.0 Vol.-%	-
linear shrinkage	0.91 mm/m	
compressive strength	-	104.1 MPa
3-point bending tensile strength	-	19.5 MPa

3.3 Durability and Recyclability

The results of the durability tests are listed in Table 4. The developed architectural concrete displays a high durability, which was validated in the CDF test (m_{28} = 113 g/m² and $R_{u,28}$ = 100%) after 28 freeze-thaw cycles and a water penetration depth of 11 mm. Thus, the architectural concrete meets the requirements respecting building regulations and usability over a long period.

Table 4. Examinations of the durability of architectural concrete

test method	*test value*
CDF test	m_{28} = 113 g/m²
	$R_{u,28}$ = 100%
water penetration depth	11 mm

Due to its composition, the architectural concrete is completely recyclable and can be used as aggregate or admixture in the production of fresh concrete. Not using a steel reinforcement facilitates and shortens recycling, including shredding, cleaning and classifying. This ensures that the quality of the recycled concrete is comparable to that of the original concrete.

3.4 Constructional Implementation

Fifty out of the 11500 façade elements were produced per day. The concrete elements were fixed to pedestals to ensure their safe transport to the building site, where they were mounted (Figure. 5).

Figure 5. Mounted façade elements on the multistory building “Leo”

4. Conclusions

This practical research work was concerned with an applicable method to develop fiber-reinforced architectural concrete for the redevelopment of the façade of the Poseidon Building, in the course of its revitalization. It was demonstrated that the developed fiber-reinforced architectural concrete combines high strength with high surface quality, durability and recyclability.

In building construction that requires lightweight construction, the increasing use of innovative high-performance materials which are fiber-reinforced and inorganic-non-metallic facilitates the production of thin-walled, single- and double-curved free-form surfaces. This entails a larger design potential for architects and planners, especially with regard to organically formed buildings.

Acknowledgements

The successful implementation of the Poseidon project was possible thanks to the close and always constructive collaboration between Fiber-Tech and Hentschke-Bau. An individual authorization could be gotten thanks to the examination of the façade system by the Steinbeis Innovation Center FiberCrete in Chemnitz.

References

Lemken, T. (2008). *Alte Orte, neuer Glanz – ressourceneffizientes Bauen und Wohnen im Bestand*. Wuppertal Institut für Klima, Energie GmbH.

Brameshuber, W. (2006). *Textile Reinforced Concrete, RILEM Report 36*. State-of-the-Art Report of RILEM Technical Committee, TC 201-TRC.

Funke, H., Gelbrich, S., & Kroll, L. (2013a). A New Hybrid Material of Textile Reinforced Concrete and Glass Fibre Reinforced Plastic. *Journal of Materials Science Research, 2*(3).

Mumenya, S. W., Tait, R. B., & Alexander, M. G. (2010). Mechanical behaviour of Textile Concrete under accelerated ageing conditions. *Cement and Concrete Composites, 32*(8), 580-588. http://dx.doi.org/10.1016/j.cemconcomp.2010.07.007

Funke, H., Gelbrich, S., & Ehrlich, A. (2013b). Development of a new hybrid material of textile reinforced concrete and glass fibre reinforced plastic. *Procedia Materials Science, 2*, 103-110, Elsevier, USA. http://dx.doi.org/10.1016/j.mspro.2013.02.013

Rafi, M., Nadjai, A., Ali, F., & Talamoa, D. (2006). Aspects of behaviour of CFRP reinforced concrete beams in bending. *Constructions and Building Materials, 22*, 277-285. http://dx.doi.org/10.1016/j.conbuildmat.2006.08.014

Schneider, H., Bergmann, I., & Schätzke, C. (2004). Lightweight concrete structures. *DETAIL,* 844-854.

Wirtschaft & Architektur. (2013). *Rhein-Main, Verlagshaus Prinz-Carl*. Nüziders.

Journal of Materials Science Research; Vol. 3, No. 3; 2014
ISSN 1927-0585 E-ISSN 1927-0593
Published by Canadian Center of Science and Education

Effect of Metal-Plate Connector on Tension Properties of Metal-Plate Connected Dahurian Larch Lumber Joints

Wei Guo[1], Shasha Song[2], Zehui Jiang[2], Ge Wang[2], Zhengjun Sun[2], Xuehua Wang[2], Feng Yang[2], Hong Chen[2], Sheldon Q. Shi[3] & Benhua Fei[2]

[1] China Institute of Building Standard Design & Research

[2] International Center for Bamboo and Rattan, Beijing 100102, China

[3] Mechanical and Energy Engineering Department, University of North Texas, Denton, TX 76203-1277, USA

Correspondence: Sheldon Q. Shi, Mechanical and Energy Engineering, University of North Texas, Denton, TX 76203-1277, USA. E-mail: Sheldon.Shi@unt.edu

Benhua Fei, International Centre for Bamboo and Rattan, No. 8 Futong Dongdajie, Wangjing Area, Chaoyang District, Beijing 100102, China. E-mail: feibenhua@icbr.ac.cn

Received: December 29, 2013 Accepted: January 27, 2014 Online Published: July 13, 2014

doi:10.5539/jmsr.v3n3p40 URL: http://dx.doi.org/10.5539/jmsr.v3n3p40

Abstract

This paper investigated the tensile behavior of metal-plate connected Dahurian larch (*Larix gmelini* (Rupr.) Rupr) lumber joints. Relationships between the ultimate load and metal-plate connector (MPC) length, width, and area were analyzed for AA loading (i.e. load parallel to the grain, MPC length parallel to the load direction) and EA loading (i.e. load parallel to the grain, MPC length orthogonal to the load direction). Failure modes were studies for both AA and AE loading conditions. It was found that the tensile strength of the joint increased as the size of the connector increased. Tooth withdrawals, MPC breakage and wood breakage were all failure modes observed for the AA loading case. However, tooth withdrawal was the only failure mode observed in the EA loading case.

Keywords: MPC joint, ultimate tension load, MPC size, failure mode

1. Introduction

Metal-plate connected lumber joints can be considered as semi-rigid (i.e. neither pinned nor completely rigid). Therefore, the deformations of the joint may have a substantial contribution to the overall deformation of the structure. Many studies (e.g. Gupta & Gebremedhin, 1990; Sasaki & Hayashi, 1982; Lau, 1987; Kent et al., 1997; Riley & Gebremdhim, 1999) analyzed the mechanical properties of semi-rigid joints in the metal-plate connected wood trusses. The average tensile strength of metal-plate connected truss joints fabricated by No.2 Southern pine lumber and 20-gage punched metal plates was found to be 27 kN, and a combination of wood and teeth failure modes was observed.

A variety of failure modes may occur at the connections in a truss system. For example, shear or tension in the steel elements, tooth withdraw, and wood failure. It has been proven that specimens including short metal-plate connectors usually fail under plate yielding while longer plates fail because of tooth withdrawal. An effective way to avoid metal-plate connector tearing and withdrawal ia to increase the contact area between connector and trusses, and keep the plate length longer than width (see, for example, Riley & Gebremedhin, 1999; Lau, 1987; O'Regan et al., 1998).

Dahurian larch is a popular species in the northeast region of China. It is used for wood frame construction because of its high strength, good decay resistance and abundance in resources. The physical and mechanical properties of Chinese larch had been extensively analyzed in terms of bending, compression, tension etc. Chen et al. (2001) tested small specimens (20×20 mm^2 cross section) of clear Chinese larch following the GB1927-1943-91 standard, "Testing methods for physical and mechanical properties of woods": the modulus of rupture (MOR), the modulus of elasticity (MOE) and the ultimate compression strength (UCS) were found to be 139.0-188.7 MPa, 4.5-5.0 GPa, and 42.3-61.1 MPa, respectively. Wang et al. (2009) tested full-size specimens (38×89 mm^2 cross section) of Chinese larch following the GB /T 50329-2002 "Standard for methods testing of timber structure". The MOR, MOE, 5% percentile UCS and ultimate tension strength (UTS) were found to be 62.3 MPa, 13.7 GPa, 26.4-31.4 MPa, and 14.4-22.4 MPa respectively. Currently, no much data is available on the mechanical behavior

of MPC joints for Chinese larch. Gupta (1996) evaluated strength properties of three connections on different materials. It was found that the average ultimate load of MPC joints of Russian dahurian larch (the same family as Chinese larch) was obtained as 37 kN, which was higher than that of southern pine (28 kN) and Douglas-fir (33 kN). Joints always failed in the withdrawal mode. Latterly, Wei et al. (2013) completed tension tests of Chinese larch MPC joints of four types, including AA and EA, and tfound that the ultimate tension load was reduced by 18.9% from AA to EA. Its failure modes were analyzed, and the load-deflection curves by Foschi 3-parameter model were developed.

The present study aims to: (i) determine the strength and failure mode of Dahurian larch MPC joints subjected to tensile loading; (ii) assess the relationship between the connector dimensions and the ultimate axial load of the joint; (iii) analyze the relationship between the joint size and the failure modes. The MPC joints including plate-connectors of various sizes were tested in both the AA and EA loading modes. The ultimate tensile loads, failure modes, and relationship between MPC size and mechanical properties were analyzed separately for each specimen type.

2. Experimental

All lumbers were processed with a local sawmill. The modulus of elasticity (MOE), air density and moisture content (MC) of each specimen were determined before fabricating the joints in according to the procedures described in GB50329-2002, GB/T1933-1991, and GB/T1931-1991 standards. In order to determine the MOE, the wood piece was placed flat-wise between the two supports spaced by 1620 mm, while the distance between loading points was 810 mm. Displacement was measured at the mid span by a linear variable differential transducer (LVDT) and then recorded by a computer. The average MOE, air density and MC determined in these experiments were 13.8 GPa, 650 kg/m^3 and 12%, respectively.

Figure 1. Experimental set up utilized in the tensile tests performed on MPC join

The Gannail-GN20 MPC obtained from a local supplier was used in this study. The plate thickness was 1.0 mm, the tooth length was 9.5 mm, a dn the tooth density was 8/in.^{2}. For the AA loading mode, MPCs with the following dimensions (width×length) were considered: 40×75 mm^2, 50×50 mm^2, 50×75 mm^2, 50×100 mm^2, 50×125 mm^2, 50×150 mm^2, 75×100 mm^2, 75×125 mm^2 and 75×150 mm^2. The MPCs' dimensions considered for the EA loading mode were: 50×50 mm^2, 75×40 mm^2, 75×50 mm^2 and 75×75 mm^2.

In order to minimize the variations in MOE, density and MC of connected pieces, each joint assembly was fabricated from a single piece of lumber cut in two halves then re-jointed by two MPCs applied by a hydraulic press. Three replicates were used in order to obtain statistically significant data.

Tension tests were carried on with a 50 kN universal testing machine at about 1 mm/minute loading speed and the specimens were failed in about 5 minutes. The load was applied by a hydraulic cylinder and load and deformation data were collected by a data acquisition system until failure. Two holes of diameter 20 mm were predrilled across

the specimen width at 100 mm from both ends of the MPC jointed specimen. Two steel bars were inserted into the holes to transfer the tensile load to the specimen. The experimental set-up utilized in the tensile tests is shown in Figure 1.

Table1. Experimental results of the tensile tests performed on MPC joints

Orientation	MPC size（L.×W.）（mm）	Specimen number	Ultimate load (kN)	Failure mode
AA Orientation	40×75	1	10.77	Tooth withdrawal
		2	10.83	Tooth withdrawal
		3	13.85	Tooth withdrawal
	50×50	1	8.41	Tooth withdrawal
		2	6.17	Tooth withdrawal
		3	10.87	Tooth withdrawal
	50×75	1	12.02	Tooth withdrawal
		2	13.93	Tooth withdrawal
		3	14.47	Tooth withdrawal
	50×100	1	17.9	Tooth withdrawal
		2	31.52	Tooth withdrawal
		3	25.95	Tooth withdrawal
	50×125	1	21.33	Broken MPC
		2	17.43	Broken MPC
		3	21.33	Broken MPC
	50×150	1	25.11	Broken MPC
		2	23.41	Broken MPC
		3	-	-
	75×100	1	24.07	Tooth withdrawal
		2	25.58	Tooth withdrawal
		3	31.62	Tooth withdrawal
	75×125	1	33.18	Broken MPC
		2	32.45	Broken wood
		3	11.77	Broken wood
	75×150	1	43.97	Broken wood
		2	38.96	Broken MPC
		3	-	-
EA Orientation	50×50	1	8.05	Tooth withdrawal
		2	7.1	Tooth withdrawal
		3	-	-
	75×40	1	7.4	Tooth withdrawal
		2	9.27	Tooth withdrawal
		3	-	-
	75×50	1	11.47	Tooth withdrawal
		2	12.01	Tooth withdrawal
		3	15.38	Tooth withdrawal
	75×75	1	18.28	Tooth withdrawal
		2	17.32	Tooth withdrawal
		3	25.4	Tooth withdrawal

3. Results and Discussion

3.1 Relationship Between MPC Joint Tensile Strength and Joint Size

Experimental results gathered for the tested MPC joints are shown in Table 1. It can be seen that the ultimate tensile load was in the range of 8.41-43.97 kN for the AA loading mode and 7.4-25.4 kN for the EA loading mode. The tooth withdrawal, plate breakage and wood rupture are the three main failure modes observed for the AA specimens, while only the tooth withdrawal was seen for the EA loading mode.

The dimensions of the metal plate connector greatly affect the mechanical properties of MPC joints, especially the strength and stiffness. The requirements on MPC size given in some standards (TPI 1995, TPI 2002, GB50005-2003) indicate that no failure should occur regardless of the plate width and length. The dimensions of the MPC element should be determined considering the size of lumbers and the joints to be realized. Larger plates allow the fraction of load supported by each tooth to be reduced. However, increasing the length of the plate will increase the costs and material waste, and might not necessarily improve the overall tensile strength of the joint. Triche and Suddarth (1998) found that the bearing capacity of teeth decreased by 39% in spite of tripling the MPC length.

The ultimate tensile load determined for joints with 50 mm and 75 mm wide plates for the AA loading mode are presented in Figures 2 and 3, respectively. The plotted values were averaged from the experimental data reported in Table 1as 8.48, 13.4, 21.97, 20.03 and 24.26 kN, for the 50×50 mm^2, 50×75 mm^2, 50×100 mm^2, 50×125 mm^2 and 50×150 mm^2 plates, respectively. The ultimate tension load always increased with MPC size except for the joint realized with a 50×120 mm^2 plate. A linear relationship was found between the ultimate tension load and the MPC size with a coefficient of correlation R^2 of 0.865.

The average ultimate tensile loads for AA type joints were determined as 27.09 kN, 32.8 kN, and 41.47 kN, for the connectors with sizes of 75×100 mm^2, 75×125 mm^2 and 75×125 mm^2, respectively. A linear relationship between the ultimate tension load and the plate length also presents in Figure 3. A better correlation was obtained compared to the 50 mm wide specimens (R^2: 0.99).

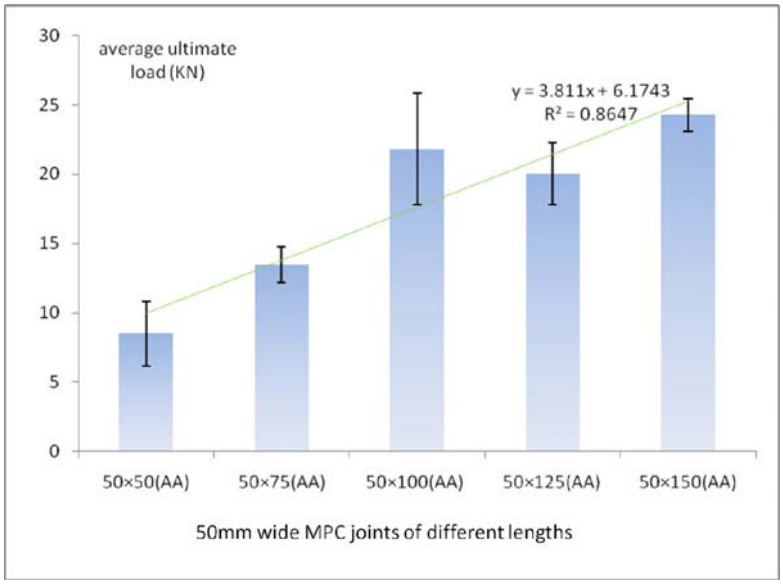

Figure 2. Ultimate tensile loads at different connector lengths for the 50 mm wide specimens loaded in AA mode

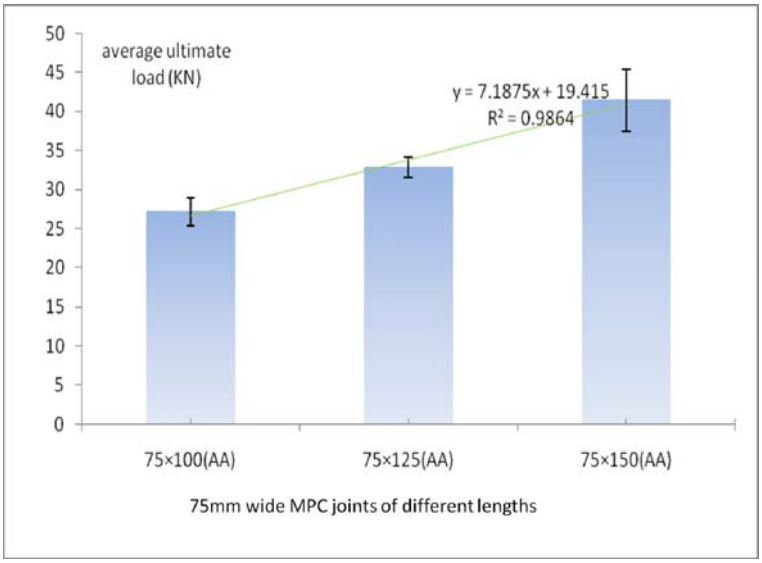

Figure 3. Ultimate tensile loads at different connector lengths for the 75 mm wide specimens loaded in AA mode

Figure 4 summarizes the experimental evidence gathered from the experimental tests carried out on the AA type specimens: (i) for a goven width of the connector, the ultimate tensile load increases with the plate length; (ii) for a given length of the connector, the ultimate tensile load of the joint becomed higher as the width increases.

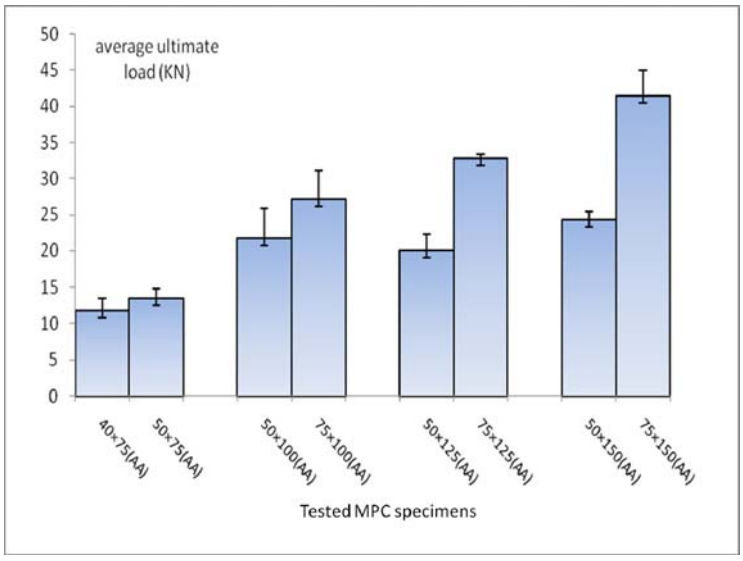

Figure 4. Comparison of the ultimate tensile loads for AA specimens with different plate widths

Figure 5 shows the average ultimate load determined for the 75mm width MPC joints tested under the EA loading mode: 8.34, 12.95 and 20.33 kN, respectively, for the joints including 75×40mm^2, 75×50mm^2 and 75×75mm^2 plates. It can be seen that strength of the joints with longer MPC plates (i.e. 75×50mm^2 and 75×75mm^2) increased by, respectively, 55.3% and 143.8% with respect to the 75×40mm^2 joint.

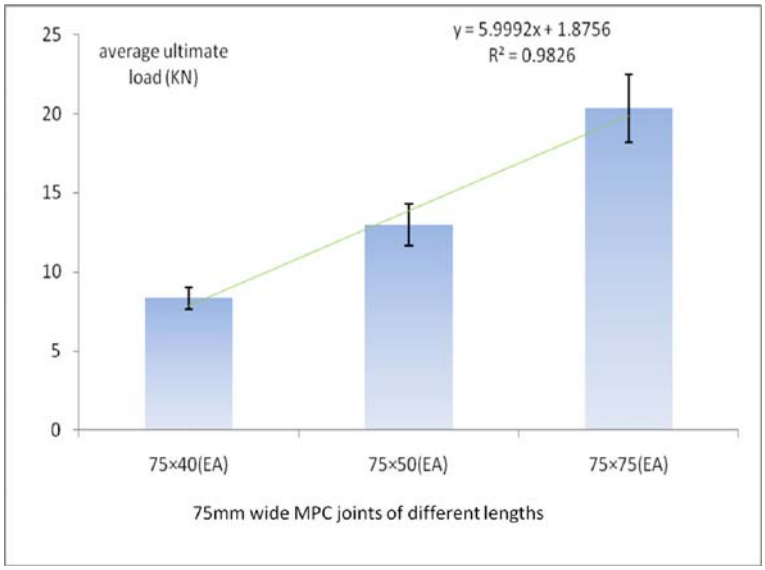

Figure 5. Ultimate tensile loads at different connector lengths for the 75 mm wide specimens loaded in EA mode

The MPC joints in the AA loading mode are stronger than that in the EA loading mode with the same joint dimensions. The ultimate tensile loads as a function of the MPC area are shown in Figure 6. It is seen from Figure 6 that the ultimate load increases linearly as the joint area increases. The R^2 values were determined as 0.73 and 0.83, for AA and EA specimens, respectively, with an average of 0.77.

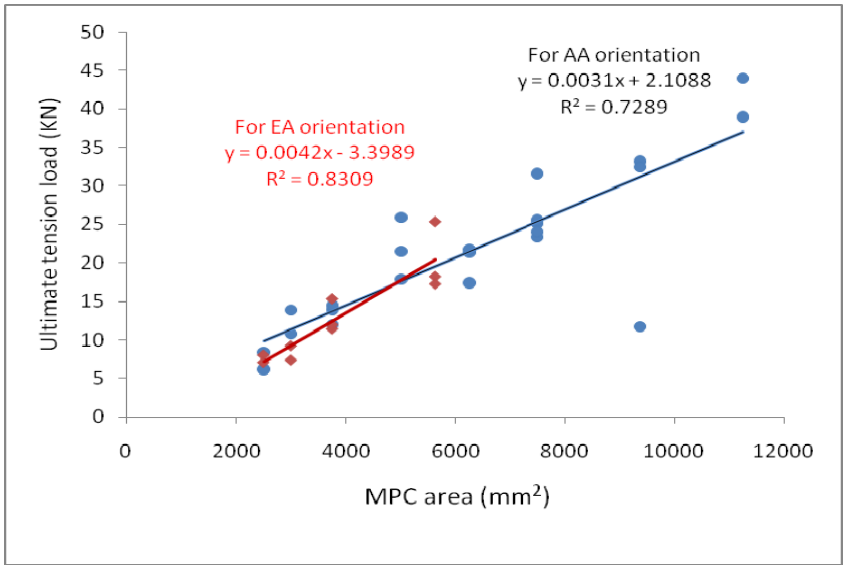

Figure 6. Relationship between the ultimate tensile load and the area of the metal plate connector

3.2 Relationship Between the Failure Modes of MPC Joints and the Joint Sizes

Figure 7 summarizes the failure modes observed in the experimental tests for the MPC joints. Tooth withdrawal, MPC breakage and wood rupture were the predominant failure modes. Tooth withdrawal was the most common failure mode for MPC plates shorter than 100 mm. Tooth withdrawal occurs when the teeth located on the plate edge cannot bear the axial tensile load transferred from the wood. Plate breakage is the most common failure mode for the MPC with a length of at least 100 mm and the plate width of smaller than 75 mm. In this case, the strength of MPC is not enough to bear large axial loads. Therefore, the MPC is more likely to fail when the connector slot is located at interface of the two pieces of wood.

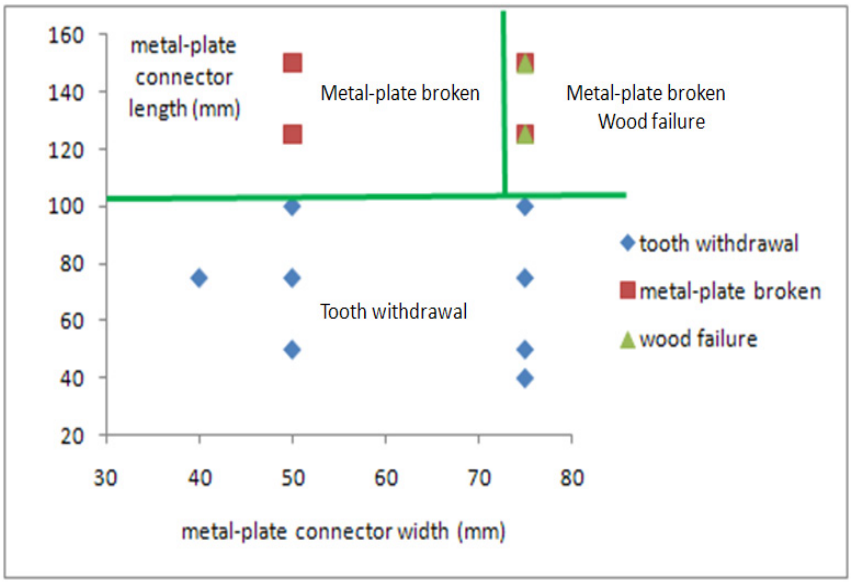

Figure 7. Failure modes observed for the Chinese larch MPC joints tested in this study

4. Conclusions

The relationship between the tensile strength of metal-plate connected Dahurian larch larch lumber joints and the size of the connector were analyzed. Two different loading modes (AA and EA) were considered.

The ultimate tensile loads were found in between 8.41 and 43.97 kN for AA specimens, and 7.4 and 25.4 kN for EA specimens. Increasing the size of the connector (i.e. the length of the plate for a fixed plate width and vice-versa) allows a higher ultimate tensile load to be obtained. The A linear relationship was found between the ultimate tensile load and the joints dimensions.

Tooth withdrawal, MPC breakage and wood rupture were the three failure modes observed for AA type joints, while tool withdrawal was the only failure mode for the EA type joints. Tooth withdrawal, MPC breakage and wood rupture occur in sequence as the axial tension load increases. The AA orientation is more appropriate for evalauting the axial tension properties of MPC joints.

Acknowledgments

This study is part of one Science & Technology Supporting Program during China's 11th Five-year Plan (2006-2010) on wood structural materials that includes other fasteners connection properties in wood construction research at Beijing Forestry Machinery Research Institute of State Forestry Administration and full-size Larch dimension lumber tests at Research Institute of Wood Industry, Chinese Academy of Forestry.

References

Guo, W., Song, S., Zhao, R., Ren, H., Jiang, Z., Wang, G., ... & Fei, B. (2013). Tension Performance of Metal-Plate Connected Joints of Chinese Larch Dimension Lumber. *BioResources, 8*(4), 5666-5677.

Kyoto University. (1982). *Bulletin of the Wood Research Institute, 68*, 22-36.

Chen, G. S., Yu, H. Q., & Zhang, S. F. (2001). Comparison on physical mechanics property of Larch wood in different planting density. *Journal of Northeast Forestry University, 29*(3), 7-12 (in Chinese).

GB50005-2003. (2005). Code for design of timber structures (in Chinese).

GB50329-2002. (2002). Standard for methods testing of timber structures (in Chinese).

GB1931-91. (1992). Method for determination of the moisture content of wood (in Chinese).

GB1933-91. (1992). Method for determination of the density of wood (in Chinese).

Gupta R, Gebremedhin KG (1990) Destructive testing of metal-plate-connected wood truss joints. *Journal of Structural Engineering, 116*(7), 1971-1982.

Gupta R, & Vatovec, M. (1996). Evaluation of dahurian larch in mechanical connections, *Forest Products Journal, 46*(9), 89-93.

Kent, S.M., Gupta, R., Miller, T.H. (1997) Dynamic behavior of metal plate-connected wood truss joints. *Journal of Structural Engineering, 123*(8), 1037-1045.

Lau, P. W. C. (1987). Factors affecting the behavior and modeling of toothed metal-plate joints. Canadian *Journal of Civil Engineering, 14*, 183-195.

O'Regan, P. J., Woeste, F. E., & Lewis, S. L. (1998). Design procedure for the steel net-section of tension splice joints in MPC wood trusses. *Forest Products Journal, 48*(5), 35-42.

Riley, G. J, & Gebremedhin, K. G. (1999). Axial and rotational stiffness model of metal-plate-connected wood truss joints. *Transactions of the ASAE, 42*(3), 761-770.

Sasaki, H., & Hayashi, T. (1982). Static tensile strength of wood butt joints with metal plate connectors. *Wood Research, 68*, 22-36.

Triche, M. H., & Suddarth, S. K. (1988). Advanced desing of metal plate connector joints. *Forest Products Journal, 38*(9), 7-12.

Truss Plate Institute. (1985). *Design specifications for metal-plate connected wood trusses*. Truss plate Institute, Inc., Madison, WI.

Truss Plate Institute. (2002). *ANSI/TPI1-2002 chapter 5-performance evaluation of metal connector plated connections* (pp. 22-38).

Wang, Z. H., Ren, H. Q., Luo, X. Q., & Zhou, H. B. (2009). Mechanical stress of larch dimension lumber from Northeastern China. *China Wood Industry, 23*(3),1-4 (in Chinese).

Journal of Materials Science Research; Vol. 3, No. 3; 2014
ISSN 1927-0585 E-ISSN 1927-0593
Published by Canadian Center of Science and Education

Conductivity Studies and Characterizations of PVA-Orthophosphoric Electrolytes

Lawal Sa'adu[1], M. A. Hashim[1] & Masbudi bin Baharuddin[1]

[1] Faculty of Science and Technology, Universiti Sains Islam Malaysia (USIM), Malaysia

Correspondence: Lawal Sa'adu, Faculty of Science and Technology, Universiti Sains Islam Malaysia (USIM), Bandar Baru Nilai, Negeri Sembilan 71800, Malaysia. E-mail: lawals2004@gmail.com

Received: June 19, 2014 Accepted: July 9, 2014 Online Published: July 24, 2014

doi:10.5539/jmsr.v3n3p48 URL: http://dx.doi.org/10.5539/jmsr.v3n3p48

Abstract

Solid polymer electrolyte (SPEs) has drawn great attention nowadays, particularly in the field of science and applied science, specifically, those used as separators in industries and researchers for the assemblage of some "classified batteries" and super capacitors. In this report, we present the grandeur of this SPE (pure type), particularly at room temperature, such that, it can be applied as an electrolyte as well as a separator in supercapacitor fabrication. The SPEs were produced from the composition of polyvinyl alcohol (PVA) and Phosphoric acid (H_3PO_4), such that, the PVA samples were kept constant while the phosphoric acid was varied at 0, 10, 20, 30, 40, 50, 60, and 70 wt. %. After the experimentation, the pure polymers show excellent results in term conductivity, in that, it has recorded a conductivity as high as 2.56 x 10^{-3} Scm^{-1} at the compositions of 70 wt. %. Aside that, we also observed that, the bulk moduli (R_b) value decreases with the increase in concentration, with pure solid polymer electrolyte (PSPE) recording 2.5 Ω at the highest composition of 70 wt. %.

Keywords: Pure solid polymer electrolyte (PSPE), polyvinyl alcohol (PVA), Phosphoric acid (H_3PO_4), Electrochemical Impedance Spectroscopy (EIS).

1. Introduction

The year 2013 marked the complete three decades (1973) of the invention of polymer electrolyte by Fenton and co-workers (Gu et al., 2000; Kumar & Sundari, 2010; Zhang et al., 2006; Yang, 2004; Ragavendran et al., 2004; Tripath et al., 2012; Ulaganathan et al., 2012; Kuo et al., 2013; Yang et al., 2013; Noor et al., 2010) and Armand (Ragavendran et al., 2004; Zhang et al., 2006). Ever since then, research on polymer electrolyte has become very elaborate.

Research has shown that, there are three classifications of polymer electrolyte systems, namely (i) Polyelectrolytes (PEs): - which have an independent ion-generating groups chemically bond to the macromolecular chain and presence of counter-ion in order to maintain the electroneutrality of the salt. In dry conditions, they have low conductivity of about 10^{-10} – 10^{-15} Scm^{-1} but in the presence of dielectric solvent such as water, there conductivities do improve (Ulaganathan et al., 2012). (ii) Solvent Swollen Polymer Electrolytes (SSPE): - In SSPE, solvents, both aqueous and non-aqueous swells the host polymer. Thus, the dopant ionic solutes such as H_3PO_4 is hosted in the swollen lattice thereby permitting the movement of ions in the solvent swollen region of the polymer host. Their conductivity depends on the compactness of the solvent in the region that is being puffed up (Ulaganathan et al., 2012). And lastly (iii) the Solvent Free Polymer Electrolytes (SFPE): These are polymer salt complex, which is formed by complexes between salts of alkali metals and polymer containing solvating hetroatoms, example; O, S and N (Ulaganathan et al., 2012). The complexation between poly ethylene oxide (PEO) and alkali metal salts is a good example of SFPE. SFPE are sub-classed into three also. They are; (a) Solid Polymer Electrolytes (SPEs), (b) Gel Polymer Electrolytes (GPEs), and (c) Composite polymer electrolytes (CPEs) (Kuo et al., 2013; Tripath et al., 2012).

GPEs can be only considered as plasticizers incorporated polymer-salt complex (Ulaganathan et al., 2012). They are therefore consisted of a liquid electrolytes immobilized in a polymer matrix (Hashmi, (a), 2013) and exhibits high ionic conductivity (10^{-3} to 10^{-4} Scm^{-1} at ambient temperature) and can be obtained by either loading of a liquid electrolyte in a microporous matrix or by increasing the viscosity of a liquid electrolyte through the addition of a soluble polymer until gel consistency is achieved or by mixing a liquid electrolyte with monomers of relatively low molecular weight, then curing the mixture by other means, such as UV polymerization, thermal

polymerization and electron beam radiation polymerization. They are criticized for having weak mechanical strength and poor interracial properties, (Qiu et al., 2004; Hashmi, (b), 2013). In CPEs, they are normally prepared by addition of high surface inorganic filters like SiO_2, MgO, TiO_2 and alike so as to improve the mechanical strength and stiffness of the complex systems (Ulaganathan et al., 2012).

SPE is a thin film that has ionic conductivity, especially, when an alkali, salt dissolves in polymer matrix. SPE have drawn great attention in the development of science and technology of lithium secondary batteries. SPEs have several advantages over liquid, gel and even composite electrolytes in that, it has process ability, flexibility, light weight, elasticity and transparency (Zhang et al., 2006), desirable shape moldability, being free from leakage, mechanical strength, better stability especially in high temperature, and high specific energy and power (Lim et al., 2012). Furthermore, use of use of solid polymer electrolyte can negate the need for a separator and be amendable to low cast manufacturing technologies (Qiu et al., 2004). Some of the applications of SPE are in Batteries, fuel cell, supercapacitors and other electrochemical devices. (Sawada et al., 2000) and other electrochemical devices (Sotta et al., 2010).

Although number of works have been carried out on the characterizations of SSPE like those of Prajapati et al., (2010) and Ahmad Khiar & Arof, (2010), this piece tries to offer a tone by step approach on the conductivity studies of this transparent polymer in order to ascertain the suitability composition for the usage in the supercapacitor fabrication which is the main target of our future work. Thus, careful measures have been put in place to ensure that every detail characteristic of the active materials, especially of the PVA – its molecular weight and its percentage hydrolysis – were taken into considerations.

2. Experimental

2.1. Preparation of the Composite PVA Electrolytes

The pure solid polymer electrolyte (PSPE) which can also be served as separators in supercapacitors fabrications have their laboratory preparations discussed elsewhere by us, in Hashim et al., (2012), Hashim et al., (2014) and by Jiang et al., (2013). But for the purpose of elaboration; the active materials comprise of H_3PO_4 and PVA. The H_3PO_4 functions as an ionic liquid, while PVA acts as a polymeric matrix, allowing ionic transport while simultaneously functioning as a separator between the electrodes of the supercapacitor. H_3PO_4 (>85 wt. % in water, molar mass of 98.00 g/mol, product, number of 1502-80) was obtained in aqueous form, from R & M marketing, Essex, UK brand, while the PVA (molecular weight; 89,000-98,000, 99+ % hydrolyzed) was obtained from Sigma Aldrich. Both H_3PO_4 and PVA were used as-received without further treatment or purification. An aqueous solution of PVA is prepared by combining PVA with distilled water in the ratio of 1:10 by volume. This solution is mechanically agitated by magnetic stirring at 60 °C for five hours to thoroughly dissolve the PVA in the distilled water. H_3PO_4 was then mixed with the PVA aqueous solution in the ratio of 100:0, 90:10, 80:20, 70:30, 60:40, 50:50, 40:60 and 30:70 wt. % for the PSPE to be obtained (this has been summarized in Table 1).

In order to vary the percentage of the H_3PO_4 used, the following formula was used;

$$\frac{n}{n+2} \times 100\% = x\% \tag{1}$$

Where x is the percentage of acid require (0, 10, 20, 30, 40, 50, 60, and 70 % wt), and n is the value of H_3PO_4 in grams.

The mixing is done in a drop-wise manner with magnetic stirring at 60 °C for about one hour or thereabouts until it completely turns to homogeneous solution (transparent in this case). The mixture is then allowed to cool down to an ambient temperature. The resulting homogeneous solution of PVA/H_3PO_4 is cast over a plastic Petri dish. Prior to this, the Petri dish was scraped off the dust using a tissue soaked in acetone. The PVA/H_3PO_4 solution solidifies onto the Petri dish and upon curing for about 3 – 4 weeks at room temperature. This is due to its high molecular weight and consequently more hydrolyzed. The solid layer was easily peeled off from the Petri dish after it dries as a freestanding layer. The thickness of the solid layers formed in this procedure can be controlled depending on the composition that have been enumerated above and as shown in Figure 1. The resulting polymer film was then put in the plastic bags for safe keeping, and to avoid contamination from surrounding, for further property analysis.

3. Result and Discussion

3.1. Conductivity and Chemical Composition Analysis

Conductivity measurements were carried out on both the solid and hybrid polymer electrolyte films which are also composed of all the different percentage ratio of PVA-H_3PO_4 an impedance method which also was highlighted by Ahmad Khiar and Arof (2010). The solid polymer films were sandwiched between a stainless steel, ion-blocking

liked measuring device (otherwise known as a probe), each of surface area 2 cm^2 in radius, in a spring-loaded glass holder.

The impedance measurements were carried out by using Electrochemical Impedance Spectroscopy (EIS) testing machine named HIOKI 3532-50 LCR Hi-Tester which was connected to the computer. The frequency range of the device was 50 Hz - 1 MHz, and simultaneously calculating both real and imaginary impedance.

Figure 1. Showing a prepared and flexible PSPE

Table 1. Table Showing the Overall Formation of the PSPE Preparation

Coding	Measured Quantity PVA in Distilled Water (g)	Measured Quantity of H_3PO_4 (g)	Ratio of PVA to H_3PO_4
P0	2	0	100:0
P10	2	0.22	90:10
P20	2	0.50	80:20
P30	2	0.86	70:30
P40	2	1.33	60:40
P50	2	2.00	50:50
P60	2	3.00	40:60
P70	2	4.67	30:70

The sample exhibits Debye characteristics, and then the plots of the negative imaginary impedance versus the real impedance on the graph should be able to display a semicircle-like shape (Ahmad Khiar & Arof 2010). From the Eq. 2, we calculated the electrical conductivity of the samples;

$$\sigma = \frac{l}{R_b A} \tag{2}$$

Where σ is the conductivity itself, l and A are respectively the thickness and area of the samples. The thickness of the sample was measured twice at different positions of the polymer films and an average was taken using digital micrometer.

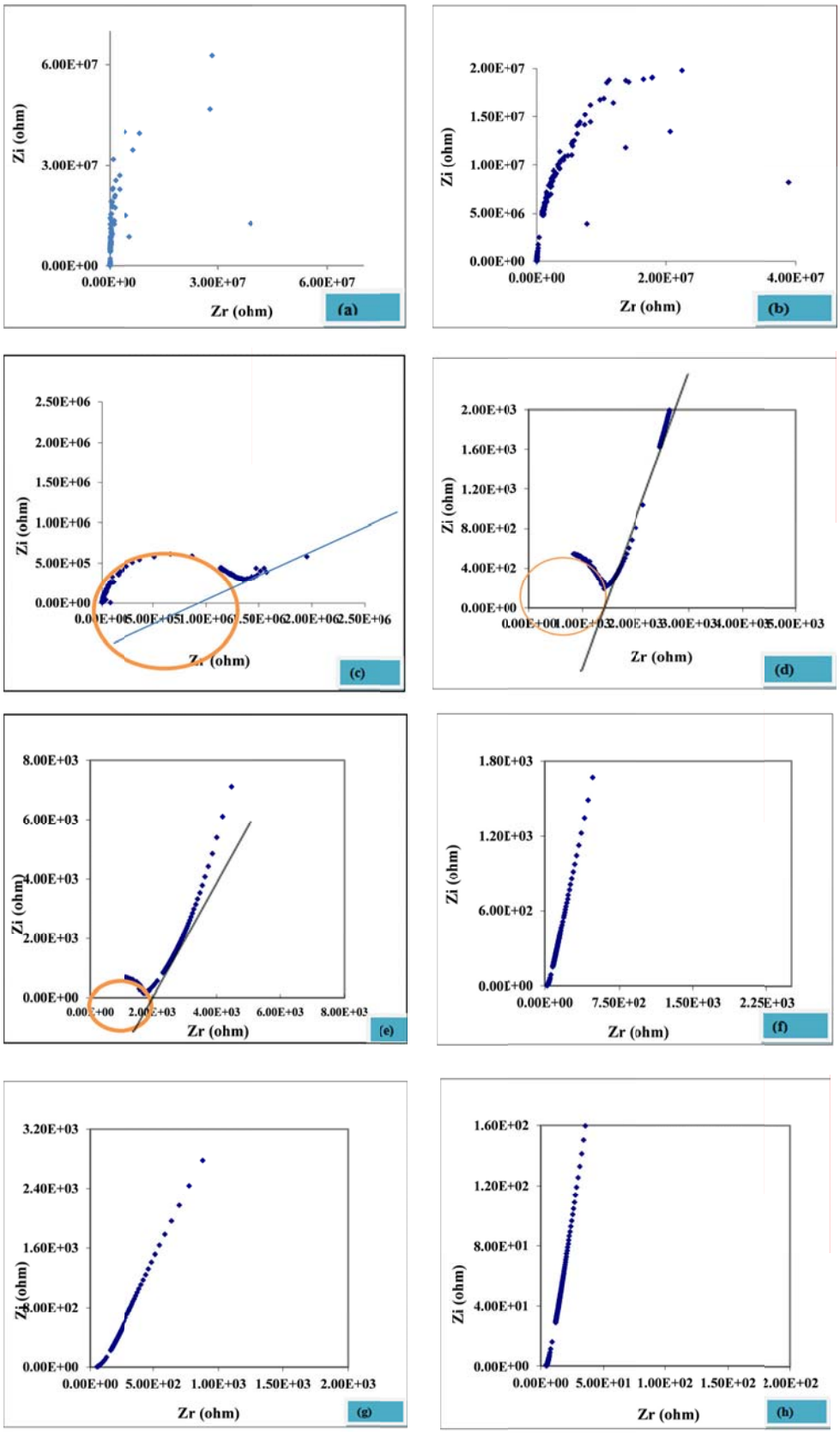

Figure 2. Impedance plots of PSPE containing 0 wt.% (a); 10 wt.% (b); 20 wt.% (c); 30 wt.% (d); 40 wt.% (e); 50 wt.% (f); 60 wt.% (g); 70 wt.% (h) ratio of the H_3PO_4 at room temperatures

Figure 2 (a-h) shows the impedance plots of a sample of the PSPE containing 0, 10, 20, 30, 40, 50, 60, and 70 wt. % ratio of the H_3PO_4 at room temperatures respectively. For the sample with 0 and 10 wt.% of the H_3PO_4, it can be observed that the point of the graph was dispersed, which clearly indicates the meager or absent of acid in this sample.

The semicircles found on the Figure of the samples containing 20, 30 and 40 wt.% could however be connected with the impact of the introduction of the percentage acid and consequently the immobile polymer chain begins to emerge.

As the acid concentration continues to increase, so the conductivity, thereby making the semicircle disappear, which is an indication that, ions that move around the polymer matrix made resistive component of the polymer electrolytes to exist. (Ahmad Khiar & Arof, 2010; Ulaganathan et al., 2012).

The calculated R_b for all the eight samples above were obtained from the frequency intercepts on each and every plotted graph. We also observed that, the R_b value decreases with the increase in concentration. The calculated values of the R_b are 1.15×10^8, 8.00×10^4, 2.40×10^4, 1.70×10^3, 2.10×10^3, 1.93×10^1, 1.26×10^1 and 2.58 Ω for 0, 10, 20, 30, 40, 50, 60, and 70 wt.% ratio of the H_3PO_4 respectively. The highest conductivity of PSPE sample was observed at 2.56×10^{-3} Scm^{-1} when the H_3PO_4 was increased to 70 wt.% while the lowest conductivity of the sample was noticed at 2.25×10^{-11} Scm^{-1} where the H_3PO_4 percentage was nil. Full details about the average values of the conductivity of PSPE is summarized in Table 2. On a general note, it can be said that, the sample of PSPE performed wonderfully well in terms of both bulk resistance calculation and the conductivity as a whole.

As mentioned earlier, that conductivity is dependent on the concentration of the H_3PO_4. Table 2 provided us with the information that, there is a relationship between the acid concentration and the polymer matrix. In addition to that, it also be deduce from the table that, the thickness on each sample, also had some impact on the conductivity of the samples. Hence, because of the thinner nature of the films in PSPE, the conductivity seems to be very promising.

Table 2. Parameters that Determine the Conductivity in PSPE

Coding	PVA: H_3PO_4	l (mm±0.005)	R_b (Ω)	σ (Scm^{-1})
P0	100:0	0.00910	1.15×10^8	2.25×10^{-11}
P10	90:10	0.00630	8.00×10^4	7.20×10^{-8}
P20	80:20	0.01100	2.40×10^4	1.46×10^{-7}
P30	70:30	0.05400	1.70×10^3	1.01×10^{-5}
P40	60:40	0.00585	2.10×10^3	8.87×10^{-7}
P50	50:50	0.00745	1.93×10^1	1.23×10^{-4}
P60	40:60	0.02615	1.26×10^1	6.61×10^{-4}
P70	30:70	0.02070	2.58×10^0	2.56×10^{-3}

3.2 Crystal Structure Analysis

The crystal structure analysis of the solid polymer electrolyte films was examined by a Philip X'Pert X-ray diffractometer (XRD) with Cu K_α radiation of wavelength λ=1. 54056 Å for 2θ angles between 10° and 80°.The XRD analysis was carried out on the PSPE films. After the analysis, the following results were obtained. The analysis of the structure of the PSPE for 0 wt.% (a); 10 wt.% (b); 20 wt.% (c); 30 wt.% (d); 40 wt.% (e); 50 wt.% (f); 60 wt.% (g); 70 wt.% (h) ratio of the H_3PO_4 was shown in Figure 3.

It can be observed from the semi-crystalline peak of the PVA ($\theta=20^o$) which also affirmed the argument put across by (Hashmi, (c), 2013) about the semi-crystal behavior of the PVA. The addition of H_3PO_4 causes the decrease in the degree of the crystallinity and consequently the increase in the amorphicity of the material and its conductivity.

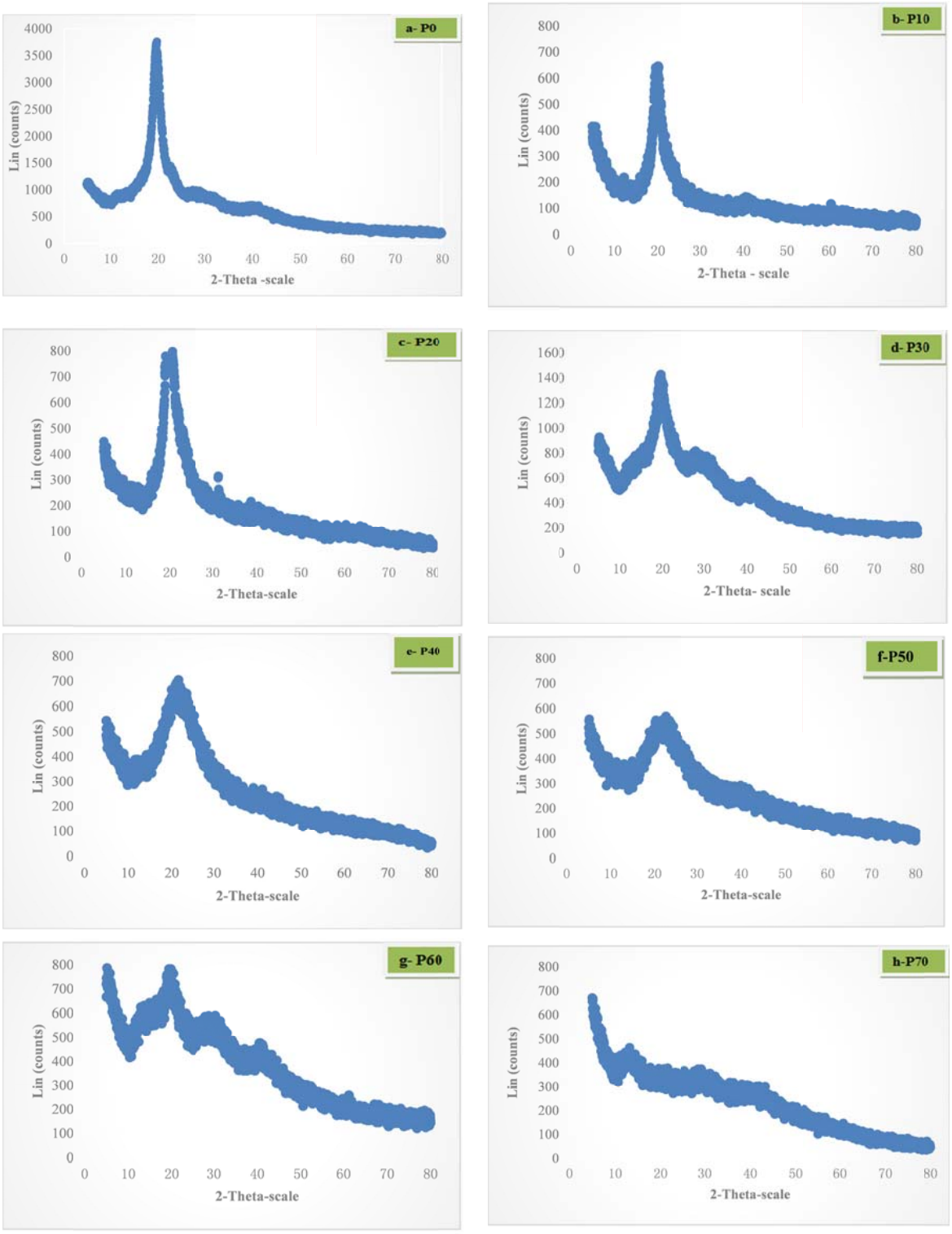

Figure 3. XRD Analysis of PSPE containing 0 wt.% (a); 10 wt.% (b); 20 wt.% (c); 30 wt.% (d); 40 wt.% (e); 50 wt.% (f); 60 wt.% (g); 70 wt.% (h) ratio of the H_3PO_4 and (i) A combined graph containing all the percentages.

3.4 Differential Scanning Calorimetry Analysis

The DSC thermal analysis was carried out using the DCS machine (Mettler Toledo DSC A851 with Star software) under N_2 atmosphere with 10 °C/min heating rate from 40 to 300 °C in order to observe the crystalline and semi-crystalline behavior of the whole samples, therefore, various parameters related to thermal properties such as

glass transition temperature ***(T_g)***, thermal transition ***(T_m)*** of crystalline phase of the polymer electrolytes and degree of crystallinity ***(T_c)*** can be evaluated from the DSC data. Samples for DSC measurements were prepared from several tiny rectangular pieces cut from the polymer film to a mass ranging from 1.98 -24.24 mg for PSPE and 7.08 – 19.82 mg for HSPE. The temperature range studied was −40 to 200 °C. The heating/cooling rate was 10 °C/min.

Table 3. Parameters for the Thermometric Analysis in PSPE

Coding	PVA: $_3PO_4$	Mass (g)	Temperature (°C)		
			T_g	T_m	T_c
P0	100:0	1.98	98.11	223.56	152.00
P10	90:10	4.48	80.78	221.06	166.27
P20	80:20	7.41	127.31	207.26	186.45
P30	70:30	8.27	117.63	156.46	-
P40	60:40	15.12	116.89	155.00	-
P50	50:50	13.53	101.13	164.59	160.05
P60	40:60	19.48	63.28	160.00	150.00
P70	30:70	24.40	79.41	129.09	79.41

Figure 4 shows the DSC analysis result of PSPE containing 0 wt.% (a); 10 wt.% (b); 20 wt.% (c); 30 wt.% (d); 40 wt.% (e); 50 wt.% (f); 60 wt.% (g); 70 wt.%. From the Figure and Table 3 it can be seen that, the first three samples show a very good T_m with an endothermic peak of slightly above 200 ^{0}C (i.e. 233.56, 221 and 207.26 for P0, P10 and P20 respectively) which indicates the huge percentage weight of PVA is present here. Noting the theoretical value of the thermal transition of the pure PVA as 230 ^{0}C, this result is closely related to that, and was in agreement with that of (Jelinska et al., 2010; Agrawal, 2004; Othman et al., 2011). However, probably due to the presence of chemical content, or intermolecular interaction (Mudigoudra et al., 2012) form among PVA and H_3PO_4, the thermal transition starts to decrease with the increase in temperature.

The higher the melting point temperature the more the stability of the molecules therein, as such, pure PVA has more stable molecules than PVA/H_3PO_4 composite. So, it can be seen that the T_m and T_c decreases (or even diminishes) as the concentration of the acid increase. This is a known fact that, in homogenized blends, the melting shifts to the lower level (Othman et al., 2011; Guirguis & Moselhey, 2012.). The other unusual humps cited in especially P0 and P60 could be as a result of the presence of the moisture inside the samples. Also the theoretical glass transition of the PVA alone is about 85 ^{o}C while the composite shows down and upwards shifts of this temperature. This could not be unconnected with the gradual increment in the concentration of the acid.

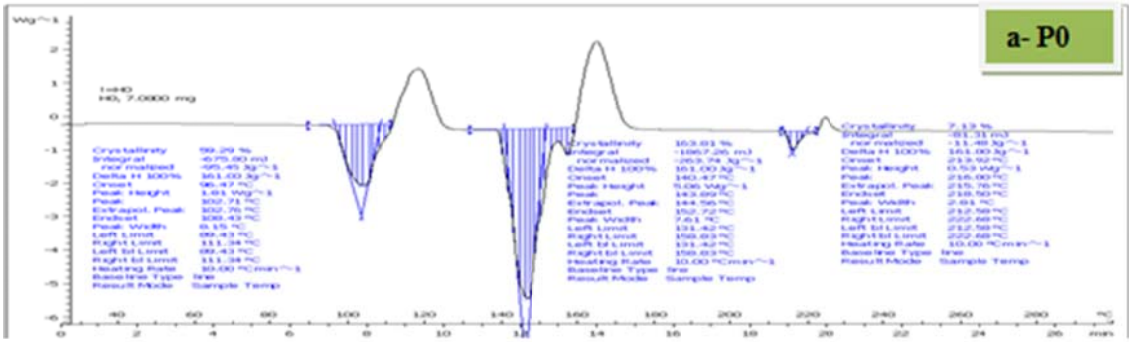

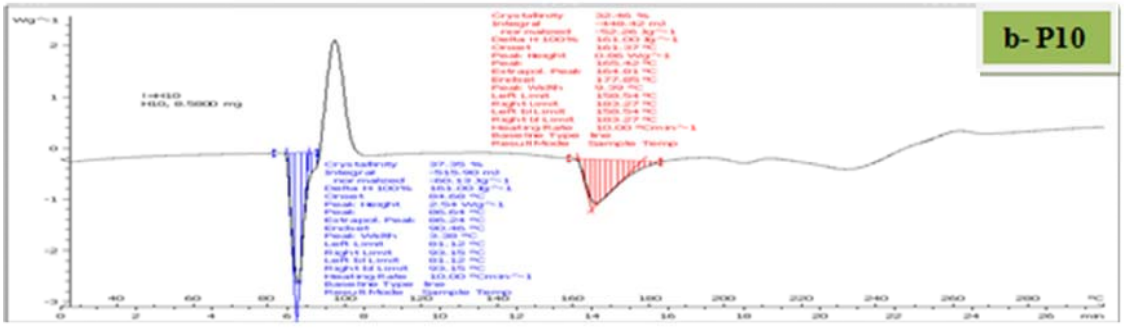
b- P10

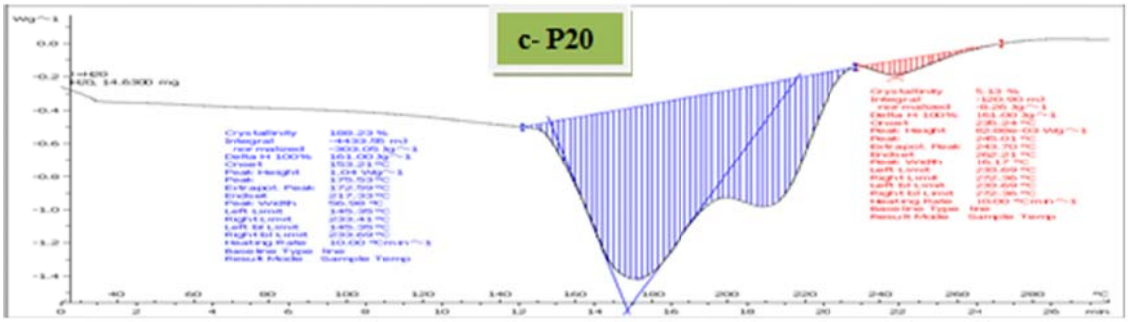
c- P20

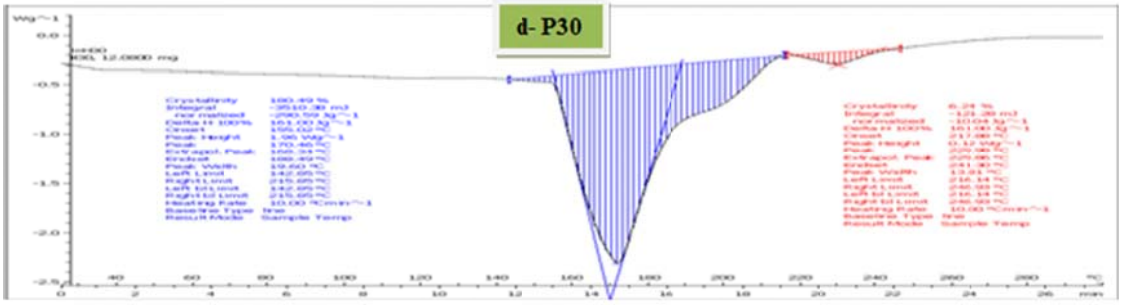
d- P30

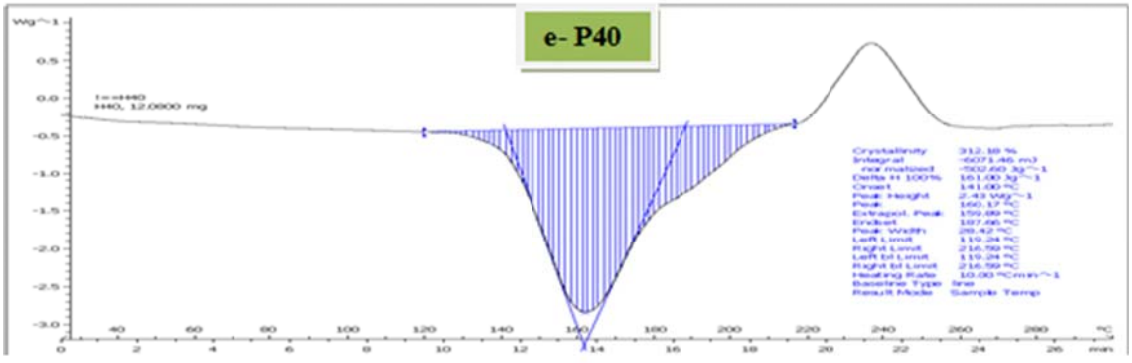
e- P40

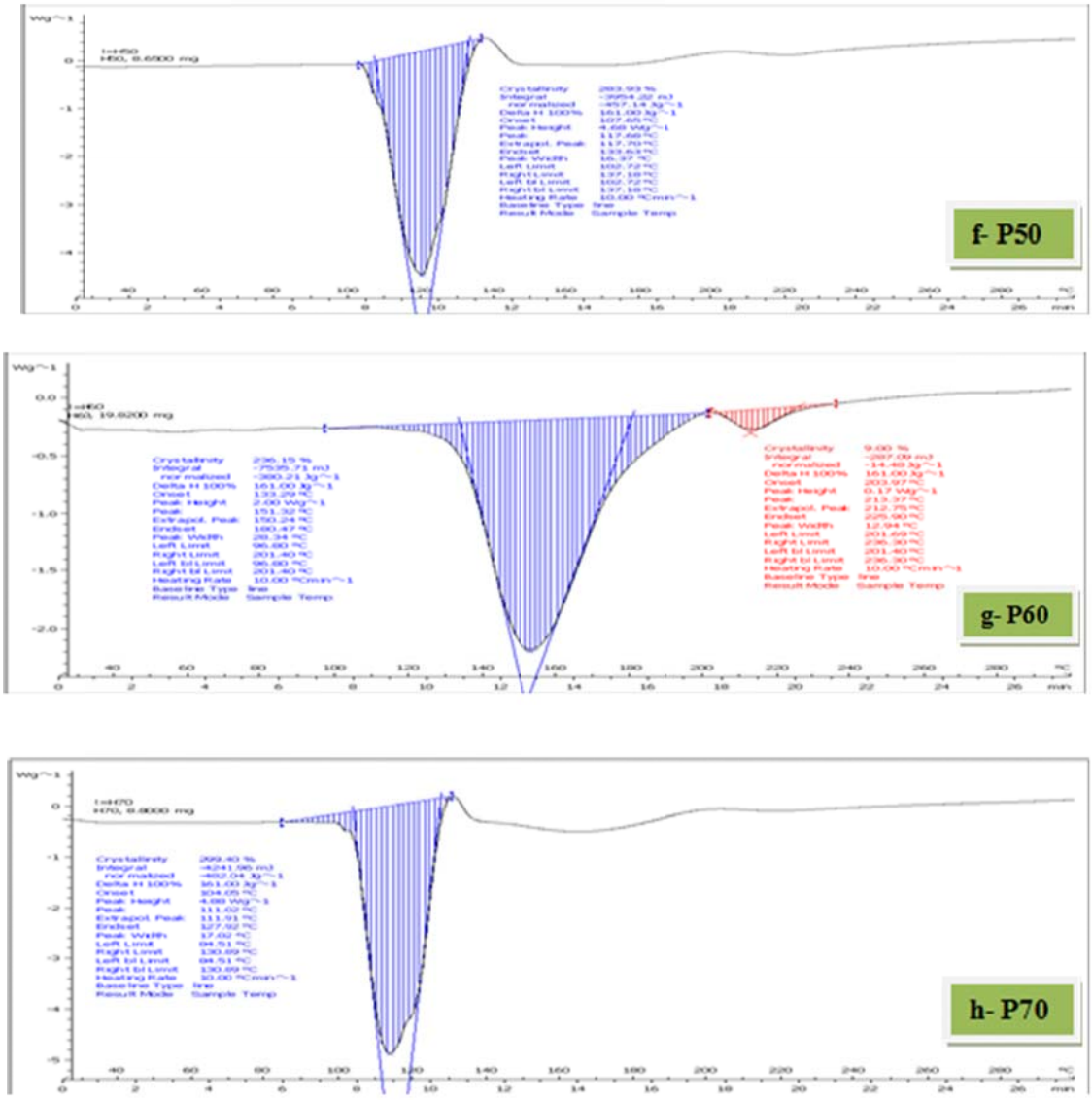

Figure 4. DSC Analysis of Solid (S) Solid Polymer electrolyte containing 0 wt.% (a); 10 wt.% (b); 20 wt.% (c); 30 wt.% (d); 40 wt.% (e); 50 wt.% (f); 60 wt.% (g); 70 wt.% (h)

4. Conclusion

In this study, we have introduced the noble of the pure solid polymer electrolyte at room temperature used as an electrolyte as well as a separator from the piece of PVA and H_3PO_4 such that, the PVA samples were kept constant while the phosphoric acid was varied at 0, 10, 20, 30, 40, 50, 60, and 70 wt. %. The PSPE results in higher conductivity of 2.56 x 10^{-3} Scm^{-1}, at the compositions of 70 wt. %, in addition to that, we also observed that, the bulk modulus R_b decreases with the increase in concentration, recording 2.5 Ω at the highest composition of 70 wt. %. The XRD analysis reveals the semi-crystalline peak of the PVA at $\theta=20^o$ border humps of the left indicating the inclusion of the acid and the crystallinity decreases as the acid concentration increases. This result was confirmed by the DSC analysis.

Acknowledgements

The corresponding author wishes to acknowledge the assistance and contributions of management of the Faculty of Science and Technology USIM under which ERGS grant (USIM/ERGS-FST-52-50111) has been provided for the purpose of this research.

Reference

Agrawal, S. L., & Awadhia, A. (2004). DSC and conductivity studies on PVA based proton conducting gel electrolytes. *Bulletin of Materials Science, 27*(6), 523-527. http://dx.doi.org/ 10.1007/BF02707280

Ahmad Khiar, A. S., & Arof, A. K. (2010). Conductivity Studies of Starched-based polymer electrolytes. *Ionics, 16*, 123-129. http://dx.doi.org/ 10.1007/s11581-009-0356-y

Gu, H.-B., Kim, J.-U., Song, H.-W., Park, G.-C. & Park, B.-K. (2000). Electrochemical Properties of Carbon Composite Electrode with Polymer Electrolyte for Electric Double-Layer Capacitor. *Electrochimica Acta, 45*, 1533-1536. http://dx.doi.org/ 10.1016/S0013-4686(99)00370-9

Guirguis, O. W., & Moselhey, M. T. H. (2012). Thermal and structural studies of poly(vinyl alcohol) and hydroxypropyl cellulose blends. *Natural Science, 4*, 57-67. http://dx.doi.org/ 10.4236/ns.2012.41009

Hashim, M. A, Sa'adu, L., & A. K. Dasuki. (2012). Supercapacitor Based On Activated Carbon And Polymer Electrolyte. *International Journal Of Sustainable Energy And Environmental Research, 1*, 1-6.

Hashim, M. A, Sa'adu, L., Baharuddin, M., & Dasuki, A. K. (2014). Using PVA, Methacrylate and Lauroyl Chitosan as Separator in Supercapacitors. *Journal of Materials Science Research, 3*(1). http://dx.doi.org/ 10.5539/jmsr.v3n1p25

Hashmi, S. A. (2013). Characteristics of Conducting Polymers for their Supercapacitive Performance. *Paper presented at the Workshop on Advanced Energy Storage Materials & Devices (WAESD)*. Universiti Pertahanan Nasional Malaysia (National Defense University Malaysia).

Hashmi, S. A. (2013). Electrical Double Layer Capacitor: Recent Development. *Paper presented at the Workshop on Advanced Energy Storage Materials & Devices (WAESD).* Universiti Pertahanan Nasional Malaysia (National Defense University Malaysia).

Hashmi, S. A. (2013). Polymer-Based Gel electrolytes for New Generation Supercapacitors. *Paper presented at the Workshop on Advanced Energy Storage Materials & Devices (WAESD)*. Universiti Pertahanan Nasional Malaysia (National Defense University Malaysia).

Jelinska, N., Kalnins, M., Tupureina, V. & Dzene, A. (2010). Poly (Vinyl Alcohol)/Poly (Vinyl Acetate) Blend Films. *Scientific Journal of Riga Technical University, 21*, 55-61.

Jiang, L., Vangari, M., Pryor, T., Xiao, Z. & Korivi, N. S. (2013). Miniature Supercapacitors Based on Nanocomposite Thin Films. *Microelectronic Engineering, 111*, 52-57. http://dx.doi.org/10.1016/j.mee.2013.01.030

Kumar, K. V., & Suneeta Sundar, G. (2010). Conductivity Studies Of (PEO +KHCO3) Solid Electrolyte System and its Application as an Electrochemical Cell. Journal *of Engineering Science and Technology, 5*, 130-139.

Kuo, C.-W., Huang, C.-W., Chen, B.-K., Li, W.-B., Chen, P.-R., Ho, T.-H., Tseng C.-G. & Tzi-Yi, W. (2013). Enhanced Ionic Conductivity in PAN-PEGME-LiClO4-PC Composite Polymer Electrolytes. *Int. J. Electrochem. Sci., 8*, 3834-3850.

Lim, D.-H., Manuel, J., Ahn, J.-H.,. Kim, J.-K., Jacobsson, P., Matic, A., Ha, J.K., Cho, K.K. & Kim, K. W. (2012). Polymer Electrolytes Based on Poly(Vinylidene Fluoride-Co-Hexafluoropropylene) Nanofibrous Membranes Containing Polymer Plasticizers for Lithium Batteries. *Solid State Ionics, 225*, 631-635. http://dx.doi.org/10.1016/j.ssi.2012.03.028

Mudigoudra, B. S., Masti, S. P., & Chougale, R. B. (2012). Thermal Behavior Of Poly (Vinyl Alcohol)/ Poly (Vinyl Pyrrolidone)/Chitosan Ternary Polymer Blend Films. *Research Journal Of Recent Sciences, 1*, 83-86.

Ahmad, A., Rahman, M. Y. B. A., & Talib, I. A. (2010). Solid polymeric electrolyte of poly (ethylene) oxide-50% epoxidized natural rubber-lithium triflate (PEO-ENR50-LiCF3SO3). *Natural Science, 2*(03), 190-196. http://dx.doi.org/10.4236/ns.2010.23029

Othman, N., Azahari, N. A. & Ismail, H. (2011). Thermal Properties Of Polyvinyl Alcohol (PVOH)/Corn Starch Blend Film. *Malaysian Polymer Journal, 6*(6), 147-154.

Prajapati, G. K., Roshan, R., & Gupta, P. N. (2010). Effect of plasticizer on ionic transport and dielectric properties of PVA-H3PO4 proton conducting polymeric electrolytes. *Journal of Physics and Chemistry of Solids, 71*, 1717-1723. http://dx.doi.org/10.1016/j.jpcs.2010.08.023

Qiu, W.-L., Ma, X.-H., Yang, Q.-H., Fu, Y.-B & Zong, X.-F (2004). "Novel Preparation of Nanocomposite Polymer Electrolyte and its Application to Lithium Polymer Batteries". *Journal of Power Sources, 138*, 245-252. http://dx.doi.org/10.1016/j.jpowsour.2004.06.061

Ragavendran, K., Kalyani, P., Veluchamy, A., Banumathi, S., Thirunakaran, R., & Benedict, T. J. (2004). Characterization of Plasticized PEO Based Solid Polymer Electrolyte by XRD and AC Impedance Methods. *Portugaliae Electrochimica Acta, 22*, 149-159.

Sawada, H., Ariyoshi, Y., Lee, K., Kyokane, J., & Kawase, T. (2000). New Approach To Highly Conductive Polymer Electrolytes: Synthesis of Gelling Fluoroalkylated End-Capped 2-Acrylamido-2-Methylpropanesulfonic Acid Copolymers Containing Poly (Oxyethylene) Units. *European Polymer Journal, 36*, 2523-2526. http://dx.doi.org/10.1016/S0014-3057(00)00024-0

Sotta, D., Bernard, J. & V.-S. Moynot. (2010). Application of Electrochemical Impedance Spectroscopy to The Study of Ionic Transport in Polymer-Based Electrolytes. *Progress in Organic Coatings, 69*, 207-214. http://dx.doi.org/10.1016/j.porgcoat.2010.04.011

Toney, M. F. (1992). X-Ray diffraction. In L. E. Fitzpatrick, C. R. Brundle, C. A. Evans Jr, & S. Wilson (Comp. & Ed.), *Encyclopedia of Material characterization* (pp. 198-213).

Tripathi, S. K., Gupta, A., & Manju, K. (2012). Studies on Electrical Conductivity and Dielectric Behaviour of PVdF-HFP-PMMA-NaI Polymer Blend Electrolyte. *Bull. Mater. Sci., 35*, 969-975. http://dx.doi.org/10.1007/s12034-012-0387-2

Ulaganathan, M., Nithya, R., & Rajendran, S. (2012). Surface Analysis Studies on Polymer Electrolyte Membranes Using Scanning Electron Microscope and Atomic Force Microscope. *Intech, 33*, 671-694.

Yang, C. C. (2004). Chemical Composition and XRD Analyses for Alkaline Composite PVA Polymer Electrolyte. *Materials Letters, 58*, 33-38. http://dx.doi.org/ 10.1016/S0167-577X(03)00409-9

Yang, R., Zhang, S., Zhang, L., & Wenbo, L. (2013). Electrical Properties of Composite Polymer Electrolytes Based on PEO-SN-$LiCF_3SO_3$. *Int. J. Electrochem. Sci., 8*, 10163-10169.

Zhang, Y.-J., Huang, Y.-D. & Lei, W. (2006). Study of EVOH Based Single Ion Polymer Electrolyte: Composition and Microstructure Effects on the Proton Conductivity. *Solid State Ionics, 177*, 65-71. http://dx.doi.org/ 10.1016/j.ssi.2005.10.008

Journal of Materials Science Research; Vol. 3, No. 3; 2014
ISSN 1927-0585 E-ISSN 1927-0593
Published by Canadian Center of Science and Education

Reviewer Acknowledgements

Journal of Materials Science Research wishes to acknowledge the following individuals for their assistance with peer review of manuscripts for this issue. Their help and contributions in maintaining the quality of the journal is greatly appreciated.

Journal of Materials Science Research is recruiting reviewers for the journal. If you are interested in becoming a reviewer, we welcome you to join us. Please find the application form and details at http://www.ccsenet.org/reviewer and e-mail the completed application form to jmsr@ccsenet.org.

Reviewers for Volume 3, Number 3

Yan Huo, Michigan Technological University, United States

Qiu Yu, Shanghai Institute of Microsystem and Information Technology, Chinese Academy of Sciences, China

Ioannis Rabias, Research Associate/ visiting scientist NCSR DEMOKRITOS, Greece

Rui Liu, Kent State University, United States

Ashwith Chilvery, Talladega College, United States

Enrico Franceschi, University of Genoa, Italy

Mosaad Sadawy, Faculty of Engineering, Al-Azhar University, Egypt

Luciano Lamberti, Dipartimento di Meccanica, Matematica e Management, Politecnico di Bari, 70126, Bari, Italy

R. E. Rowlands, University of Wisconsin, Madison, WI 53701, USA

Ashwith Chilvery, Talladega College, United States

Gholam Ali Koohmareh, University of Isfahan, Iran

Shudipto Konika Dishari, The Pennsylvania State University, United States

Call for Manuscripts

Journal of Materials Science Research is a peer-reviewed journal, published by Canadian Center of Science and Education. It publishes reviews, and research papers on studying the relationship between structure, properties, and uses of materials. It focuses on the following topic areas: composite materials, carbon, ceramics and glasses, metals, polymers, semiconductors, thin films, nanomaterials, refractory, semiconductors, biomaterials and functionally graded materials. All submitted articles should report original, previously unpublished research results, experimental or theoretical.

The journal is published in both printed and online versions, and the online version is free access and download.

We are seeking submissions for forthcoming issues. All manuscripts should be written in English. Manuscripts from 3000–8000 words in length are preferred. All manuscripts should be prepared in MS-Word format, and submitted online, or sent to: jmsr@ccsenet.org

Paper Selection and Publishing Process

a) Upon receipt of a submission, the editor sends an e-mail of confirmation to the submission's author within one to three working days. If you fail to receive this confirmation, your submission e-mail may have been missed.

b) Peer review. We use a double-blind system for peer review; both reviewers' and authors' identities remain anonymous. The paper will be reviewed by at least two experts: one editorial staff member and at least one external reviewer. The review process may take two to three weeks.

c) Notification of the result of review by e-mail.

d) If the submission is accepted, the authors revise paper and pay the publication fee.

e) After publication, the corresponding author will receive two hard copies of the journal, free of charge. If you want to keep more copies, please contact the editor before making an order.

f) A PDF version of the journal is available for download on the journal's website, free of charge.

Requirements and Copyrights

Submission of an article implies that the work described has not been published previously (except in the form of an abstract or as part of a published lecture or academic thesis), that it is not under consideration for publication elsewhere, that its publication is approved by all authors and tacitly or explicitly by the authorities responsible where the work was carried out, and that, if accepted, the article will not be published elsewhere in the same form, in English or in any other language, without the written consent of the publisher. The editors reserve the right to edit or otherwise alter all contributions, but authors will receive proofs for approval before publication.

Copyrights for articles are retained by the authors, with first publication rights granted to the journal. The journal/publisher is not responsible for subsequent uses of the work. It is the author's responsibility to bring an infringement action if so desired by the author.

More Information

E-mail: jmsr@ccsenet.org

Website: www.ccsenet.org/jmsr

Paper Submission Guide: www.ccsenet.org/submission

Recruitment for Reviewers: www.ccsenet.org/reviewer

The journal is peer-reviewed
The journal is open-access to the full text
The journal is included in:

CAS
DOAJ
EBSCOhost
Google Scholar
JournalTOCs
PKP Open Archives Harvester
ProQuest
Standard Periodical Directory
Ulrich's
Universe Digital Library
WorldCat

Journal of Materials Science Research
Quarterly

Publisher Canadian Center of Science and Education
Address 1120 Finch Avenue West, Suite 701-309, Toronto, ON., M3J 3H7, Canada
Telephone 1-416-642-2606
Fax 1-416-642-2608
E-mail jmsr@ccsenet.org
Website www.ccsenet.org/jmsr

ISSN 1927-0585